INFORMATION TO USERS

This manuscript has been reproduced from the microfilm master. UMI films the text directly from the original or copy submitted. Thus, some thesis and dissertation copies are in typewriter face, while others may be from any type of computer printer.

The quality of this reproduction is dependent upon the quality of the copy submitted. Broken or indistinct print, colored or poor quality illustrations and photographs, print bleedthrough, substandard margins, and improper alignment can adversely affect reproduction.

In the unlikely event that the author did not send UMI a complete manuscript and there are missing pages, these will be noted. Also, if unauthorized copyright material had to be removed, a note will indicate the deletion.

Oversize materials (e.g., maps, drawings, charts) are reproduced by sectioning the original, beginning at the upper left-hand corner and continuing from left to right in equal sections with small overlaps.

Photographs included in the original manuscript have been reproduced xerographically in this copy. Higher quality 6" x 9" black and white photographic prints are available for any photographs or illustrations appearing in this copy for an additional charge. Contact UMI directly to order.

ProQuest Information and Learning
300 North Zeeb Road, Ann Arbor, MI 48106-1346 USA
800-521-0600

Université d'Ottawa · University of Ottawa

Université d'Ottawa • University of Ottawa

FACULTÉ DES ÉTUDES SUPÉRIEURES ET POSTDOCTORALES

FACULTY OF GRADUATE AND POSTDOCTORAL STUDIES

ASMANRAFAT, Mehrdad

AUTEUR DE LA THÈSE - AUTHOR OF THESIS

M.A.Sc. (Chemical Engineering)

GRADE - DEGREE

Department of Chemical Engineering

FACULTÉ, ÉCOLE, DÉPARTEMENT - FACULTY, SCHOOL, DEPARTMENT

TITRE DE LA THÈSE - TITLE OF THE THESIS

Surface Characterization of Hollow Fiber Dialysis Membranes Used in Artificial Kidney

Takeshi Matsuura

DIRECTEUR DE LA THÈSE - THESIS SUPERVISOR

EXAMINATEURS DE LA THÈSE - THESIS EXAMINERS

Graham Neale

William Kozicki

J.-M. De Koninck, Ph.D.

LE DOYEN DE LA FACULTÉ DES ÉTUDES SUPÉRIEURES ET POSTDOCTORALES

SIGNATURE

DEAN OF THE FACULTY OF GRADUATE AND POSTDOCTORAL STUDIES

Surface Characterization of Hollow Fiber Dialysis Membranes Used in Artificial Kidney

Mehrdad Asmanrafat

A thesis submitted to the Faculty of Graduate and Postdoctoral Studies
in partial fulfillment of the requirements for the
degree of
Master of Applied Science
in the Department of Chemical Engineering
University of Ottawa
Ottawa, Canada

January, 2002

ABSTRACT

The internal and external surfaces of dialysis hollow fiber membranes were characterized by the combination of two techniques, e.g. contact angle measurement (CAM) and atomic force microscopy (AFM), aiming at the improvement of membrane biocompatibility. A number of surface properties including surface energy, roughness, pore size, and nodule size were evaluated.

CAM studies were carried out by observing the liquid meniscus at the surfaces of hollow fibers. An imaging system equipped with a goniometer protractor and a video camera was developed for this purpose. AFM studies were also conducted at the internal surface of hollow fibers by cutting the fibers at an inclined angle. It was found that the contact angle depended not only on the polymeric material but also on the surface morphology including nodule size and roughness parameters. The theoretical prediction showed that the measured contact angle would be greater than the value intrinsic to the membrane material, and the prediction was confirmed by experimental data. It was also theorized that this behavior was the consequence of the formation of composite structures at the membrane surface.

RÉSUMÉ

Les surfaces internes et externes de membranes de dialyse fibreuses et vidées furent caractérisées par la combinaison de deux techniques, soit par la mesure de l'angle de contact d'un liquide et par la microscopie à force atomique, le but étant à améliorer la biocompatibilité des membranes. Certaines propriétés de surface furent évaluées incluant l'énergie de surface, la rudesse, la grandeur de pores et la grandeur de nodules.

Des études d'angle de contacts furent poursuivies par l'observation de la ménisque se formant sur les surfaces intérieures des fibres. Un système d'imagerie équipé d'un protracteur goniomètre et d'une caméra vidéo fut développé pour ce travail. Des observations par microscope furent aussi entreprises pour étudier la surface intérieure des fibres en les coupant en angle incliné. Il a été déterminé que l'angle de contact du liquide dépend non-seulement sur la matière polymérique mais aussi sur la morphologie de la surface incluant la grandeur des nodules et la rudesse de la surface. La prédiction théorique a démontré que l'angle de contact mesuré serait plus grande que la valeur intrinsèque du matériel membraneux, et ceci fut confirmé par les données expérimentales. Il a aussi été théorisé que ce comportement était due à la formation de structures composites sur la surface de la membrane.

ACKNOWLEDGEMENT

The author wishes to express his sincere gratitude to Professor Takeshi Matsuura, for his continuous advice, encouragement, understanding and trust during the course of this research. Also, many thanks for his careful review of the manuscripts.

The author would also like to thank Dr. K.C. Khulbe for his guidance and cooperation, and Mr. Louis Tremblay for his technical support during this study.

Also, special thanks to Dr. Thanh Nguyen and Dr. Dibyendu De from Baxter Healthcare Int. (Renal Division, Miami Lakes, FL) for providing useful information and dialysis hollow fibers. The author is also grateful to the Baxter Healthcare Inc., and the Government of Ontario, for their financial support under the Ontario Graduate Scholarship in Science and Technology (OGSST).

Dedicated to my dear wife, Shideh for her love, unceasing support and strength

and

to my parents for their support and encouragement in all my undertakings.

TABLE OF CONTENTS

LIST OF TABLES

LIST OF FIGURES

NOMENCLATURE

List of Symbols

D_n	nodule size, nm
D_p	pore size, nm
$\Delta\rho$	density difference between the liquid and vapor phases, kg/m^3
e_{coh}	cohesive energy of solid, J/m^3
f (x, y)	surface function relative to the center plane
f_1	fractional surface areas of low-surface-energy region
f_2	fractional surface areas of high-surface-energy region
f_{SL}	fraction of the surface where solid and liquid are in contact
f_{LV}	fraction of the surface where liquid and vapor (air) are in contact
f_w	area fraction of solid surface wetted by the liquid
f_{nw}	area fraction of solid surface non-wetted by the liquid
g	acceleration due to gravity, kg m/s^2
Υ_{LV}	liquid-vapor surface tension, J/m^2
Υ_{SL}	solid-liquid surface tension, J/m^2
Υ_{SLE}	effective solid-liquid surface tension, J/m^2
Υ_{SV}	solid-vapor surface tension, J/m^2
h	height of liquid rise in hollow fibers, m
k	ratio of mean surface roughness to mean surface nodule size, (R_a/μ_n)
K	cantilever force constant, Nm-1
l	radius of nodules, nm

l_1	radius of the largest circle that surrounds the region between nodules, nm
l_2	radius of a circle that has the same area as that of the confined region, nm
L	sampling length in profilometer, μm
L_x	surface dimension in the x direction, nm
L_y	surface dimension in the y direction, nm
m	cantilever mass, μg
ν	resonant frequency, kHz
μ_n	mean nodule size, nm
μ_p	mean pore size, nm
r	average internal radius of hollow fibers, m
R	surface roughness or the ratio of the actual to the projected area.
R_a	mean roughness, nm
R_1	first principal radius of curvature at a point of the liquid surface, m
R_2	second principal radius of curvature at a point of the liquid surface, m
δ_{sp}	solubility parameter, $J^{1/2}\ m^{-3/2}$
σ_n	geometric standard deviation of nodule size
σ_p	geometric standard deviation of pore size
θ_e	equilibrium contact angle, degree
θ_i	intrinsic contact angle, degree
θ_{ap}	apparent contact angle, degree
θ_a	advancing contact angle, degree
θ_r	receding contact angle, degree

θ_c	Cassie contact angle for heterogeneous surfaces, degree
T_g	glass transition temperature, °C
T_m	crystalline melting temperature, °C
y	height of the roughness in profilometer, μm

Abbreviations

AFM	atomic force microscopy
ATIR	attenuated total internal-reflection spectroscopy
CA	cellulose acetate
CAM	contact angle measurement
DS	degree of substitution
ESRD	end-stage renal disease
ESCA	electron spectroscopy for chemical analysis
MCA	modified cellulose acetate
PEG	polyethylene glycol
PS	polysulfone
PVP	polyvinylpyrrolidone
SEM	scanning electron microscopy
SIMS	secondary ion mass spectrometry
SPM	scanning probe microscope
SSIMS	static secondary ion mass spectrometry
STM	scanning tunneling microscopy
TIPS	thermally induced phase separation
XPS	X-ray photoelectron spectroscopy

CONTRIBUTIONS

1- This research has been presented in an oral and a poster session at the 12th Annual Meeting of the North American Membrane Society in May 2001 in Lexington, Kentucky, USA.

2- An article on this study has been submitted to the Journal of Membrane Science for publication in November 2001.

Chapter 1

INTRODUCTION

1.1 Motivation

The surface and interfacial properties of membranes are important in a variety of biomedical applications, particularly in blood-contacting applications. One of the most important membrane applications is in hemodialysis process where membranes are used as artificial kidneys (Mulder, 1995). The main requirement for hemodialysis membranes is biocompatibility that is influenced by both membrane material and membrane surface properties.

Membrane surface characteristics appear to be important in coagulation and thrombosis, the two interrelated processes in blood "clotting". Assuming a pure membrane material, with no leachable toxic or biomedically active products, the major interfacial interaction appears to be adsorption of plasma proteins (Andrade, 1976). The plasma proteins adsorption properties seem to correlate with the materials' long-term blood "biocompatibility". It is known that several phenomena occur when blood comes in contact with foreign substances. First of all some of the proteins start depositing on the surface of the hollow fiber membranes followed by deposition of platelets and neutrophills. These cause the formation of thrombus and embolus. In recirculating blood, the thrombus and embolus may block the arteries in brain or heart and cause stroke.

Several studies indicated that the interfacial interactions between biological environment and biomaterial are mediated by the membrane surface properties such as hydrophilicity, and surface composition (Tsai and Lin, 2001). For example, it has been reported that membranes with smoother surfaces (surface roughness of a few nanometers) have a better biocompatibility (Tsunoda et al., 1999).

1.2 Problem Statement

A number of surface properties have been proposed to correlate with biocompatibility. These properties are tabulated in Table 1.1.

Table 1.1 Surface characterization of polymers for biocompatibility correlations (Andrade, 1976).*

General Class	Surface Property	Measurement	Investig-ator	year
Charge or Potential	Wettability	Visual observation	Lampert	1931
	Surface free energy, γ_s	Contact angle	Lyman	1965
	Critical surface tension,	Contact angle	Baier	1972
	Work of adhesion	Contact angle	Bischoff	1968
	Wettability spectrum	Contact angle and inter-molecular force calculations	Nyilas	1975
Surface Chemistry	Zeta potential	Streaming potential	Ross	1953
	Charge	Ion interactions	Hubbard & Lucas	1960
	Conductivity	Bulk Conductivity	Bruck	1973
Cleanliness	Functional groups	Direct synthesis	Falb	-
		Infrared spectroscopy	Baier	1970
	Impurities	Teflon test	Baier	1970

*This is a very brief summary table.

As is evident from Table 1.1, most investigators have considered only one surface property. Very little work has been done in attempting to measure a spectrum of surface properties and look for their correlation, if any, with protein adsorption and/or blood compatibility, although R.E. Baier and his collaborators have pioneered in the use of a variety of surface characterization tools for biomedical material surface. (Andrade, 1985)

During recent years, many surface-sensitive techniques such as atomic force microscopy (AFM), contact angle measurement (CAM), scanning tunneling microscopy (STM), X-ray photoelectron spectroscopy (XPS), and scanning electron microscopy (SEM), have been developed to analyze polymeric surfaces (Chan, 1994). Among these techniques, only a few have been applied to investigate the properties of the internal and external surfaces of dialysis hollow fiber membranes.

1.3 Scope of the Research

In the course of this research, two techniques have been developed for the characterization of the internal and external surfaces of dialysis hollow fibers used in artificial kidney, i.e. contact angle measurement (CAM) and atomic force microscopy (AFM). Despite the popularity and maturity of these techniques, they have not been applied to the inside and outside surfaces of dialysis hollow fibers. This was because of difficulties introduced by surface curvature and small size of hollow fibers (inside diameter =150-250 μm). The hollow fibers studied in this work were melt-spun polysulfone and cellulose acetate hollow fibers prepared under different spinning

conditions. These hollow fiber membranes were kindly supplied by Baxter Healthcare International, Miami Lakes, FL.

The objective of this study was to develop the surface characterization techniques applicable to the dialysis hollow fiber membranes. More specifically, the tasks involved in this study were:

1. To examine applicability of contact angle measurement (CAM) and atomic force microscopy (AFM) for surface characterization of dialysis hollow fiber membranes.

2. To study hollow fiber membranes' internal and external surface properties such as pore size, pore size distribution, nodule size, nodule size distribution, roughness, and wetting properties aiming at the development of novel hollow fibers with long-term biocompatibility and high performance.

3. To develop a theory capable of predicting the effect of membrane morphology on surface energetic.

Chapter 2

LITERATURE SURVEY

2.1 Hemodialysis

2.1.1 Background

Kidney disease is a major problem, affecting about 5 percent of the population and accounting for over 60,000 deaths per year in the United States. While the ideal solution is to give the patient a kidney transplant, this is not always possible due to the lack of suitable donors. To sustain the patient until a transplant is possible, the membrane-based hemodialyzer (artificial kidney) can be used. Over 85,000 Americans are currently sustained on the artificial kidney; perhaps 15,000 of them have conditions suited to very long-term support (Clark and Gao, 2001).

Hemodialysis is a rate-governed membrane process in which a microsolute is driven across a semipermeable membrane by means of a concentration gradient. The microsolute diffuses through the membrane at a greater rate than the microsolutes present in the feed solution. If the receiving solution (defined as dialysate) is not continuously renewed, the solute concentrations on the both sides of the membrane tend to equalize, negating the driving force for the separation. This is an essential difference between an equilibrium-based process and a rate-governed membrane process (Kessler and Klein, 1992).

In general, membranes used for separation processes span a wide range of applications. They can be categorized in the order of targeted particle size or molecular weight as shown in Fig.2.1.

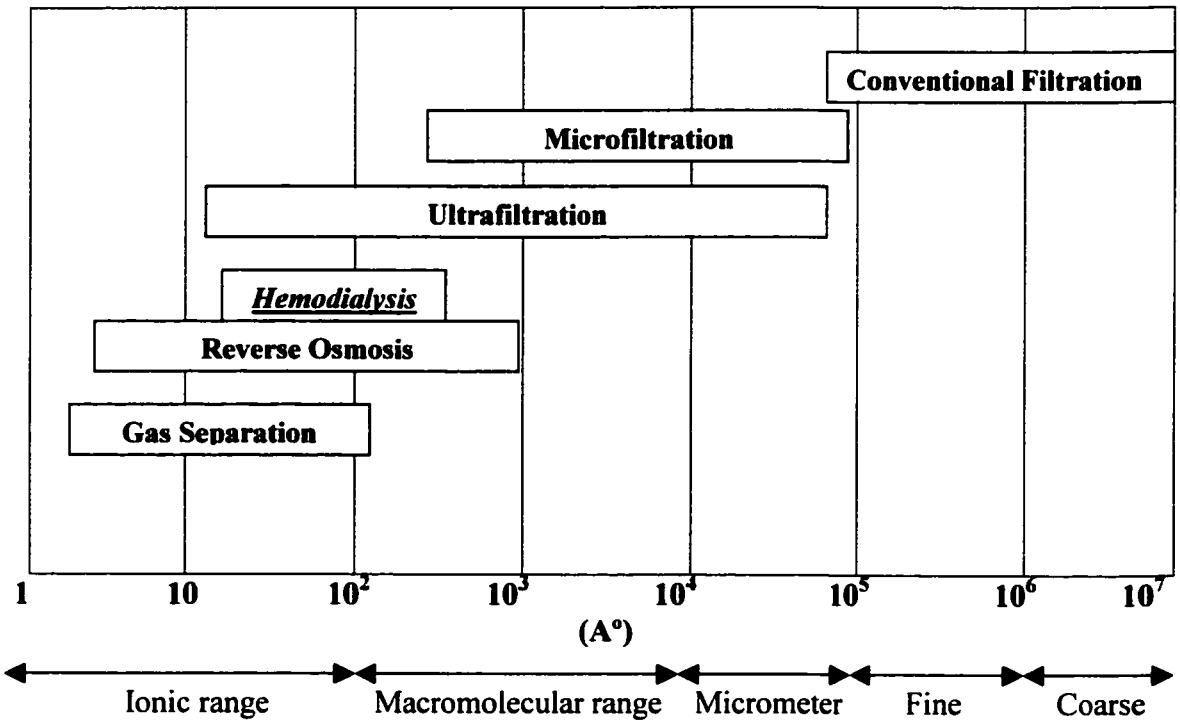

Figure 2.1 Spectrum of membrane separation applications and their respective range of average effective pore size (Elsen & Silva, 1993).

As is evident from Fig. 2.1, particle size ranges from approximately 10^{-10}m (1 A°) for gas separation to 10^{-3}m (10^{7} A°) for conventional filtration. Hemodialysis membranes are in the lower range of particle size or molecular weight spectrum such that the lower molecular weight end of ultrafiltration and hemodialysis membranes overlap.

2.1.1.1 Treatment of End-Stage Renal Disease

Once renal function decreases to less than approximately 5 % of normal, life can not be sustained without recourse to artificial means. Hemodialysis, the dialysis of a patient's blood against a physiological saline solution, replaces kidney function in three principal areas: removal of waste metabolites, removal of excess body water, and restoration of acid-base and electrolyte balances. The waste metabolites include urea, the end product of protein catabolism, and creatinine, the end product of muscle metabolism. In addition, it is thought that there are larger solutes (up to 13 k Dalton) that accumulate very slowly in end-stage renal disease (ESRD) patients and may have negative impacts on various metabolic regulatory mechanisms. In the literature these solutes are referred to as "middle molecules" for lack of better identification.

Patients with ESRD currently undergo treatment three times per week. The length of the treatment varies with the dialyzer used, the size of the patient, and the quantity of fluid the patient has retained since the preceding treatment. As a general rule, three to five hours of treatment will suffice for all patients.

2.1.1.2 Ultrafiltration Capacities

Hemodialysis membranes have ultrafiltration capacities ranging from 5 to 70 $mL/h.m^2$ mm Hg. Because of regulatory venous resistance (needle plus vein) ranging from 60 to 120 mmHg, and an additional blood channel resistance of 20 to 50 mm Hg, the minimum transmembrane pressure difference encountered is between 80 to 170 mmHg.

These values depend, of course, on the rate of blood flow employed. For low permeability dialyzers containing one m^2 of surface area, this predicts that ultrafiltration will produce 400 to 850 mL/h of fluid loss. With the more permeable dialyzers, the fluid loss can reach 4 to 8 L/h. Such high rates can produce fluid disequilibrium and are avoided in modern dialysate controllers by mechanical means (Kessler and Klein, 1992).

In one approach to the control of ultrafiltration, the dialysate controller provides balanced volumes of dialysate into and out of the shell side of the dialyzer. Introduction of a bias into this balance allows predetermined rate of ultrafiltration. Another series of dialysate controllers uses turbine flow meters to measure the rate of dialysate entering and leaving the device and then balances pressures to achieve predetermined rates of filtration. (Kessler and Klein, 1992).

2.1.1.3 Hemodialysis Module and Design Considerations

Hollow fiber hemodialyzers were first introduced in 1966 (Lipps et al., 1967). The external and internal structure of a typical unit is shown in Fig. 2.2.

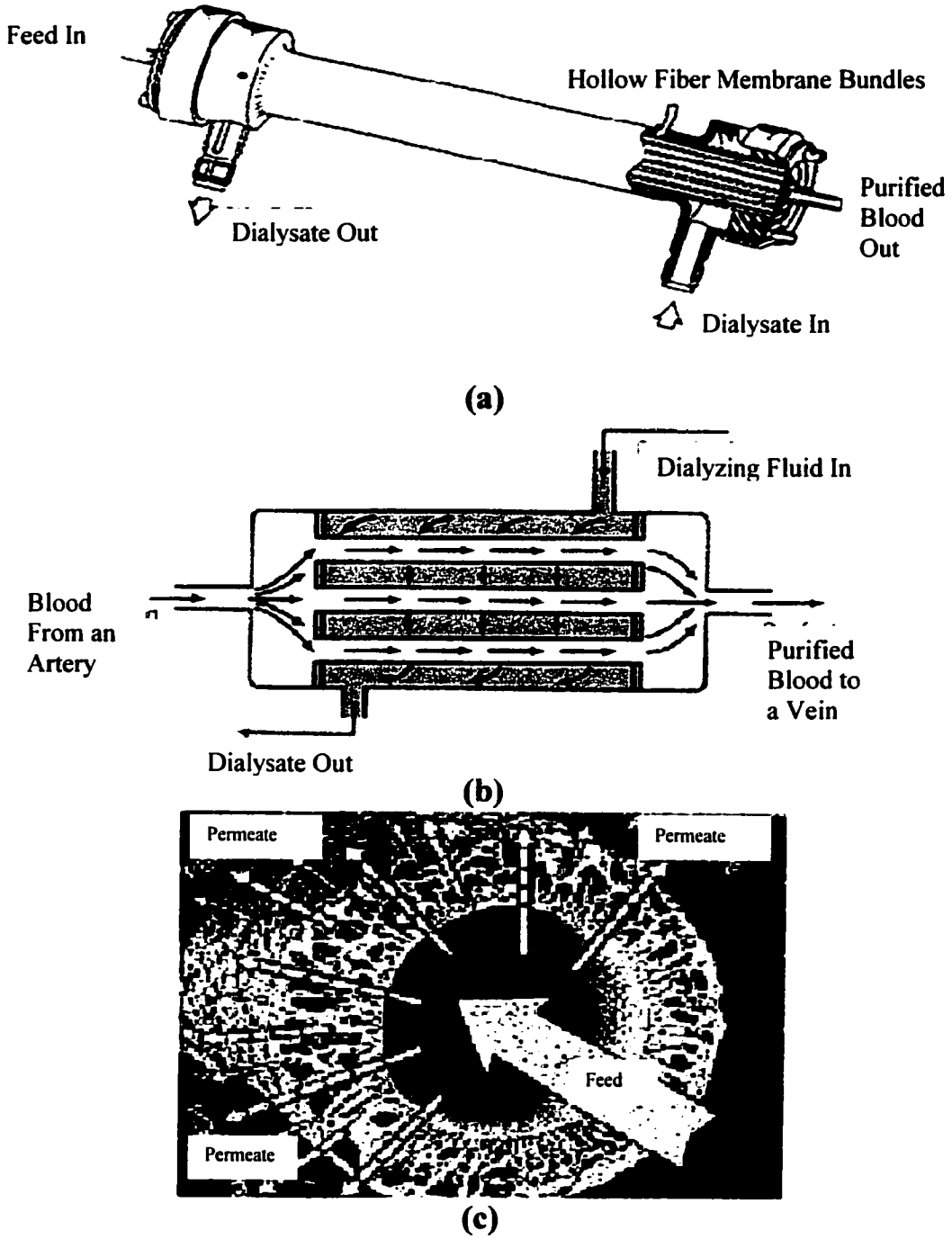

Figure 2.2 Typical hollow fiber hemodialyzer, (a) external structure (Kessler and Klein, 1992), (b) schematic internal structure (Felder and Rousseau, 2000), and (c) Cross sectional view and flow direction in a hollow fiber.

A bundle of hollow fibers is contained in a housing and encapsulated at each end forming tubesheets. At each end, a gasket and endcap form headers to direct blood flow in and out of the lumens of the fibers. Adjacent to each tubesheet is a circumferential header, which directs the dialysate flow in and out of the shellside space. The device is geometrically similar to a shell-and-tube heat exchanger. The housing and endcaps of these modules are usually fabricated from a transparent engineering polymer such as polycarbonate or poly (styrene-co-acrylonitrile). The encapsulant that forms the tubesheet is typically a polyurethane, and a low-Durometer elastomer such as silicone rubber is used for the gasket between the endcap and the tubesheet.

The hollow fiber dialyzer has achieved widespread acceptance and has largely supplanted other designs. This is due to the ease with which this design can be manufactured, its compactness, and its reliable performance in extra corporeal systems. While originally intended as disposable items, health care costs have provided incentive to reuse these dialyzers, but only with respect to a single patient. Due to the chronic, intermittent and life-sustaining character of hemodialysis therapy, hemodialysis membranes need to fulfill a long list of requirements in order to optimize treatment:

1. Biocompatibility.
2. Hemocompatibility: not inflict any damage to the formed elements of the blood and minimal activation of the body defense mechanisms to prevent indirect damage to the blood or other organs.

3. High diffusive permeability in the lower and middle molecular weight range (MW=1000-2000 Dalton) for effective removal of toxic metabolites of protein catabolism and correction of acid base status.
4. High sieving coefficients for toxic polypeptides that accumulate in the tissues of uremic patients (e.g. β_2-microglobulin).
5. Steep drop in sieving coefficient in the vicinity of the MW of albumin to prevent excessive albumin loss.
6. Sufficient hydraulic permeability to correct fluid overload.
7. High hydraulic permeability in case of high flux membranes.
8. Minimal backfiltration or backdiffusion.
9. No chronic or subchronic toxicity and therefore no or minimal release of residues from the manufacturing or sterilization process.

Constraints imposed by the fluid dynamics of blood and the operating conditions of a dialysis session have a heavy impact on the design of a hollow fiber dialyzer. For example, the hollow fiber internal diameter is always close to 200 μm to avoid excessive pressure drops across the blood side fluid path. The total surface area of a hollow fiber membrane is usually between 1 and 2 m^2. These design considerations which have led to a wide variety of dialyzers with very similar performance characteristics in the lower molecular weight range, have made it even more important to focus on ways to improve hemocompatibility through membrane design and to increase membrane permeability in the toxic polypeptide range (Elsen & Silva, 1993).

2.1.1.4 Interaction of Plasma Proteins with Foreign Surfaces

Whole blood carries within it two humoral defense mechanisms that have been found to be of importance in extra corporeal treatment. The first is coagulation defense system that protects us from excessive blood loss when the vascular tree is damaged. The second is the complement system that identifies—for subsequent attack and destruction—foreign bodies that have entered the circulation. The latter may be bacteria, viruses, or synthetic surfaces, which can complement coagulation cascade. Each of these defense mechanisms is complex and they can operate interdependently.

The mechanism of initiation of coagulation cascade by synthetic surface is still a matter of debate. Two observations are important. Very hydrophilic surfaces, such as poly(ethylene oxide) gels or regenerated cellulose, appear to trigger this mechanism only minimally. Very hydrophobic surfaces may or may not initiate the cascade, depending on the protein adsorption that occurs—and whether or not such proteins are denatured following adsorption. As a practical matter, all patients undergoing hemodialysis are given intravascular injections of heparin, a glycosaminoglycan, which catalyzes the destruction of fibrinogen. The latter is a necessary precursor to the formation of thrombin, the cloth-forming protein (Kessler and Klein, 1992).

The immune protection system is thought to operate via an enzymatic cascade, which eventually assembles an attack complex at the surface of the foreign body. An intermediate product, C5a, signals monocytes and neutrophils to produce stimulants for subsequent cellular attack of the foreign material. Although most synthetic membranes

are not subject to enzymatic degradation, they can stimulate the cascade to occur. The by-product of such stimulation is the release of the proteins that produce the characteristics of an inflammatory reaction. That is, the presence of the synthetic surface fools the defense mechanism into activating and wasting its enzymatic and oxidative burst defenses.

2.1.1.5 Membrane Materials used in Hemodialyzers

Both natural and synthetic polymers or copolymers are commercially available for manufacturing hemodialysis membranes. The natural polymers are based on cellulosic polymers and synthetic polymers are derived from petrochemicals. Cellulose is obtained from either wood pulp or cotton linters. When a dialysis membrane separates two aqueous phases, the problem of material choice is relatively simple. Clearly, the membrane pores must be filled with water during use, so wettability is a primary consideration. As a consequence of this requirement, the predominant materials for dialysis membranes are relatively hydrophilic polymers. At one end of the spectrum are cellulose and poly(ethylene-co-vinyl alcohol) (Eval), and on the other end poly(methylmethacrylate), the latter pre-wetted by the manufacturer. In between fall cellulose acetate with a degree of substitution (DS) of 2.5, poly(acrylonitrile-co-methallylsulfonic acid), and other acrylonitrile copolymers.

The use of polysulfone membranes (PS) for hemodialysis would appear to be a contradiction to the wettability requirement, but many dialyzers made from this material

contain a small amount of poly(vinylpyrrolidone)(PVP) as an alloying agent to the PS. The PVP provides the requisite wetting, although there may still be very small diameter pores that are inactive during dialysis because of the exclusion of water (Kessler and Klein, 1992). The polymers used as starting materials for membrane manufacturing are divided into three basic categories:

1. Hydrogel polymers, such as cellulose, chitosan, and poly (vinyl alcohol). The characterizing features of these polymers include high equilibrium water contents, large swelling values when cycled from dry to water wet state, and uniform cross sectional structures.
2. Glassy engineering plastics, such as poly(amides), poly(sulfones), poly(ethersulfone), poly(carbonate), and poly(dimethyl phenyleneoxides). These polymers are characterized by low equilibrium water contents and very strong hydrophobic interactions. They may be semicrystaline.
3. There are a number of vinyl copolymers, including copolymers of acrylonitrile, or charged derivatives of engineering plastics, such as sulfonated polysulfone, which exhibit some properties characteristic for the first two categories described above. For example, a copolymer of acrilonitrile and sodium methallyl sulfonate used for hemodialysis has a significant equilibrium water content, approaching the values typical for hydrogels, but also has a strong adsorptivity for human serum albumin, characteristic of the hydrophobic bonding properties encountered when the engineering plastics are used to prepare membranes.

Table 2.1 lists the majority of the hollow fiber membranes currently used for the fabrication of hemodialyzers, together with the manufacturer and the spinning technique.

Table 2.1 Raw materials and fabrication method of hollow fiber membranes for hemodialysis manufactured by various companies (Elsen & Silva, 1993).

Company	**Material**	**Fabrication Method**
Amicon	Polysulfone	Solution spinning
Asahi	Cellulose, Polyacrylonitrile	Solution spinning
Baxter (Althin)	Cellulose, Cellulose acetate,	Melt-spinning
Baxter (Althin-R&D)	Polysulfone	Melt-spinning
Enka	Cellulose, Cellulose acetate	Solution spinning
Fresenius	Polysulfone	Solution spinning
Gambro	Polyamide, Polycarbonate	Solution spinning
Hospal	Polyacrylonitrile	Solution spinning
Kurary	Ethylene-vinyl alcohol	Solution spinning
Minntech	Polysulfone	Solution spinning
NMC	Polysulfone	Solution spinning
Terumo	Cellulose	Solution spinning
Toyobo	Cellulose acetate	Solution spinning

Cellulose acetate (CA) and polysulfone (PS) polymers are the most widely used polymers in artificial kidney. Both of them are classified as condensation (step-growth) polymers.

2.1.1.5.1 Cellulose Acetate

Cellulose acetate is the most important ester derivative of cellulose. Cellulose is an abundant naturally occurring polymer. This polymer represents about one-third of all plants. Although found widely in nature, commercial cellulose is almost derived entirely from cotton and wood. Cotton is composed of about 89 % cellulose. Wood contains about 40-50 % cellulose with the remaining being lignin and lower molecular-weight polysaccharides. Treatment of wood pulp with acid and steam followed by basic sodium sulfide yields a product that is 92-98 % cellulose. Cellulose acetate is produced by acetylating of cellulose using acetic anhydride in acetic acid in the presence of a strong acid catalyst (usually sulfuric acid). This reaction is shown in equation 2.1. In this equation, **P** represents a polymer molecule minus the functional group of interest and **P~~OH** specially represents cellulose molecule.

$$\underset{\text{Cellulose}}{\mathbf{P\sim\sim OH}} + \underset{\text{acetic acid}}{\mathbf{HOCOCH_3}} \Leftrightarrow \underset{\text{cellulose acetate}}{\mathbf{P\sim\sim OCOCH_3}} + \underset{\text{water}}{\mathbf{H_2O}} \qquad (2.1)$$

2.1.1.5.2 Polysulfone

The polysulfones are transparent, amorphous polymers but possess good mechanical properties due to the rigid polymer chains. The *glass transition temperatures* are in the 180-230 °C range. The resistance of polysulfones to aqueous environments, including acids, bases, and oxidants, is excellent. The very good thermal and hydrolytic stability of polysulfones make them useful for microwave cookware and in medical, biological, and food processing industries. Other applications include circuit breakers, electrical connectors, battery cases, camera bodies, aircraft interior parts, and membrane supports for reverse osmosis. Outdoor use is somewhat limited because of relatively low UV stability (Odians, 1991).

Polysulfones are synthesized by nucleophilic aromatic substitution between aromatic dihalides and bisphenolate salts. This is shown in the following equation, where X is halogen, Y is SO_2 or C=O and Ar is phenyl group (Odians, 1991).

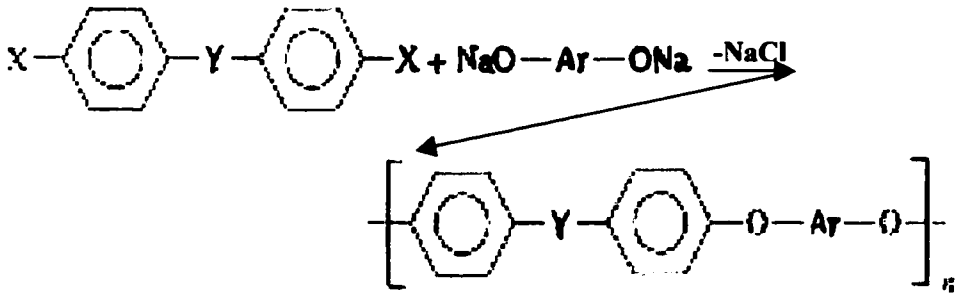

(2.2)

2.1.1.6 Manufacturing Processes of Hemodialysis Hollow Fiber Membranes.

Membrane characteristics are not only defined by the material but also by the manufacturing process. This becomes evident when comparing different membranes from the same polymer in terms of biocompatibility, ultrafiltration, diffusive and convective capacity. The reason for this is that the manufacturing process defines the microstructure of the membrane by which all the performance parameters of a dialyzer are primarily governed (Nguyen and Ericsson, 1999). Solution spinning and melt-spinning are the two techniques used to prepare hemodialysis hollow fiber membranes.

2.1.1.6.1 Solution Spinning Process

In solution spinning the desired polymer or copolymer is dissolved in a chemical solvent and this solution is spun into hollow fibers using an annular single hole spinneret. In this process, a lumen-filling medium (core liquid) is used to inflate the hollow fiber as it is spun. Generally, the core liquid contains a chemical solvent or a mixture of chemical solvents. The hollow fibers pass through a coagulation bath, which is a non-solvent for the polymer matrix. Generally, water, a chemical solvent, or a mixture of chemical solvents and water are used. After the coagulation bath, the fibers pass through various washing steps to remove all chemical solvents or any other leachable material from the polymer matrix. After removing all the solvents, the hollow fibers are replastisized with a mixture of glycerol with water or alcohol.

After solution spinning, the hollow fiber contains a core liquid. It is very difficult to remove the core liquid during the fiber washing process. Most often, manufacturers use fluro carbons such as Freon. Freon is a very good chemical solvent to solubilize other chemical solvent, but the use of Freon as core liquid remover has become increasingly controversial and a replacement is necessary because of the world ban on Freon application (Elsen & Silva, 1993).

The schematic representation of the solution spinning technique is illustrated in Fig. 2.3.

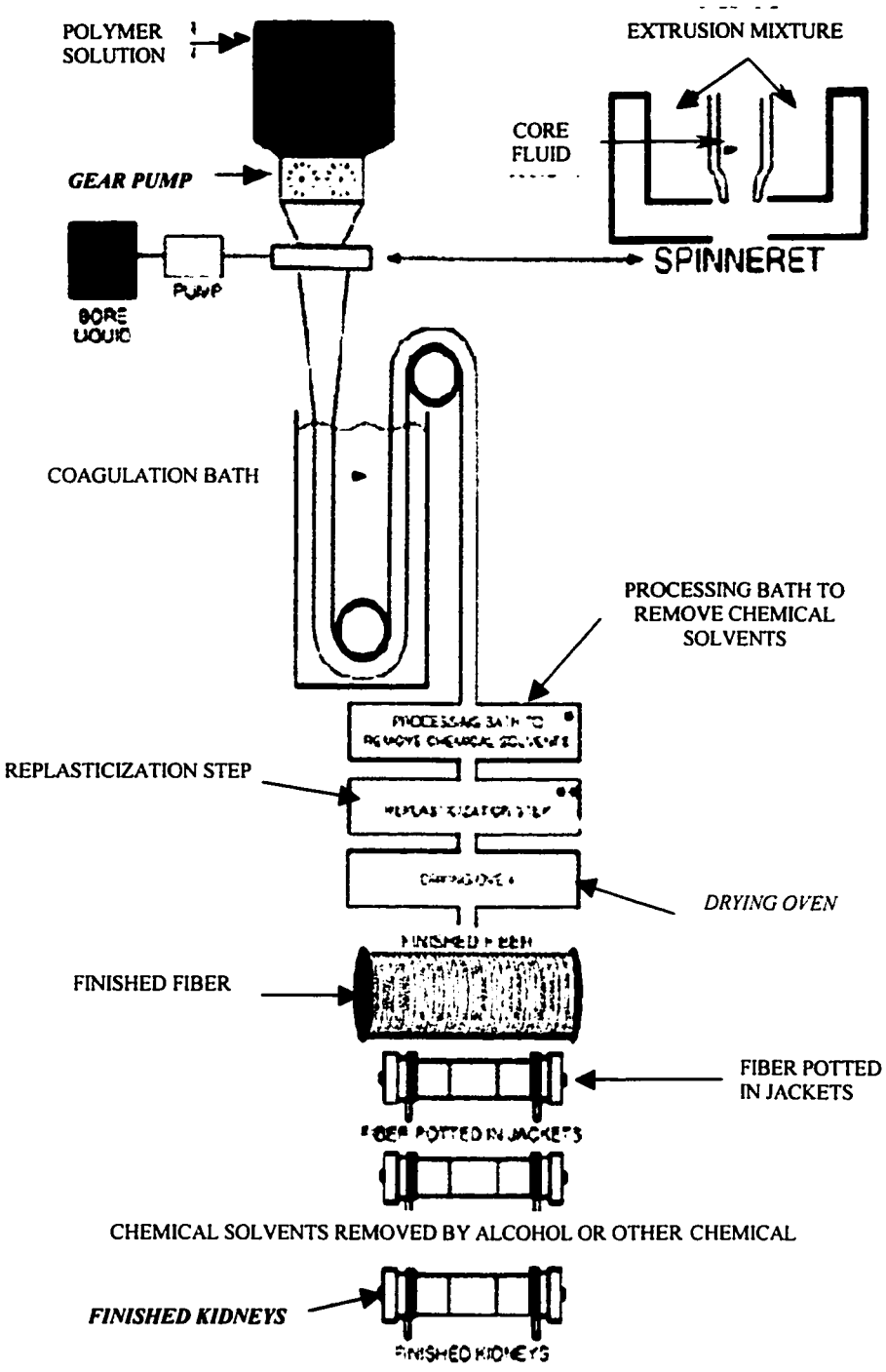

Figure 2.3 Generic flowchart of hollow fiber solution spinning process (Elsen & Silva, 1993).

2.1.1.6.2 Melt-spinning Process

With the melt-spinning process, the polymer blend is extruded close to its melting temperature forming hollow fiber membranes using an annular spinneret. During this process, an inert gas such as nitrogen is used as core gas to keep the fiber lumen open and air-cooling is used as coagulation medium. Further process is accomplished by water. The advantage of this process is that the hollow fibers are free of any potentially toxic chemicals such as solvents and core fluids.

The total absence of solvents or other potentially toxic solution during melt-spinning and further processing produces fibers that are totally free of toxic residuals. This is a distinctive advantage of melt-spinning compared to solution spinning particularly for biomedical applications of membranes such as hemodialysis (Elsen & Silva, 1993).

2.1.1.7 Membrane Structure

Membrane structure and morphology provide important distinction between dialytic membranes. For instance, all of the performance parameters of a dialyzer are primarily governed by the microstructure of the membrane. The first choice is to make a membrane as thin as the material will allow, while still providing the requisite mechanical stability for potting and pumping pressures. In addition to being thin, the membrane must provide the required morphology, i.e., porosity and pore size. These are

often conflicting demands. High porosity implies reduced load bearing elements in the cross section and, thus, limited tensile strengths. Fortunately, the more hydrophilic materials, such as cellulose and copolymers of vinyl alcohol, can be produced as thin, highly efficient hydrogel membranes reinforced by crystalline regions. The more hydrophobic, glassy polymers, such as polysulfones, are produced in asymmetric form to provide a thin solute-resistant skin supported by a more porous substructure. The thick substructure provides the mechanical support needed.

Asymmetric membrane structures are produced by the coagulation process used to convert a solution of polymer into a membrane structure. The phase-separation mechanisms that occur as the polymer is precipitated from the concentrated solutions include liquid-liquid and liquid-gel transitions. The skin is thought to be caused by a rapid loss of solvent from the polymer solution film into the coagulating bath. The resulting highly concentrated polymer solution precipitates with a morphology different from the underlying polymer solution since the initially coagulated surface acts as a barrier to transfer of the solvent out of—and non-solvent into—the lower layers of the solution. For the production of asymmetric dialysis membranes, the control of such phase separation mechanisms becomes rather critical because of the added demand for thin cross sections in dialytic applications (Kessler and Klein, 1992). A typical microstructure of a polysulfone hollow fiber dialysis membrane is shown in Fig. 2.4.

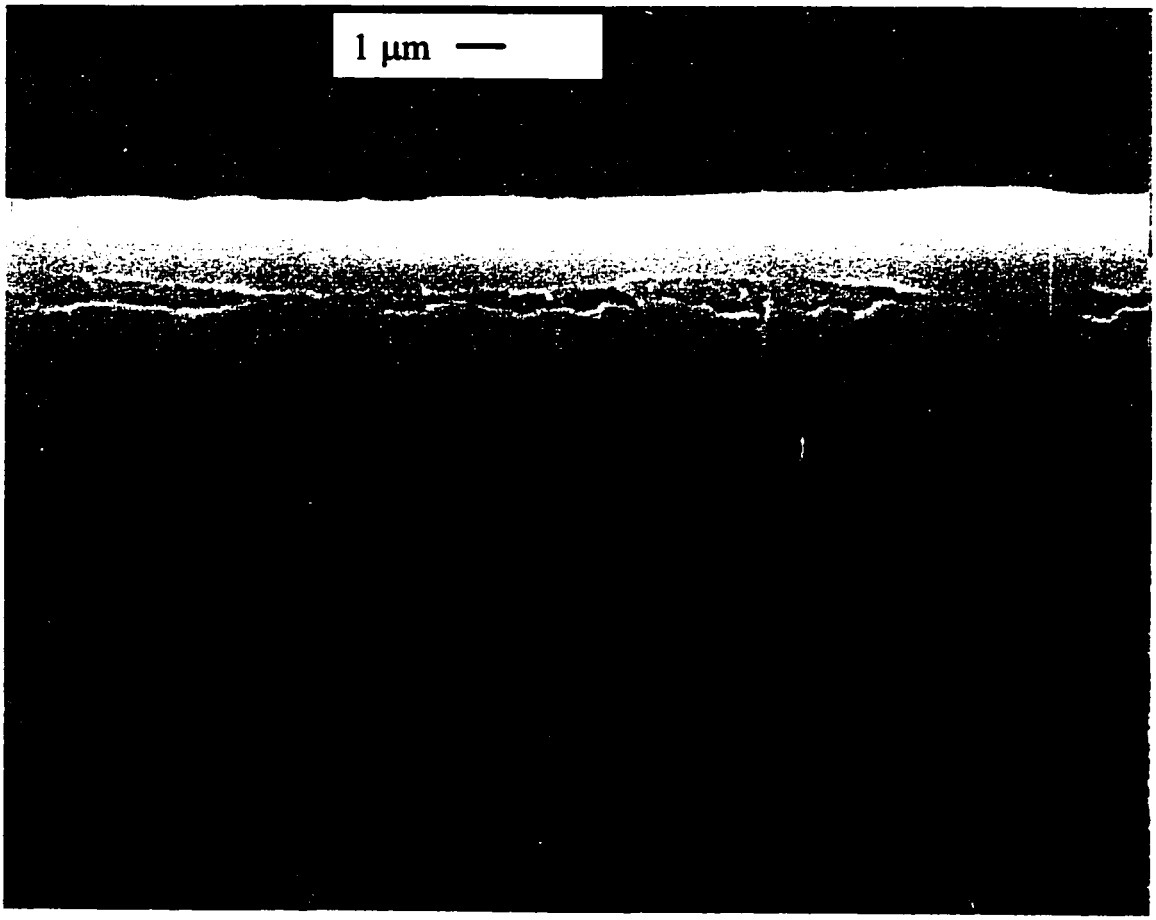

Figure 2.4 *SEM* image of the external skin layer of an asymmetric PS hollow fiber dialysis membrane.

2.2 Polymer Surface Characterization and Modification

2.2.1 Background

Polymers have been applied successfully in the fields such as membrane, biomaterials, protective coatings, friction and wear, composites, microelectronics devices, and thin-film technology. In general, special surface properties such as chemical composition, hydrophilicity or hydrophobicity, roughness, crystalinity, conductivity, lubricity and cross-linking density are required for the success of these applications. In recent years, many advances have been made in developing surface characterization and treatment techniques to analyze and alter the chemical and physical properties of polymer surfaces without affecting bulk properties (Chan, 1994). These techniques have been applied to achieve the following purposes:

1. Modify surface morphology by changing surface roughness or crystallinity
2. Increase hydrophobicity or hydrophilicity
3. Produce special functional groups at the surface for specific interactions with other functional groups.
4. Increase surface energy
5. Improve chemical inertness
6. Introduce surface cross-linking
7. Remove weak boundary layers or contaminants
8. Increase surface electrical conductivity
9. Increase surface lubricity

Improvement in surface modification techniques cannot be made without an in-depth understanding of the physical and chemical properties of polymer surfaces. The nature and the concentration of the functional groups introduced by different surface modification techniques must be determined. Such results will advance our understanding of various surface modification mechanisms.

The level of surface treatment must also be controlled if optimal results are to be obtained. For example, in printing, the polymer films should be wettable so that ink can be transferred onto the surface, but not wettable enough to induce smearing in printed images. Hence, it is obvious that polymer surfaces and modified surfaces must be characterized at the *molecular level*. Techniques commonly used for characterization of bulk properties are not suitable because only the properties within the first few nanometers of the surface are important for success.

It is important to point out that the structure and chemical properties of polymeric surfaces are not necessarily invariable but may depend on time and environment. The surfaces of homopolymers, copolymers, and polymer blends, which may have properties very different from their bulk, are good examples of this effect. Functional groups of homopolymers and block copolymers tend to restructure or reorient in response to different environments. The low-energy components tend to migrate to the polymer-air interface as a result of the thermodynamic drive to minimize the surface energy. In an aqueous environment, the hydrophilic groups are attracted to the surface, as shown in Fig. 2.5. Such changes can occur in the top few tenths of a nanometer of the surface.

Contact angle data, which are extremely surface sensitive, are frequently used to monitor migration of functional groups at polymer surfaces (Chan, 1994).

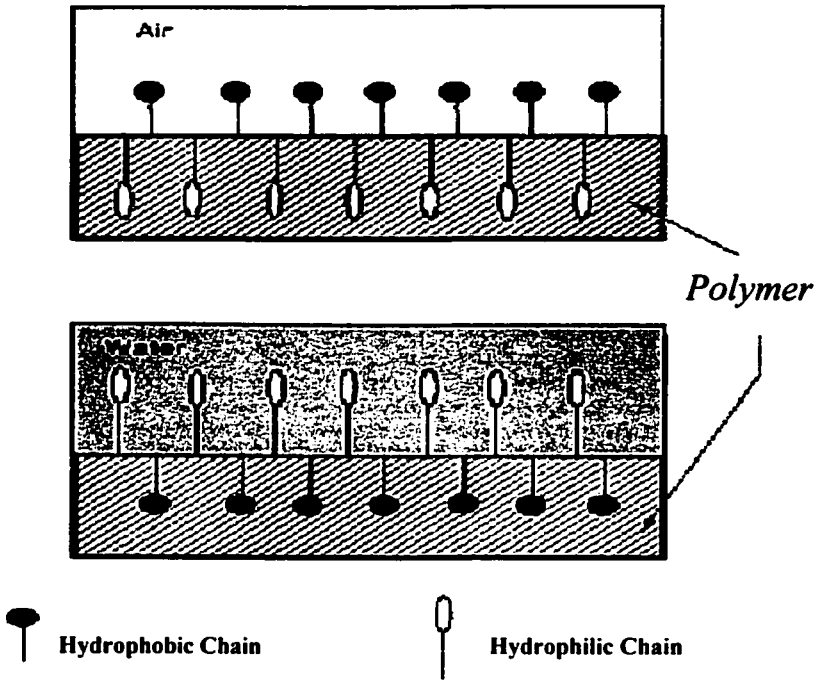

Figure 2.5 Segregation of hydrophobic groups occurs at the air-polymer interface, and segregation of hydrophilic groups occurs at the water polymer interface (Chan, 1994).

2.2.2 Polymer Surface Characterization Techniques

During recent years, many surface-sensitive techniques such as atomic force microscopy (AFM), scanning tunneling microscopy (STM), secondary ion mass

spectrometry (SIMS), X-ray photoelectron spectroscopy (XPS), scanning electron microscopy (SEM), and contact angle measurements have been developed to analyze polymer surfaces. Among these techniques, XPS and SIMS, which can provide surface chemical and structural information, have been most widely used by scientists and engineers in both academia and industry. (Chan, 1994).

Before investigators can choose the appropriate technique(s) for the analysis, they need to understand the limitations and capabilities of each technique, and they must be able to identify the information that is relevant to the analysis. Several important factors must be considered in choosing a surface analyzing technique, namely, sampling depth, surface information, analysis environment, and sample suitability. When surface sensitive techniques are involved, the first important consideration is what surface information is needed. Each technique supplies different and often complementary information. The choice of a suitable technique(s) is affected by many factors, and it is difficult to set up rules to zero in on a choice. When high-resolution, three-dimensional images are needed, AFM, and SEM are the appropriate techniques. When chemical analyses demand the most surface–sensitive probe, contact angle measurements and static SIMS (SSIMS) are good choices. If quantification and chemical state information were important, XPS would definitely be a candidate. If one is investigating a small amount (ppm) of impurity in a sample, then SSIMS is a good choice. The following is a brief description of the above-mentioned techniques.

2.2.2.1 Atomic Force Microscopy (AFM)

The atomic force microscopy was invented by Binnings, Quate, and Gerber in Switzerland in 1982. Similar to a scanning tunneling microscope, it can produce three-dimensional images of solid surfaces at very high resolution. The advantage of using AFM is that it can image non-conducting samples such as polymers and ceramics. A typical commercial AFM consists of a piezoelectric scanner, which controls scanning motion, an optical head, which senses cantilever deflection, and a base, which supports the scanner and the head and includes a circuit for the deflection signal (Chan, 1994). It operates by scanning across the surface with a sharp tip, with diameter between 1 and 20 nanometer, mounted on a soft cantilever spring of between approximately 0.001 and 0.2 Nm^{-1}. The tip and cantilever are micro fabricated from silicon, silicon oxide, or silicon nitride. It is important that the cantilever is insensitive to vibrations and acoustic noise from the laboratory. Hence it is chosen to have a natural resonant vibration frequency as far removed from those experienced in buildings as possible. As the resonant frequency (ν) is given by the classical results

$$\nu = \frac{1}{2\pi}\sqrt{\frac{K}{m}} \tag{2.3}$$

Where K is the cantilever force constant and m its mass. In order to obtain the highest resonant frequency, cantilevers are made with very low masses, typically around 1 μg, with low force constant (K= 0.004 Nm-1 yields a resonant frequency of 8 kHz).

The AFM tip, when brought into contact with a surface, experiences a very small force (of the order of nanoNewtons) because of interaction with the surface atoms. In this

mode, known as the "contact mode", the tip is scanned at a tip-sample separation corresponding to a chemical bonding length of the tip/sample combination. This leads to the cantilever being either attracted or repelled as it is scanned across the surface. The repulsive force at very small tip-surface separations originates from both nuclear and Pauli repulsions as closed electronic shells of surface and tip atoms are forced to interpenetrate. The attractive force arises as a result of decrease in potential energy of the system caused by chemical bonding through electron overlap between tip /surface atoms. The deflection of the cantilever may be sampled (force imaging) or kept constant using a feedback loop to keep the force at a pre-set value (constant force topography). Figure 2.6 illustrates the principle of operation of AFM (Attard and Barnes, 1998).

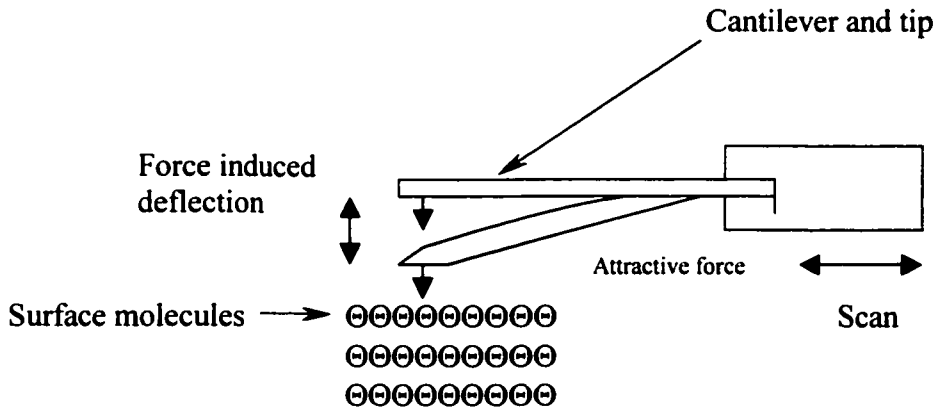

Figure 2.6 Schematic showing the principle of atomic force microscopy (AFM)

The deflection of the cantilever may be monitored by an optical technique such as that shown in Fig. 2.7 in which a laser beam is reflected from the back of the cantilever onto a segmented photodiode detector. As the sample is scanned across the tip, the

deflections in the beam arise from changes in local surface topography or "stiffness", i.e. a soft area of the sample that is easily deformed by the tip will appear as a cavity or pit in the AFM image. The feedback signal is used to control the height of the piezoelectric crystal as the sample is scanned. The height of the piezoelectric crystal is related directly to the topography of the sample surface.

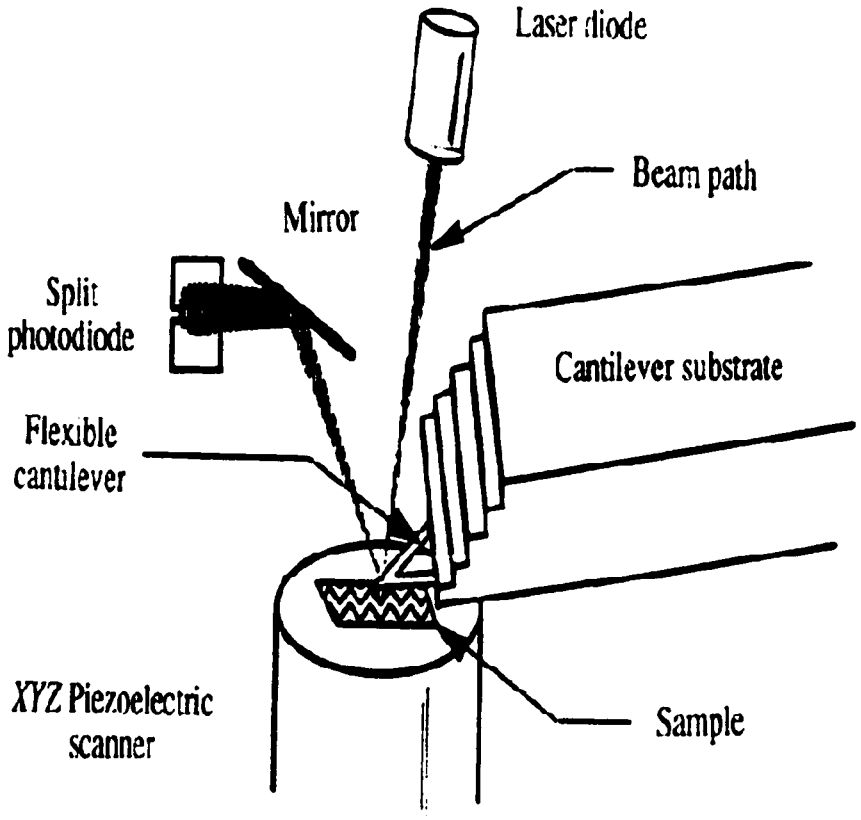

Figure 2.7 *Tapping mode* and *AFM* optical sensing system (Digital Instrument, Inc.).

A second mode of scanning, known as the "non-contact mode", may also be used. This is particularly important for delicate samples, which may be damaged by imaging in the contact mode. In this case the tip is not in contact with the surface since no electron cloud overlap occurs. The forces are electrostatic in origin (or magnetic if the tip/sample combinations are magnetic) and are even smaller than in the "contact mode". In order to enhance the sensitivity of the technique the tip is forced to vibrate close to its resonance frequency and hence this method is often referred to as the "tapping mode". Variations in the sample-tip forces will alter the resonant frequency of the tip, and this frequency shift is used to give a measure of the magnitude of the forces in action. Obviously, for a surface protrusion, the forces acting on the tip will be large so, once again, topographic images of surface force versus lateral position on the surface are possible even with non-conducting samples (Attard and Barnes, 1998).

2.2.2.2 Scanning Tunneling Spectroscopy (STM)

Scanning tunneling spectroscopy, invented by G.Binning and H.Rohrer at IBM in 1982, reveals high-resolution, three-dimensional pictures of the surface of a conductive sample by measuring the tunneling current between the probe and the sample when the tip is scanned over the surface. Figure 2.8 illustrates schematically the components of a scanning tunneling microscope.

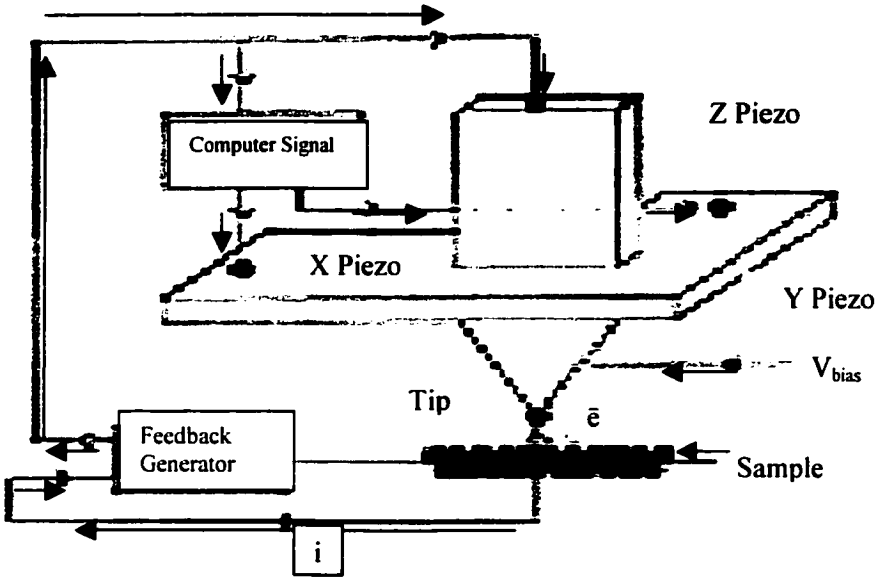

Figure 2.8 Experimental apparatus used in STM (Attard and Barnes, 1998).

The tunneling current changes potentially with the distance between the tip and the sample. As a result of this relationship, the tunneling current is an excellent parameter for sensing tip to sample separation. When STM is used to study polymer surface structures, special sample preparation is necessary. A thin conducting layer of Au, Cr, or Pt and C mixture is deposited on the surface of the sample. Piner et al. show that an approximately 10 nm Au coating or 2 nm Cr coating is sufficiently conductive to allow reliable operation of STM. Figure 2.9 shows a STM image of a gold –coated polyethylene crystal that has five plates stacked one on the top of the other; the height of each plate is approximately 11 nm (Chan, 1994).

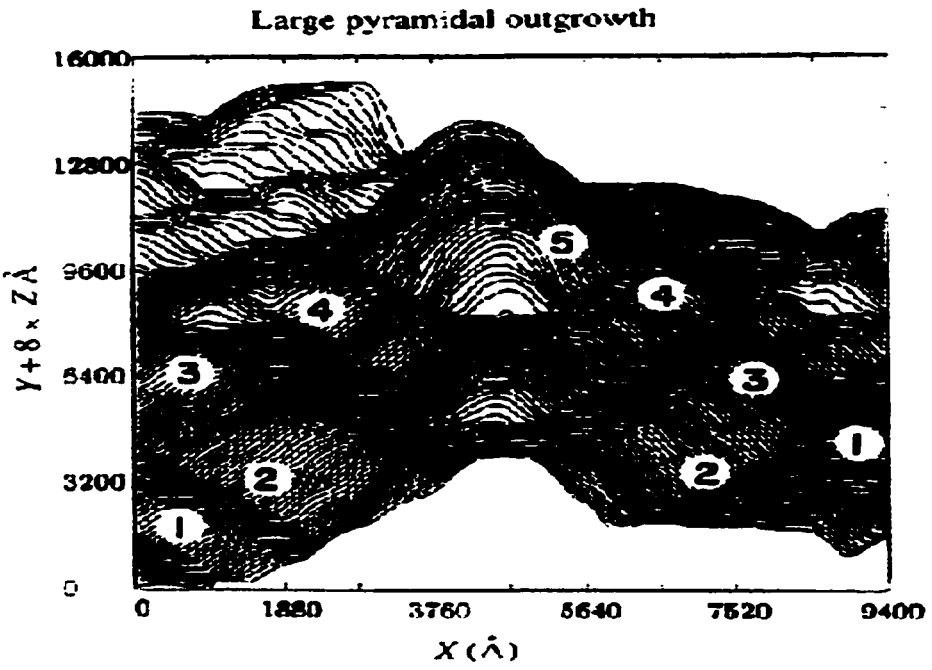

Figure 2.9 A STM scan of a gold-coated polyethylene crystal. The crystallite comprises of five layers of lamella each with a characteristic thickness of 11 nm (Chan,1994).

2.2.2.3 Scanning Electron Microscopy (SEM)

SEM has been playing an important role in determining microstructures of polymers. When an electron beam impinges on a sample, backscattered electrons, secondary electrons, and X-rays are produced. The primary electron beam can be focused down to nanometer scale. High-energy electrons are used to obtain high spatial resolution, whereas low-energy electrons are used to increase surface detail. Secondary electrons, which are emitted from a surface with low energy (<50 eV), can be easily detected by a scintillator detector. They are primarily produced within the top few

nanometers of the sample. Backscattered electrons are of high energy and come from a depth of one μm or more. They can give atomic number contrast (heavy elements appear bright and light elements appear dark) and topography contrast.

However, this technique is not very useful for elements with atomic number below 10. High-resolution SEM, which requires high-energy electrons, is almost impossible with polymers because high-energy electrons can cause structural and chemical changes at polymer surfaces. To minimize beam damage, polymer samples are usually coated with a metal such as gold (Chan, 1994). Figure 2.10 shows a schematic illustration of a scanning electron microscope.

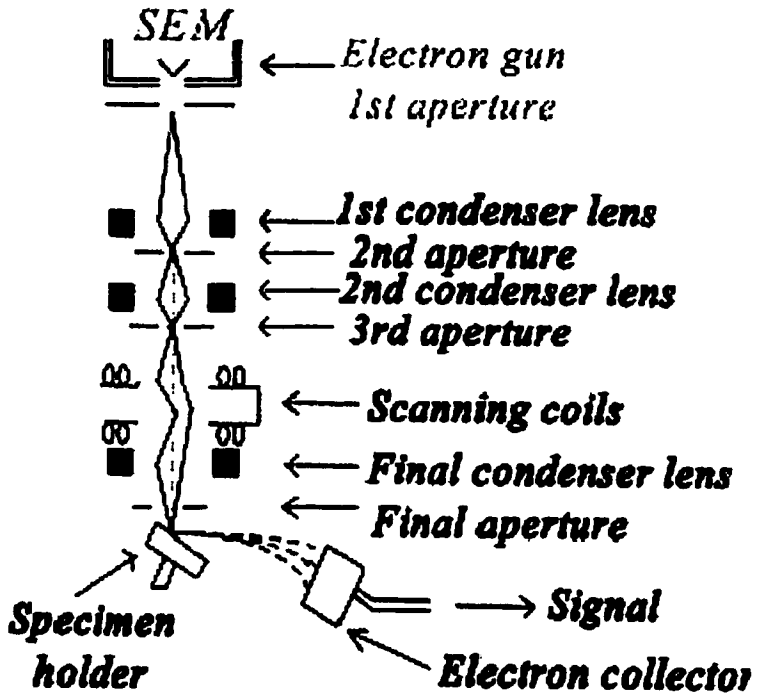

Figure 2.10 Schematic illustration of scanning electron microscope (Tan, 1999).

2.2.2.4 X-Ray Photoelectron Spectroscopy (XPS)

X-ray photoelectron spectroscopy, which is also known as electron spectroscopy for chemical analysis (ESCA), is probably the most widely used technique in characterization of polymer surfaces. In this technique, which was initially developed by Professor Kai Siegbahn at the University of Uppsala, a sample is irradiated by a beam of X-rays. The interaction between an X-ray photon and the inner-shell electron of an atom causes a complete transfer of photon energy to the electron. The electron then has enough energy to escape from the surface of the sample. This electron is referred to as the photoelectron. (See Fig.2.11)

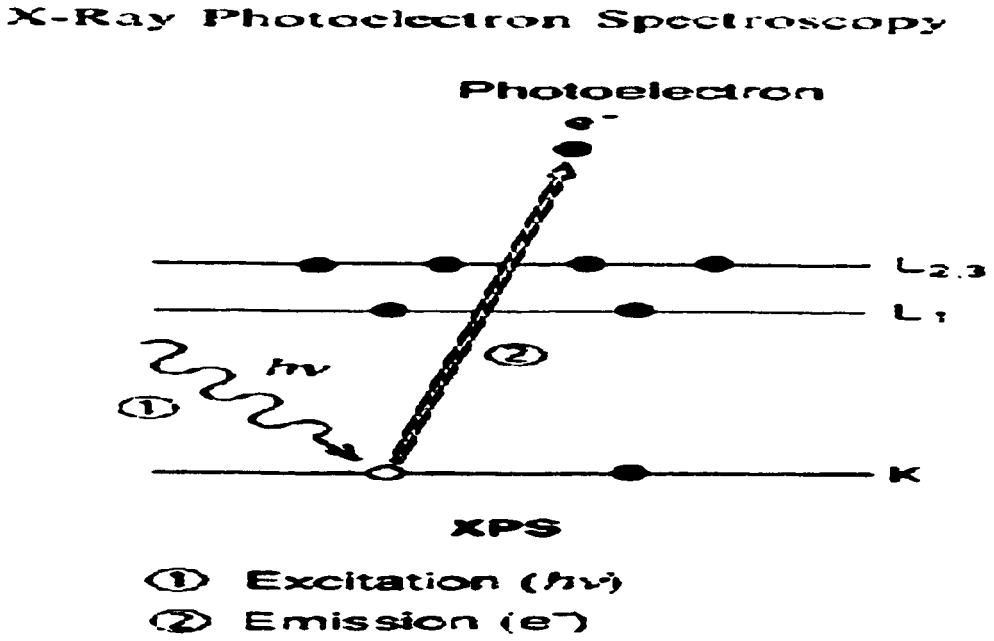

Figure 2.11 Schematic diagram showing XPS processes (Chan, 1994).

The kinetic energy of the photoelectron is measured by an electron energy analyzer. The difference between the kinetic energy of the photoelectron and the X-ray photon yields the binding energy of the inner-shell electron. Knowing the binding energy of an inner-shell electron allows identification of the element. The binding energy of an inner-shell electron is also sensitive to the electronic environment of the atom. When the atom is bound to atoms of different elements of differing electro negativity, the binding energy may increase or decrease. This change in binding energy is called the chemical shift, which can be used to provide structural information for a molecule. An XPS set up is shown in Fig. 2.12.

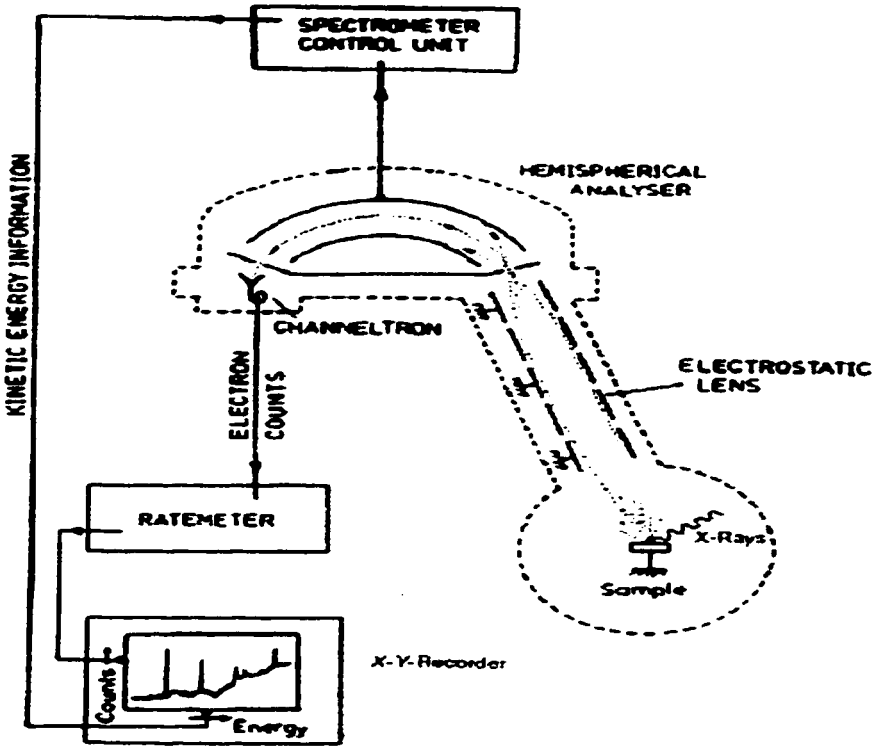

Figure 2.12 Schematic diagram of an XPS spectrometer (Chan, 1994).

2.2.2.5 Contact Angle Measurements (CAM)

2.2.2.5.1 Background

Contact angle measurement is perhaps one of the most known surface analysis techniques. In contact angle measurement, the behavior of a liquid on a solid surface is characterized. When a liquid is placed in contact with a solid surface, the bare surface of the solid adsorbs the vapor of the liquid until the volatility of the adsorbed material is equal to that of the liquid. When equilibrium is established, there is an interface between liquid and solid phases. The tangent angle between solid and liquid is known as the contact angle. In the other words, when a drop of liquid is placed on a solid surface and the surface tension of the liquid is larger than the surface tension of the solid, it makes a definite angle of contact between the liquid and the solid phases. When the same liquid is placed on surfaces of increasing surface tension, the contact angle decreases as the surface tension of the solid increases, as shown in Fig. 2.13. Finally, total wetting ($\theta = 0$) occurs if the surface tension of liquid is smaller than the surface tension of the solid.

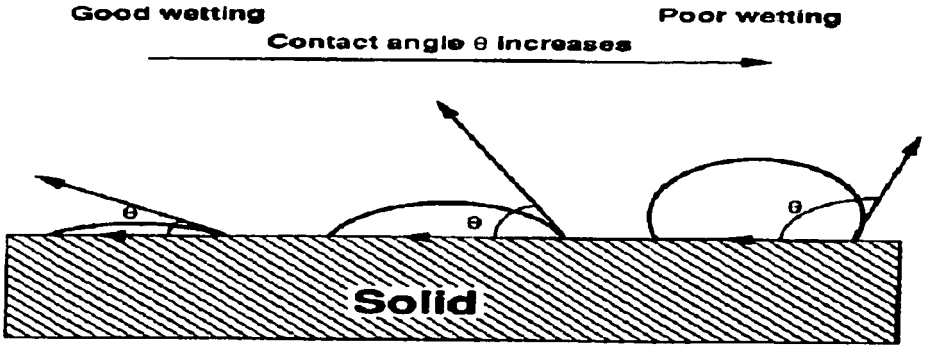

Figure 2.13 Small and large contact angles represent good and poor wetting, respectively.

The contact angle, as shown in Fig. 2.14, is governed by the force balance at the three-phase boundary and is defined by Young's equation:

$$\cos\theta_i = (\Upsilon_{SV} - \Upsilon_{SL})/\Upsilon_{LV} \qquad (2.4)$$

Where: Υ is the surface tension (or surface free energy), θ_i is the intrinsic equilibrium contact angle, and the subscripts sv, sl, and lv refer to the solid-vapor, solid-liquid, and liquid-vapor interfaces respectively.

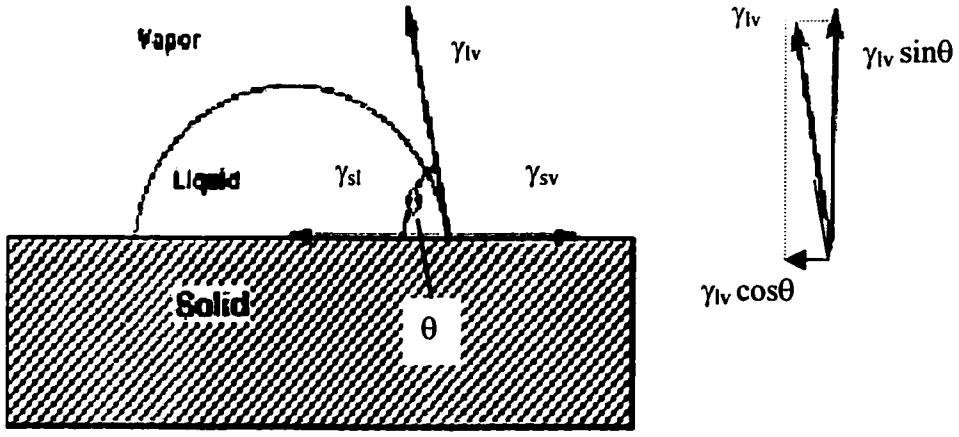

Figure 2.14 Equilibrium contact angle of a liquid drop on a solid surface.

The two types of contact angle are static and dynamic. Static contact angle are measured when the system is stationary, whereas dynamic contact angles are measured when the system is moving. Surface energy information can be derived from contact angle data. When water is used as the testing liquid, hydrophobicity and hydrophilicity of the polymer can be determined. The change in the contact angle as a function of aging time on a polymer surface treated by plasma or corona discharge is a very useful method for monitoring the migratory behavior of various functional groups at the surface. In a

typical static contact angle experiment, a drop of liquid is introduced on the surface of a sample by micro syringe. At equilibrium, the contact angle is measured by a telescope equipped by a goniometer eyepiece. Alternatively, measurements can be made on photographs or computerized video images (Chan, 1994).

2.2.2.5.2 Contact Angle Hysteresis

If the surface of a solid is smooth, chemically homogeneous, and rigid, the contact angle formed by the tangential plane to the liquid with the plane of the solid is the intrinsic equilibrium contact angle. When the liquid front is caused to advance over an ideal solid surface by the addition of a small amount of liquid, the same contact angle will be reestablished after the advance has stopped. When the liquid is caused to recede by subtraction of a small amount of liquid, the same contact angle will be reestablished after the retreat has stopped. On a practical surface, addition of liquid will not cause the liquid front to advance, but it will increase the height of the liquid drop and the contact angle. When enough liquid is added, a sudden advance will be observed. The angle at the onset of this sudden advance is the *advancing contact angle* θ_a, which is the maximum observed value. Subtraction of the liquid will not cause the liquid front to recede, but it will decrease the height of the liquid drop and the contact angle. When enough liquid is subtracted, a sudden retraction will occur. The angle at the onset of this sudden retraction is the *receding contact angle* θ_r, which is the minimum observed value. The difference between θ_a and θ_r is referred to as *contact angle hysteresis*.

2.2.2.5.3 Practical Significance of Contact Angle Measurement

Studies and measurements of contact angles of liquids on solids have great technological importance. This is especially true with water; every action of water on earth is controlled by its wetting behavior with the solid with which it comes into contact. For example, contact angle of water on our skin is about 90 degrees. If it was zero, water could have penetrated the pores of the skin and possibly been absorbed by blood. The structure of a bird's feather is constructed such that the contact angle of water on a typical feather is as high as 150 degrees. Machines such as Lathes are usually coated with a thin layer of grease or oil especially during transportation to prevent corrosion by water. This is achieved by the fact that grease or oil layer forms a highly non-wetting system with water. In the manufacture of printing inks, the contact angle formed by a drop of ink on paper determines the printing quality of ink. It has been practically observed that it must be ideally between 90 degrees and 110 degrees. If it is less than 90 degrees, the ink will spread on paper. If it's more than 110 degrees, breaks will occur while printing. The importance of contact angle measurement in the textile and fiber industry does not need to be overstressed. Cotton yarn is usually wetted by water, but synthetic fabrics have definite contact angle for water. Nylon, for example, gives a contact angle of about 40 degrees. Fabrics must be coated, therefore, with suitable wetting agents. Otherwise, it will be difficult to remove dirt and soil while washing the fabric with water. But it is

advantageous to use a non-wetting surface for a raincoat or umbrella cloth. Coating by a silicon polymer gives a highly non-wetting system. Waterproofing or water-repellency is an important industrial process, which depends on contact angle values (Boutin, 1999).

Most of the polymers like polyethylene, polypropylene, Teflon, etc. show high contact angle behavior with many liquids. A number of applications of polymers have taken advantage of this situation. An example is the Teflon coated frying pan. Contact angle measurement has shown that the contact angle is about 35 degrees for cooking oil on Teflon; thus oil must not stick to the surface making it easier for cleaning. The efficiency of insecticide sprays also depends on their wetting behavior on the surface of insects. Usually in most insecticides, an organic liquid having a low surface tension is used as spray so that it spreads completely. Contact angle is therefore an essential parameter to be considered in any pesticide or insecticide spray formulation.

An important technological application that emerged out of contact angle studies is in the enhanced oil recovery from sand beds. Laboratory experiments on displacing petroleum by water in glass capillaries have demonstrated that a considerable fraction of the oil remains attached to the wall when the central space of the capillary is already filled with water. In a sand column, the amount of oil remaining in the sand when water appeared at the downstream end of the column was greater, greater the contact angle. Flooding the oil wells with surfactants along with water or steam reduces the pressure drop across each oil-water meniscus, reduces the oil-water interfacial tension and changes the contact angle so that water displaces oil at the liquid-solid interface. The process is

called *'tertiary oil recovery'* and it is now possible by this method to recover more than 60% of oil from an oil reservoir. In heat exchangers and condensers used in chemical industries, maximum efficiency is achieved if the metal surface is coated by a non-wetting agent like calcium stearate or oleic acid. Liquids condensed on such coated walls form droplets because of high contact angle and fall down easily. This technique is called 'drop-wise' condensation. Contact angle measurement is important in controlling droplet surface area to increase or decrease evaporation and to optimize wetting of heat exchanger surfaces. Another area where contact angle plays an important role is in detergency, the process of cleaning clothes, etc., by a surface-active agent. If the soiled cloth is to get rid of dirt, grease, oil, etc., it is necessary that water must spread and penetrate the dirt particles. If spreading is to occur, the interfacial tension between solid-liquid and liquid vapor must be as small as possible. What the detergent does is exactly to lower these interfacial tensions by the process of adsorption. Contact angle measurements of lotions, oils, soaps and other toilet preparations on human skin and hair strands provide valuable information for their correct formulation and are now routine (Boutin, 1999).

2.2.2.6 Surface Profilometer

In practice, surfaces are generally not smooth, but exhibit small-scale peaks and valleys. Surface texture or roughness is commonly measured by a profilometer. It is suitable for measuring macro surface structures (in μm range); Whereas AFM has a very high spatial resolution and is more suitable for determining microstructures (in nm range).

A profilometer comprises a mechanical sensing system. In use, a sharply pointed stylus rests lightly on the surface, carefully traversing it. The up and down movements of the stylus are magnified and recorded, creating a surface profile. The main parameter for profile evaluation is average roughness, R_a defined as:

$$Ra = \frac{1}{L}\int_0^L |y| dx \tag{2.5}$$

Where L is the sampling length and y is height of the roughness trace at a given point from the centerline (See Fig 2.15).

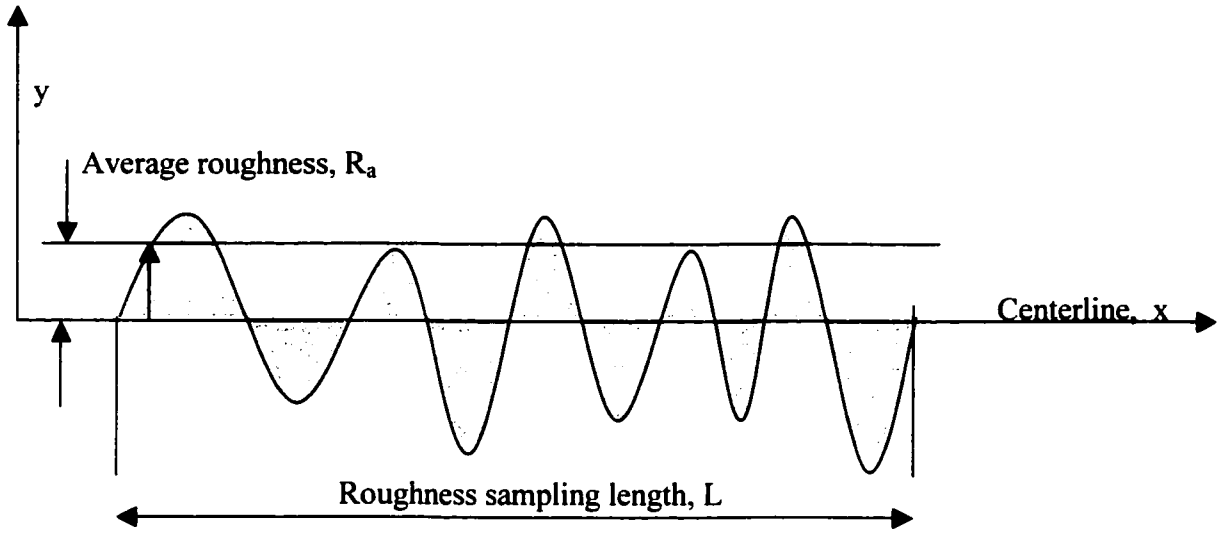

Figure 2.15 Schematic diagram showing the mean roughness, R_a

2.2.2.7 Attenuated Total Internal-Reflection Spectroscopy (ATIR)

Attenuated total internal-reflection spectroscopy has been a useful technique for the characterization of polymer surfaces. It is based on the idea that when a beam of infrared radiation passes from a denser to a less dense medium, reflection occurs. The sample is simply pressed against an internal-reflection element, as shown in Fig. 2.16. The radiation is internally reflected from the interface between the sample and the internal reflection element. It also penetrates a certain distance beyond the reflecting interface. Generally, this technique is not very surface- sensitive because of the large penetration depth; nevertheless, it is still a very useful technique when surface sensitivity is not necessary (Chan, 1994).

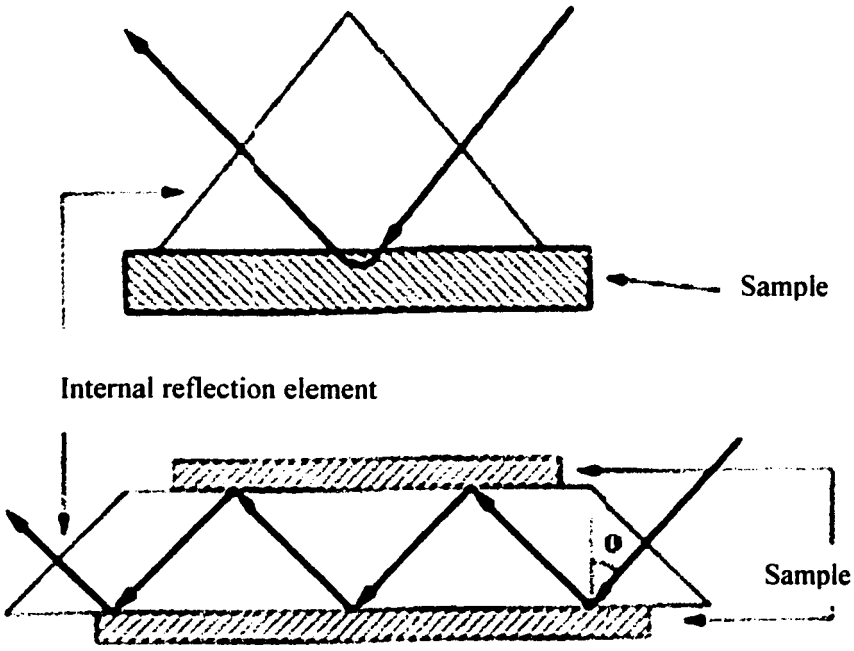

Figure 2.16 Schematic representation of the path of a ray of light in a single and multi reflection element (Chan, 1994).

2.2.2.8 Static Secondary Ion Mass Spectrometry (SSIMS)

SSIMS has proved to be a valuable method for determining composition and structure of polymer surfaces. It complements XPS because SSIMS can differentiate among polymers that have similar XPS. In an SSIMS experiment, the surface is bombarded with a primary ion beam of low current density to minimize damage. The sputtered material consists largely (> 99%) of secondary neutral species, with a small fraction (< 1%) of secondary negative and positive ions. The mass of the ions is measured by a mass analyzer. A detailed analysis of negative and positive ion spectra can provide structural and chemical information about the polymer surface. A key problem with SSIMS is its inability to perform quantitative analysis. In addition, lack of understanding of the relationship between the structure of a polymer and its ionic fragments obtained in an SSIMS experiment renders the analysis of an unknown sample very difficult.

Chapter 3

THEORY

3.1 Background

It is known that a drop of water deposited onto the surface of a solid object will form a sessile drop. In addition, we often see that many liquids can climb up to a certain height in a capillary tube and form a meniscus at the top. In these phenomena, the angle formed between the liquid-vapor interface and the liquid-solid at the solid-liquid-vapor three-phase contact line is conventionally defined as *contact angle*. In this study, the contact angle and its correlation with microscopic surface morphology will be the center of attention. It should also be noted that all the theories mentioned in this work are based on equilibrium contact angle.

Unfortunately, contact angle phenomena are complex. This complexity is most easily appreciated by invoking the classical theory of capillarity (Gibbs, 1961). Minimizing the overall free energy of a system consisting of a liquid in contact with a solid yields the following two well-known equations:

Laplace equation of capillarity (De Laplace, 1808).

$$\gamma_{lv}\left[\frac{1}{R_1}+\frac{1}{R_2}\right]=\Delta\rho gz+c=\Delta P \tag{3.1}$$

where R_1 and R_2 are the principal radii of curvature at a point of the liquid surface, $\Delta\rho$ is the density difference between the liquid and vapor phases, g is the acceleration due to gravity, z is the ordinate of a point of the liquid surface at which the principal radii of curvature are R_1 and R_2, c is a constant, and ΔP is the capillary pressure.

Young's equation is represented by (Young, 1855),

$$\text{COS}\ \theta_i = (\Upsilon_{SV} - \Upsilon_{SL})/\Upsilon_{LV} \qquad (3.2)$$

Where Υ is the surface tension (or surface free energy), θ_i is the intrinsic equilibrium contact angle, and the subscripts sv, sl, and lv refer to the solid-vapor, solid-liquid, and liquid-vapor interfaces respectively (Good, 1993).

The derivation of Laplace and Young relations assumes that the solid surface in contact with the liquid is smooth, homogeneous, isotropic and non-deformable (Li and Neumann, 1996).

3.2 Effect of *macroscopic* surface morphology on the wetting phenomenon.

The equilibrium intrinsic contact angle given by Young's equation, θ_i is a unique function of the interfacial tensions. In the vast majority of cases, however, experimentally observed contact angles are not uniquely determined by the surface tensions of the solids and liquids; normally, there exists a range of contact angles, quite often as large as 50°. These angles are categorized as apparent contact angle (Li and Neumann, 1996).

Normally, the largest and the smallest of these angles are recorded and termed as the *advancing contact angle,* θ_a, and the *receding contact angle,* θ_r, respectively. The equilibrium contact angle can also be measured. As will be shown in the results section the values of equilibrium contact angle for hollow fibers are only a few degrees less than advancing contact angles. The difference between the advancing and the receding contact angles is also called *contact angle hysteresis.* It is known that two factors give rise to contact angle hysteresis, surface heterogeneity and surface roughness.

3.2.1 Surface Heterogeneity

Polymer surfaces are largely heterogeneous. For example, the surface of polymer blends may comprise several components, or plasma-treated polymer surfaces may contain both high and low-surface-energy regions (Morra et al., 1990). Surface heterogeneity can cause contact angle hysteresis.

A surface may consist of low and high surface energy regions with intrinsic contact angles θ_1 and θ_2, respectively. As the liquid drop periphery advances over such a surface, the liquid front tends to stop at the region boundaries where energy barrier exist. The advancing angles are associated with the low-surface-energy regions, whereas the receding angles are associated with the high-surface-energy regions (Adamson, 1982).

Cassie and Baxter (1944) derived the Cassie equilibrium contact angle θ_c for a heterogeneous surfaces:

$$\Upsilon_{LV} \cos \theta_c = f_1 (\Upsilon_{S1V} - \Upsilon_{S1L}) + f_2 (\Upsilon_{S2V} - \Upsilon_{S2L}) \qquad (3.3)$$

or

$$\cos\theta_c = f_1 \cos\theta_1 + f_2 \cos\theta_2 \quad (3.4)$$

Where θ_c is known as Cassie contact angle for heterogeneous surfaces, and f_1 and f_2 represent the fractional surface areas of low-surface-energy and high-surface-energy regions, such that

$$f_1 + f_2 = 1 \quad (3.5)$$

3.2.2 Surface Roughness

The effect of macroscopic surface roughness on contact angle was modeled by several authors about 50 years ago. It was only in 1963 that Wenzel recognized that Young's equation might not be a universal equilibrium condition for the physical interaction between a solid and a liquid. The basic idea was to account for through R, the ratio of the actual to the projected area.

Thus $\Delta A_{sl} = R\,\Delta A_{sl\ apparent}$ and similarly for ΔA_{sv} such that the Young's equation becomes

$$\cos\theta_{ap} = R\,(\Upsilon_{SV} - \Upsilon_{SL})/\Upsilon_{LV} \quad (3.6)$$

Where θ_{ap} is apparent contact angle and R is the surface roughness and always larger than unity (Miller and Neogi, 1985).

This leads to the so-called Wenzel equation correlating the apparent and the intrinsic (θ_i) contact angles:

$$\cos\theta_{ap} = R\cos\theta_i \quad (3.7)$$

If the surface is very rough, a liquid with large contact angle (>90°) may not completely wet the surface. Such an incompletely wetted surface is referred to as a composite surface. Cassie and Baxter (1944) have derived an equation for composite surfaces:

$$\text{COS}\,\theta_{ap} = R f_w \text{COS}\,\theta_i - f_{nw} \qquad (3.8)$$

Where R is surface roughness, θ_i is the intrinsic contact angle at the solid liquid interface and f_w and f_{nw} are area fractions of solid surface wetted and non-wetted by the liquid, respectively. When $f_{nw} = 0$, Eq.3.8 becomes Wenzel's equation (Eq.3.7).

One of the difficulties with relations like Cassie or Wenzel equation is that they seemingly conflict with experimental observation: the latter equation predicts that the contact angle on a macroscopic rough surface should be smaller than the contact angle on a smooth surface if the surface is hydrophilic ($\theta_i < 90°$). If the contact angle on the smooth surface is larger than 90° (hydrophobic surface), then the contact angle on the rough surface should be larger (Li and Neumann,1996).

Experimentally, however, one finds that with increasing roughness, the advancing contact angle always increases and the receding contact angle decreases (Neumann et al. 1971). Another difficulty is that these equations are useful only for a uniformly macroscopic rough surface (See Fig. 3.1) and the parameter R does not take into account

the detailed nature of the surface (Jasper et al. 1955). Finally, θ_{ap} should not only depend on R but also on surface texture, for example surface nodule size and pore size. In addition to these difficulties, the explanations of the relation between surface parameters such as roughness, nodule size, and heterogeneity on the one hand, and the phenomena of contact angle on the other, made further investigations necessary.

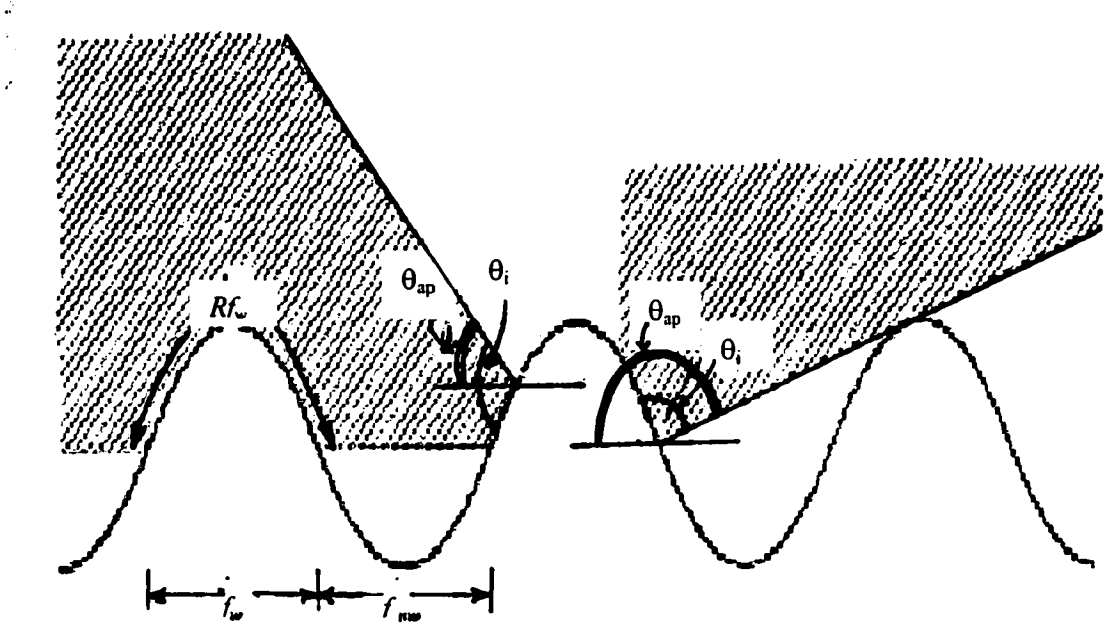

Figure 3.1 Drop edge on a macroscopic rough surface (Adamson, 1982).

3.3 Effect of *microscopic* surface morphology on the wetting phenomenon.

The effect of *microscopic* surface nodule size and roughness on the wettability of hollow fiber membranes has been studied. The applicability of equations developed for macroscopic surface morphology (Young's and Cassie's equations) was also examined. In particular, our study on the effect of nodule size and roughness on the membrane surface is based on the concept that liquid cannot completely fill the troughs created between the nodules. This concept is illustrated in Fig. 3.2.

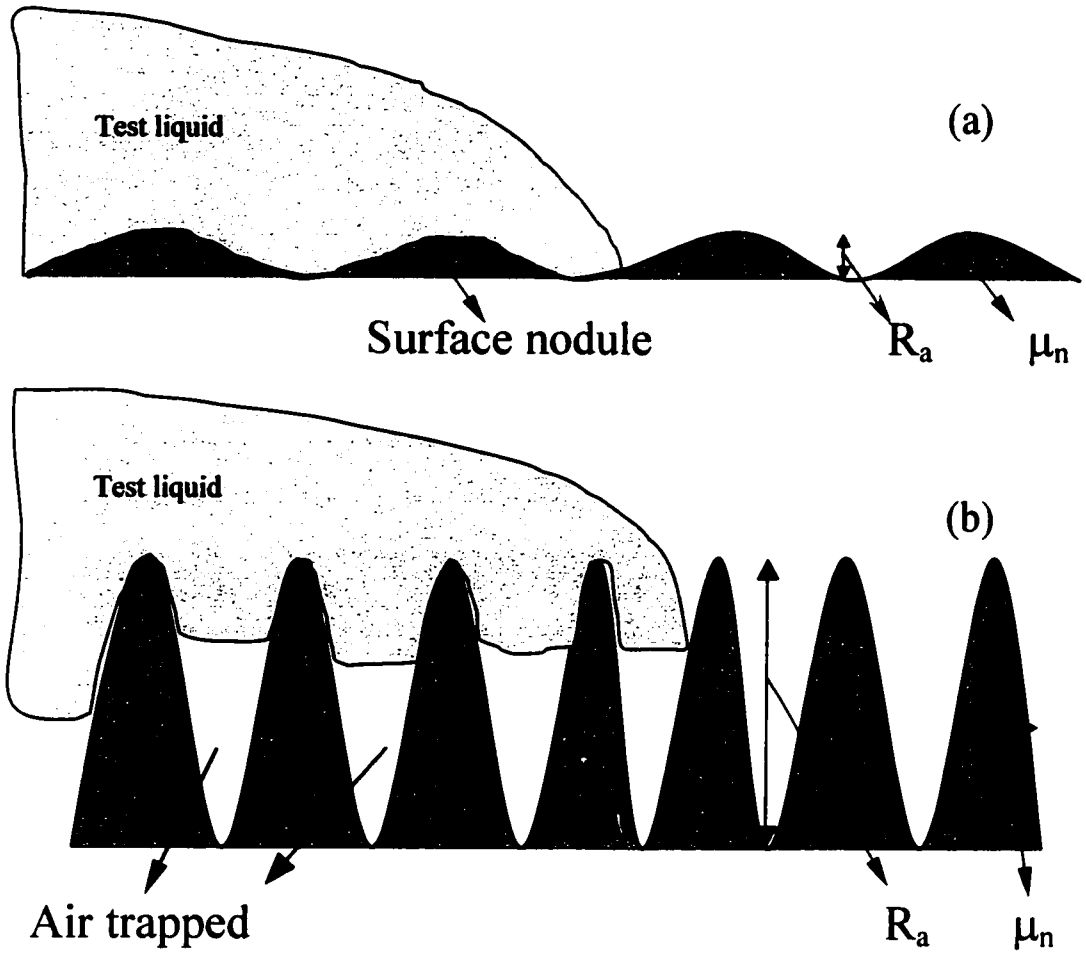

Figure 3.2 Microscopic cross-sectional drawings of (a) a relatively smooth surface, and (b) a relatively rough composite surface.

As shown in Fig. 3.2, the smaller the nodules and rougher the surface, the less the liquid penetrates into troughs due to the capillary phenomena. In this situation, the surface is considered as a composite surface in which the liquid does not come in complete contact with the solid surface due to the air trapped in the troughs. Therefore, there is a decrease in area of contact between liquid and solid, causing the decrease in membrane surface hydrophilicity.

3.3.1 Direct Approach

In case of a composite surface, described in Fig. 3.2, the following modified form of Υ_{SL} is proposed to consider the effect of trapped air in the troughs:

$$\Upsilon_{SLE} = \Upsilon_{SL}\, f_{SL} + \Upsilon_{LV}\, f_{LV} \tag{3.9}$$

where: Υ_{SLE} = effective surface tension for solid-liquid system.

f_{SL} = fraction of the surface where solid and liquid are in contact

f_{LV} = fraction of t he surface where liquid and vapor (air) are in contact.

Equation (3.9) implies that γ_{SLE} will become more than γ_{SL}, when $\gamma_{SL} < \gamma_{LV}$. When the test liquid is water γ_{LV} is known to be 72.8 $x10^{-3}$ J/m^2. Therefore, an attempt was made to approximately evaluate the range of γ_{SL}. It is known that the solid-vapor surface tension can be calculated from the relationship (Miyata et al., 1999),

$$\Upsilon_{SV} \approx 75x10^{-9}\, e_{coh}^{2/3} \tag{3.10}$$

where: the coefficient "$75x10^{-9}$" has a unit of $J^{1/3}$.

Furthermore from (Miyata et al., 1999),

$$e_{coh} = \delta_{sp}^{2} \tag{3.11}$$

and $\delta_{sp}=32.5x10^{3}\ J^{1/2}\ m^{-3/2}$ for polysulfone material (Sourirajan and Matsuura, 1985)

Therefore, γ_{SV} is calculated to be $77.7x10^{-3}\ J/m^2$.

The experimental θ values for polysulfone material depend on the surface morphology but they are above 60° and below 85°.Then, γ_{SL} can be calculated by equation 3.2 for the above range of θ. It is from $41.3\ x10^{-3}\ J/m^2$, corresponding to $\theta = 60^{\circ}$, to $71.3x10^{-3}\ J/m^2$, corresponding to $\theta = 85^{\circ}$. This confirms that γ_{SL} ($41.3\text{-}71.3x10^{-3}\ J/m^2$) < γ_{LV} ($72.8x10^{-3}\ J/m^2$). Therefore, γ_{SLE} should be greater than γ_{SL}. Using γ_{SLE} instead of γ_{SL} in Eq. 3.2 to calculate apparent contact angle, θ_{ap},

$$\text{COS}\ \theta_{ap} = (\gamma_{SV} - \gamma_{SLE})/\gamma_{LV} \tag{3.12}$$

θ_{ap} becomes greater than θ_i. This means that the contact angle of the composite surfaces becomes greater than the intrinsic contact angle of the material. Moreover, comparing Fig.3.2 (a) and (b), it is evident that the chance of air being trapped in troughs increases as the ratio R_a/μ_n increases, that further leads to an increase in f_{LV}, γ_{SLE}, and θ_{ap}. Therefore, it is predicted theoretically that the measured contact angle, θ_{ap}, will increase with an increase in R_a/μ_n. This will be confirmed later in the experimental results section.

3.3.2 Indirect Approach

To quantify the effect of surface morphology on contact angle, the following empirical model was proposed based on the theory developed in section 3.3.1.

$$\cos\theta_{ap} = f_{sl} - R_a f_{lv} \cos\theta_i \qquad (3.13)$$

Where: θ_{ap} = apparent contact angle at the solid liquid interface

θ_i = intrinsic contact angle at the solid liquid interface

f_{sl}= fraction of the solid surface that is in contact with the liquid or $\mu_n/(\mu_n+\mu_p)$

f_{lv}= fraction of the solid surface that is not in contact with the liquid or $\mu_p/(\mu_n+\mu_p)$

R_a= the ratio of the actual to the projected surface area that can be replaced by the numerical value of mean surface roughness.

Eq. 3.13 allows an increase of θ_{ap} with an increase in R_a when $\theta_i < 90°$.

The capillary rise equation, which defines the height of liquid that rises into a tube due to capillary action, can, on the other hand, be applied for the case of dialysis hollow fiber membranes:

$$\cos\theta_e = (r.\Delta\rho.g.h)/2\Upsilon_{LV} \qquad (3.14)$$

where: h= height of liquid rise in the hollow fibers, m

Υ_{LV} = surface tension of the liquid interface, J/m

θ_e= equilibrium contact angle of the liquid on the hollow fiber interior, degree

r = average internal radius of hollow fibers, m

$\Delta\rho$= density difference between the liquid and vapor phases, kg/m^3

g = acceleration due to gravity, $kg\ m/s^2$

As will be shown in the experimental section, the values obtained for θ_e from capillary rise experiments using Eq. 3.14 are in the range of 67.5 to 68°, while the values for experimental equilibrium contact angle (θ_{ap}) obtained from meniscus technique are in the range of 77 to 81°.

It will also be shown that θ_e values, obtained from Eq. 3.14, are independent from surface morphology (i.e. roughness and nodule size), while θ_{ap} values are affected by surface morphology. From these observations, it was hypothesized that θ_e values obtained from Eq. 3.14 correspond to the smooth and homogeneous surfaces. It is also known that when surface is smooth and homogeneous, the contact angle values are most likely those intrinsic to the surface material.

Therefore, θ_e values, obtained from Eq.3.14, may be considered as those intrinsic to the hollow fiber material.

Hence, θ_e in (3.14) = θ_i

Combining equations (3.13) and (3.14) yields

$$\text{COS}\ \theta_{ap} = f_{sl} - R_a f_{lv}\,(r.\Delta\rho.g.h)/2\Upsilon_{LV} \qquad (3.15)$$

This equation is valid when the intrinsic contact angle is large (but less than 90°) and the surface is microscopically rough (R_a>7nm and k>0.2). The validity of this equation will be examined later in the experimental results section.

3.3.3 Geometrical model for surface pores and nodules at the membrane surface.

In this section, a configuration is proposed to geometrically correlate the area covered by surface pores (or openings) with the one covered by nodules obtained from AFM surface images of the hollow fiber membranes. Assuming the closest packing of spherical nodules and an interstitial region (confined region) shown in Figure 3.3, the ratio of l_1 (radius of the largest circle that surrounds the confined region) to l (radius of the nodule) is calculated to be 0.577, while the ratio of l_2 (radius of a circle that has the same area as that of the confined region) to l is calculated to be 0.226.

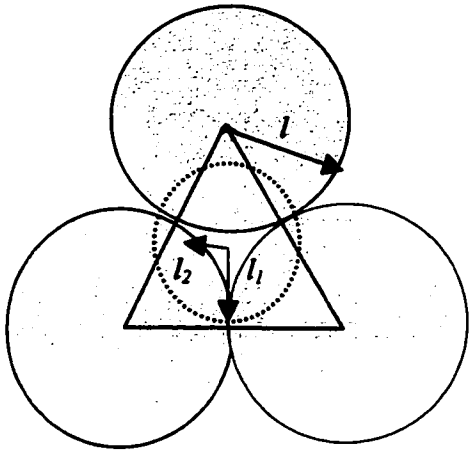

Figure 3.3 Closest packing of spherical nodules and the interstitial region.

The ratios of pore diameter to nodule diameter (μ_P/μ_n) experimentally obtained ranged from 0.268 to 0.557. It is also known that the pore sizes measured by AFM correspond to the pore entrances, which are of funnel shape and have maximum openings (Singh et al., 1998). By comparing the experimental values for μ_P/μ_n to those obtained from the above geometrical model, it may be concluded that the pores observed by AFM, most likely, correspond to the interstitial region surrounded by the nodules.

Chapter 4

EXPERIMENTAL

4.1 Materials

Melt-spun polysulfone and cellulose acetate hollow fiber membranes prepared under different spinning conditions were obtained from Baxter Healthcare Corporation, Miami Lakes, FL. As per procedure, some of the hollow fibers had been dried in an oven at 60-70 °C for predetermined periods after leaching out solvents and non-solvents. All polysulfone hollow fibers were manufactured by blending polysulfone with different molecular weight of polyethylene glycol (PEG). They were PEG-1000, 1500, and 2000.

4.1.1 Polysulfone Hollow Fibers

The basic structure of polysulfone is composed of aromatic entities, bis-phenol A and diphenylene sulfone (See Fig. 4.1). Each group contributes with specific properties to the polymer. The entire polymer molecule is proved to be thermal and oxidative resistant. In addition, a high degree of resonance of aromatic groups allows large amount of incident energy in the form of heat or ionizing radiation to be dissipated without chain scission or cross-linking taking place (Nguyen and Ericsson, 1999).

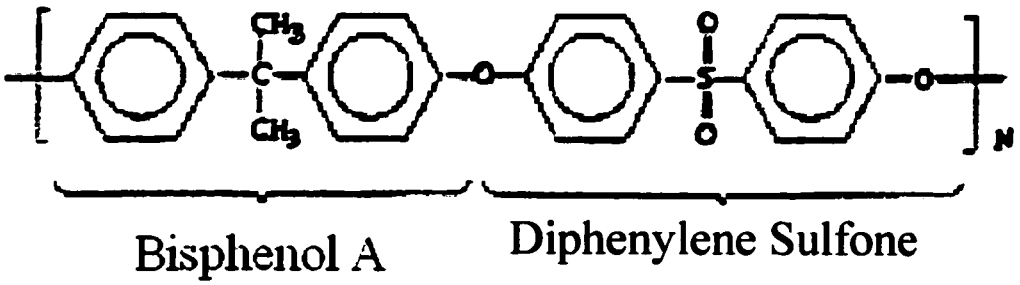

Figure 4.1 Chemical structure of Polysulfone polymer (Nguyen and Ericsson, 1999).

This membrane was manufactured from a synthetic high performance polymer via "*Thermally Induced Phase Separation*", *TIPS process.* Unlike solution spinning, the polysulfone melt was extruded through a spinneret at an elevated temperature and then was cooled down by air to create the membrane. The applied technology does not require the use of high molecular weight additives such as *polyvinylpyrrolidone (PVP)* in the formulation in order to control the membrane performance. In the TIPS process polysulfone polymer and plasticizers were mixed together at a high temperature to form a homogeneous melt, also called dope. The polymer blend or dope comprises a mixture of a polysulfone compound (i.e. polyarylsulfone or bisphenol A) with a concentration of at least 25 %, a solvent for PS compound (i.e. tetramethylene sulfone or "Sulfolane") with a concentration of at least 45 %, and optionally, a non-solvent (i.e. polyethylene glycol or glycerol) with a concentration of at least 5 % (Mcluch et al., 2001). The polymer blend was then extruded through a spinneret with nitrogen gas in the core to create a hollow fiber. Cooling down of the fiber was done gradually along the length and thereby controlling the membrane structure. This creates a membrane having a uniform micro porous wall structure with a very smooth inner surface. Only heat exchange was used in

this process; i.e. without chemicals or additives added in the fiber lumen for the creation of the microstructure as in solution spinning (Nguyen and Ericsson, 1999). Figure 4.2 illustrates the process for fabricating polysulfone hollow fiber membranes.

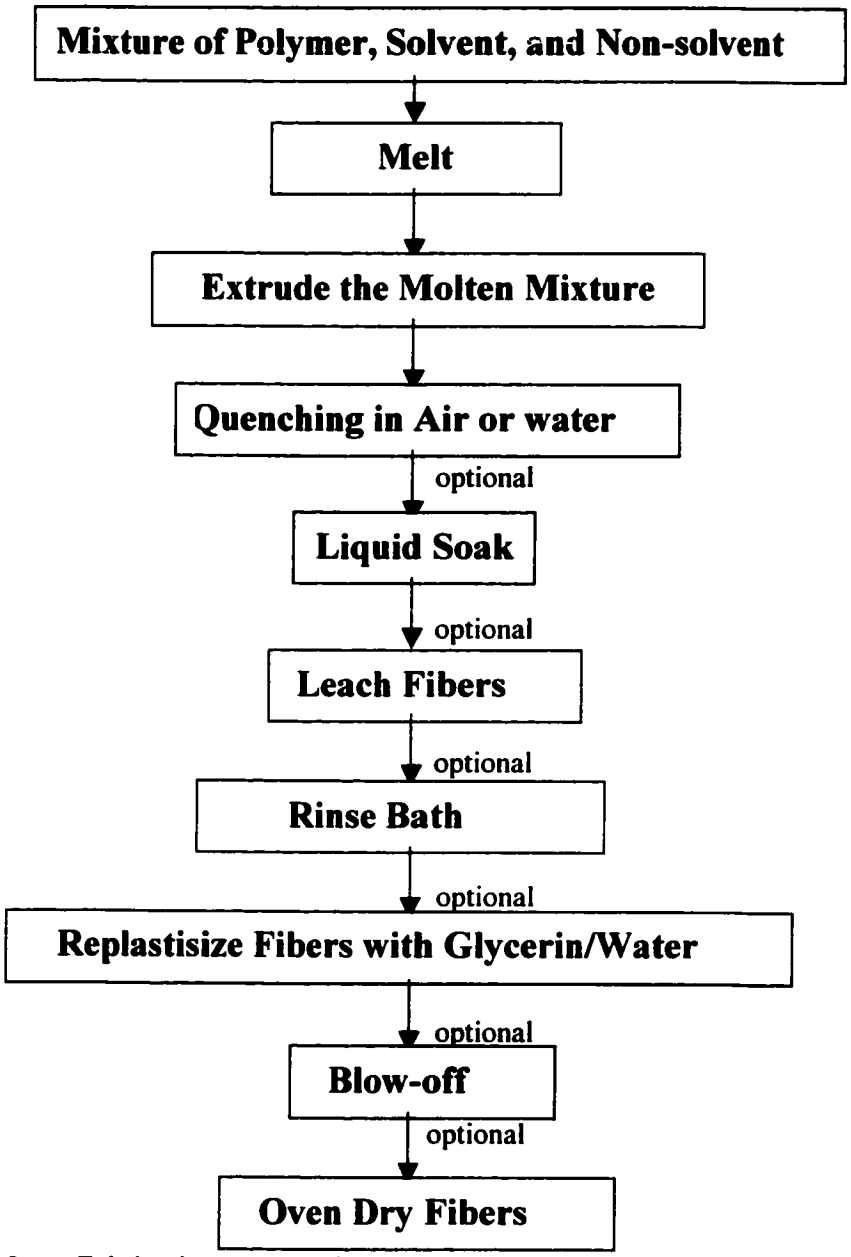

Figure 4.2 Fabrication process for melt-spun polysulfone hollow fiber membranes (Mcluch, 2001).

4.1.2 Cellulose Acetate Hollow Fibers

In melt-spinning process of cellulose acetate hollow fibers, only natural based polymer (cellulose diacetate), polyethylene glycol, and glycerol were used. Chemical structure of cellulose acetate is shown in Fig. 4.3.

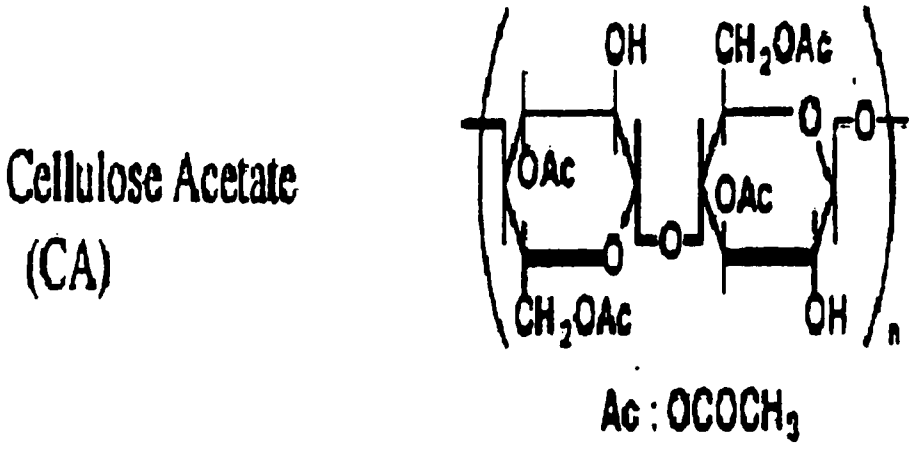

Figure 4.3 Chemical structure of cellulose acetate polymer.

The polymer blend comprises a mixture of cellulose acetate in weight percent ranges from 34-42%, glycerin 2-20%, and polyethylene glycol (MW of 150 to 600 Da), (Elsen & Silva, 1993). The melt-spinning process for manufacturing of cellulose acetate hollow fiber membranes is almost the same as the one for polysulfone. This process is schematically presented in Fig. 4.4.

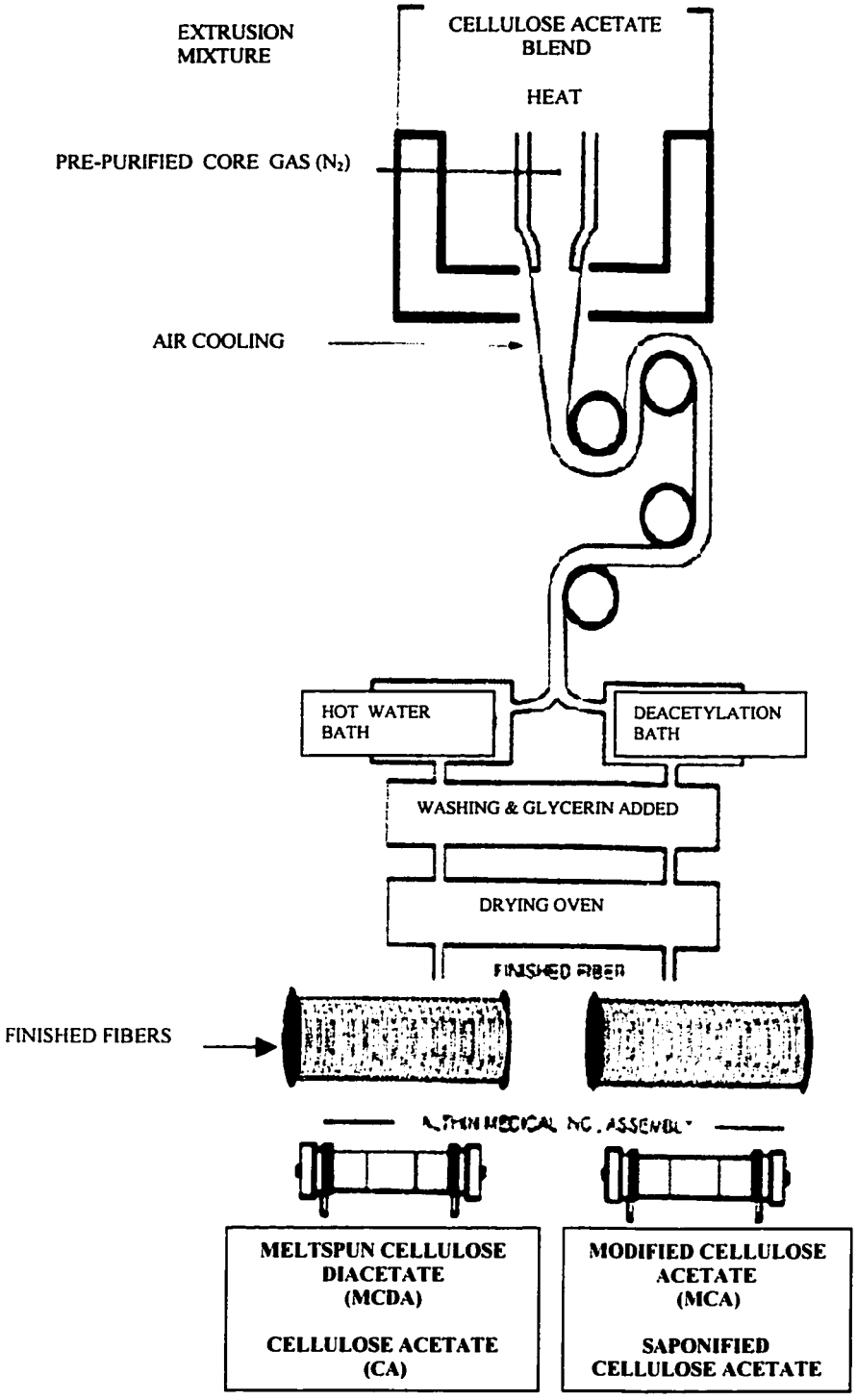

Figure 4.4 Flowchart of cellulose acetate hollow fiber melt-spinning process (Elsen & Silva, 1993).

4.2 Methods

4.2.1 Contact Angle Measurements (CAM)

4.2.1.1 Measurement Techniques Used for Hollow Fiber Membranes

4.2.1.1.1 Meniscus Technique

Contact angle measurement was carried out by goniometrically determining the angle from observations of the three-phase meniscus system at the external (See Fig. 4.5) and internal surfaces of hollow fibers (See Fig. 4.6). For this purpose, a contact angle goniometer (Rame Hart, Model 100) was used. This gonimeter was modified for hollow fiber application in our laboratory.

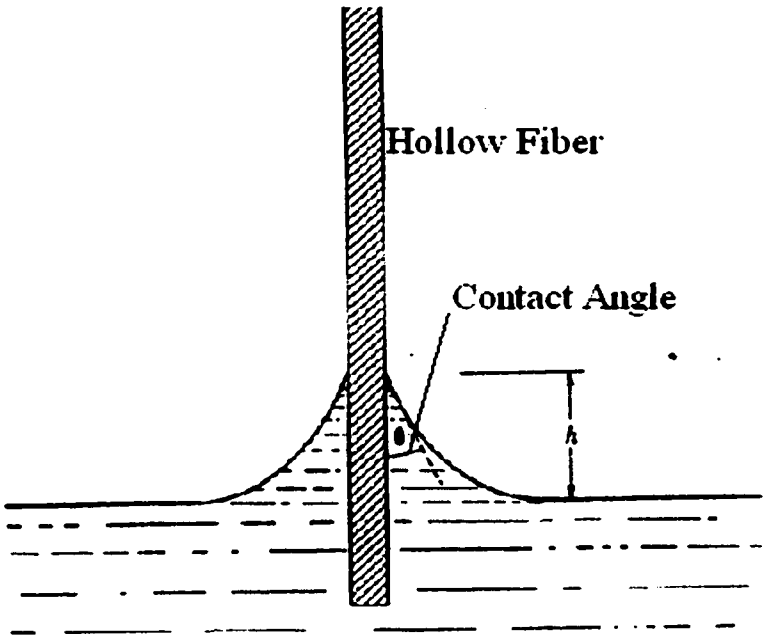

Figure 4.5 Three-phase meniscus system at the external surface of hollow fibers.

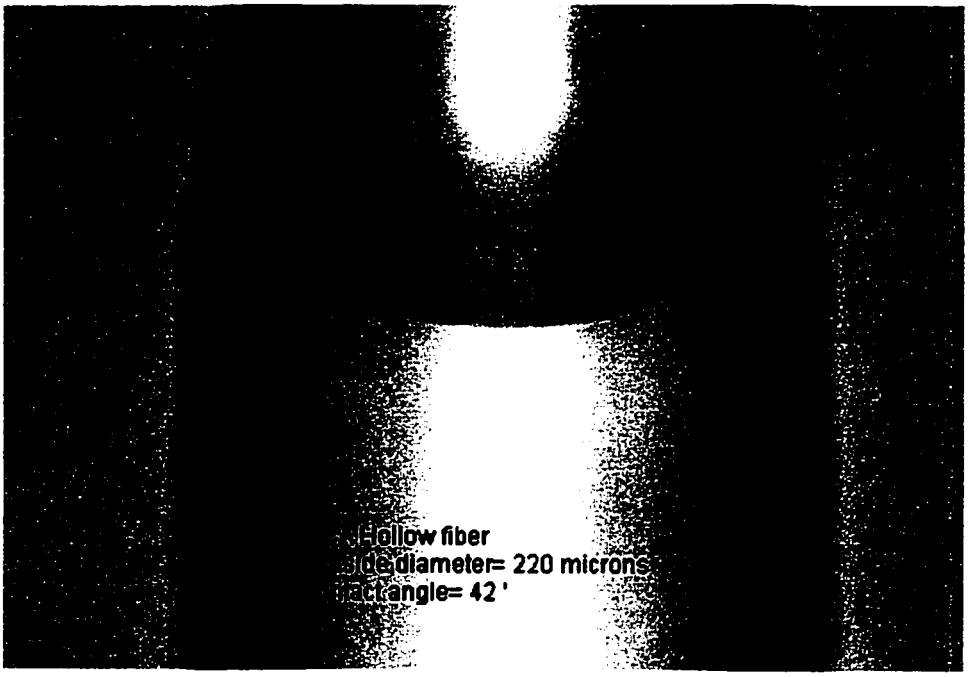

(a)

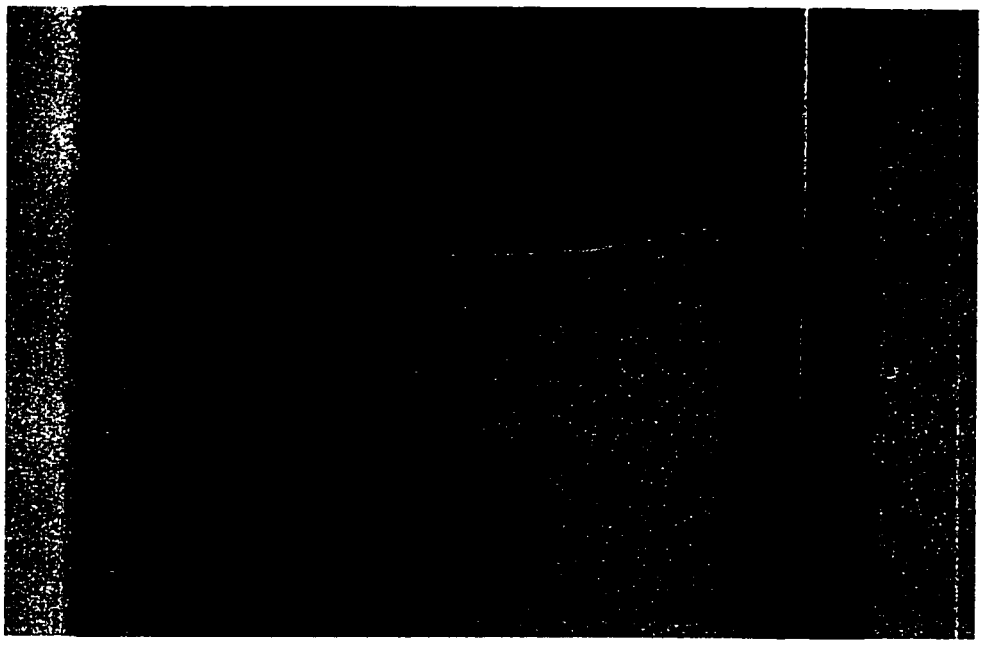

(b)

Figure 4.6 Internal meniscus of (a) modified cellulose acetate (MCA) and (b) polysulfone (PS) dialysis hollow fiber membranes.

4.2.1.1.1.1 Sample Preparation

The first step was to remove glycerin from the surface of the hollow fiber membranes. Glycerin was used to preserve the membrane pore structure prior to drying of the membrane. To remove the glycerin, the hollow fibers were placed in a perforated vessel that was dipped into a beaker containing distilled water. A laboratory stirrer and a magnetic stir bar were used to circulate water in the vessel for half an hour. After glycerin removal, fibers were dried in air for one hour. Then, they were cut into 20 cm long fibers. Each piece of hollow fiber was gently mounted on a rectangular metallic frame by double side tape at the top and bottom as shown in Fig. 4.7.

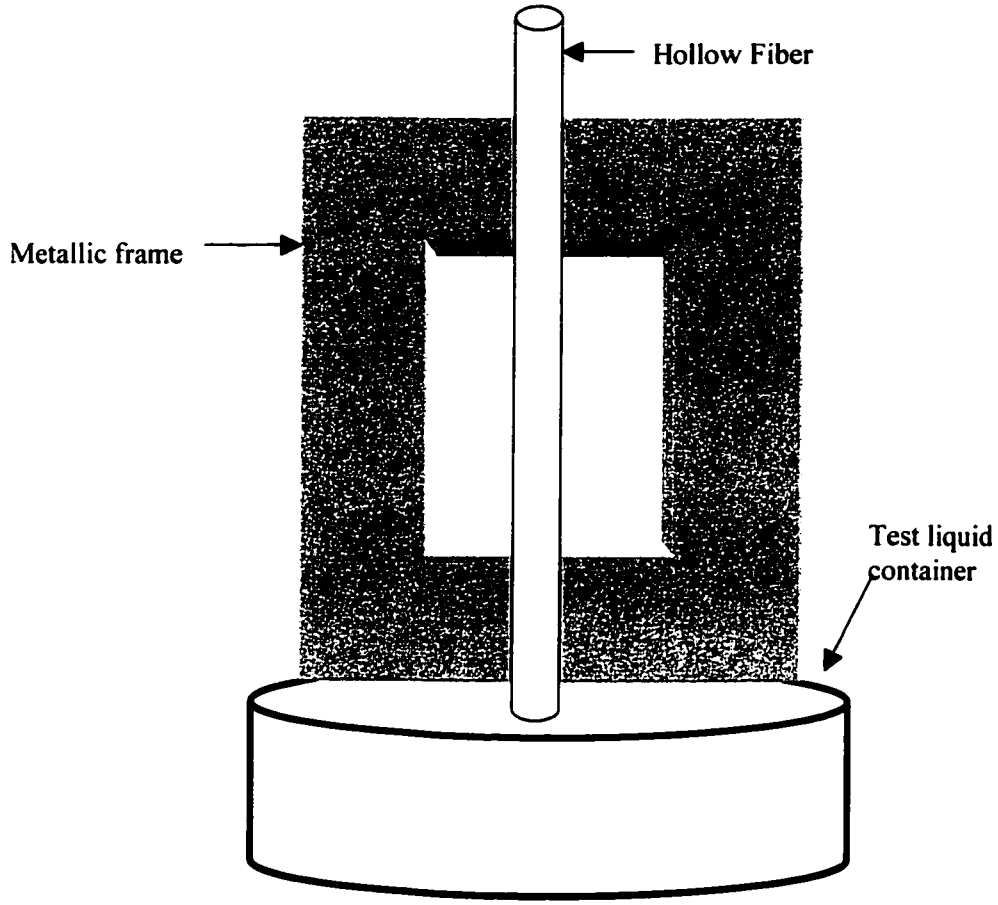

Figure 4.7 Sample holding technique used for direct measurement of contact angle.

4.2.1.1.1.2 Measurement Technique

The technique used in this study (Meniscus technique) is a novel approach toward the direct measurement of contact angle at the internal and external surfaces of dialysis hollow fiber membranes. The main advantage of this technique is its straight forwardness. While this technique provides useful information on both wettability and surface morphology of the membrane, the previously used techniques, i.e. Whilmy Plate and Capillary Rise techniques, give only some information on the membrane wettability without considering the surface morphology of the membrane.

In this technique, each hollow fiber was partially immersed in the test liquid (distilled water). Then, capillary rise and meniscus at the interior and exterior of the hollow fiber were monitored by a modified contact angle goniometer (See Fig. 4.8). Equilibrium contact angle was measured after the equilibrium condition was reached. Advancing and receding contact angles were also measured by gradually increasing and decreasing the level of the test liquid in the container in which hollow fiber was partially immersed. Each contact angle was the average of at least seven measurements. In all cases, contact angle data was reported in terms of equilibrium contact angle (θ_e) unless otherwise specified.

4.2.1.1.1.3 Experimental Apparatus

A Rame-Hart goniometer was modified to make the above-mentioned technique applicable to the surfaces of dialysis hollow fiber membranes. The first step was to increase the magnification ratio of the equipment by replacing the existing objective lens

with two lenses that were more powerful (*OLYMPUS* IC-10 and IC-20). IC-10 lens was used for the internal measurements while IC-20 was used for the external measurements.

The gonimeter's eyepiece was also replaced with an eyepiece (*OLYMPUS*, Model WHK 10x /20 L-H) equipped with a protractor (*OLYMPUS*, Model NE45 in 360 degrees, pattern diameter of 10 mm, and graticule size of 20.4 mm. In addition to the above modifications, two fiber optic illuminators were attached to the system to clearly monitor the meniscus. The contact angle gonimeter is shown in Fig. 4.8.

4.2.1.1.2 Capillary Rise Technique

Capillary rise inside hollow fibers was monitored by the same goniometer used in meniscus technique, then the internal diameter and the height of the liquid inside the hollow fibers were measured. The capillary rise equation (Eq. 3.14) was used to determine contact angle at the internal surface of hollow fibers. All the experimental procedures were similar to the meniscus technique except that in this technique, contact angle was determined indirectly from other measured parameters such as liquid height in the fibers, fiber diameter and test liquid surface tension while in meniscus technique it was directly measured from the observation of the meniscus system.

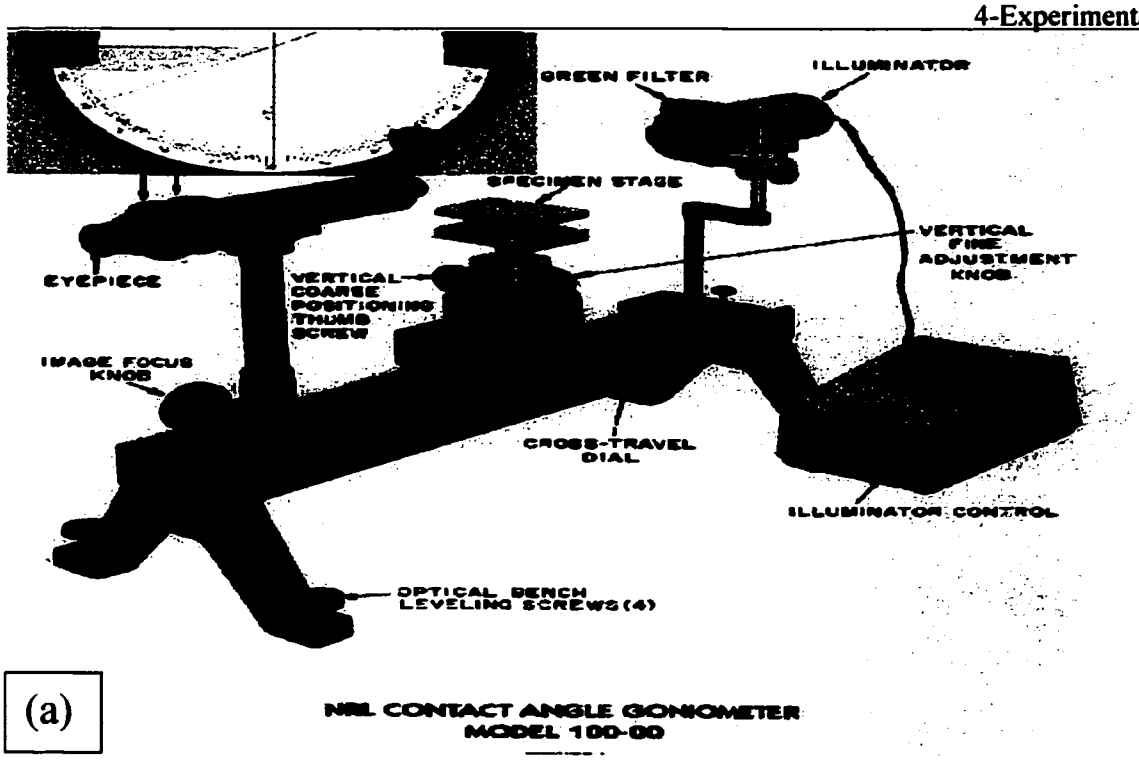

Figure 4.8 NRL contact angle apparatus (a) with a manual goniometer, and (b) with a goniometer and video camera (Rame-Hart, Model 100).

4.2.1.2 Contact angle measurement techniques used for flat sheet membranes.

4.2.1.2.1 Sessile Drop Technique

Advancing (θ_a), receding (θ_r), equilibrium (θ_e), and instantaneous contact angles at the membrane surfaces were measured by a horizontal beam comparator (SCHERR TUMICO, 22-2000 SERIES). Samples were prepared by cutting the membranes in small coupons (3cm x 5cm) and fixing them onto a flat glass plate. Distilled water drop was deposited onto the membrane surface by a microsyringe and θ_e was measured while the syringe tip was still in the drop. To measure θ_a and θ_r, the volume of the drop ($2x10^{-2}$ ml) was slowly increased and then decreased by adding water to and withdrawing water from it while again the syringe tip was in the drop. On the water addition, a contact angle reading just prior to the sudden movement of the three phase interface, was recorded as θ_a. Water was then withdrawn until the onset of another sudden movement of the three phase interface, to give the θ_r reading. To measure the instantaneous contact angle, the syringe tip was removed from the drop after the equilibrium was reached. Then, instantaneous contact angle was measured as a function of time. Each contact angle data was an average of seven measurements for each membrane.

4.2.1.2.2 Meniscus technique

Meniscus technique for flat sheet membranes was almost the same as the one for hollow fiber membranes. Samples were prepared in the same way prepared for sessile drop technique. Then, they were partially immersed in the test liquid and the angle was directly measured by monitoring the meniscus at the membrane surface.

4.2.2 Atomic Force Microscopy (AFM) Studies

4.2.2.1 AFM Apparatus

AFM studies were conducted on a tapping mode at the interior and exterior of the hollow fibers using a MultiMode™ scanning probe microscope (MM-SPM)(Nanoscope III equipped with 1553D scanner, Digital Instruments, CA). Major components of MultiMode™ SPM system are shown in Fig. 4.9.

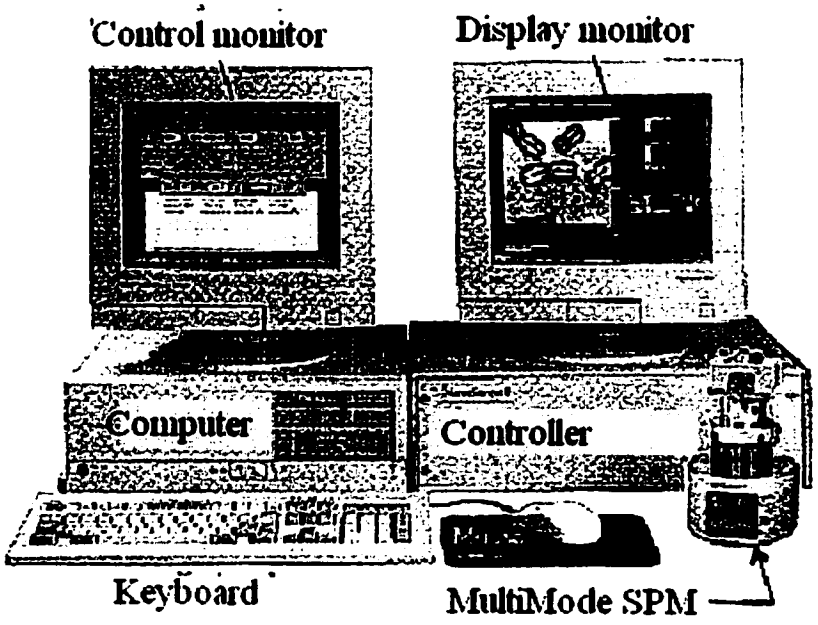

Figure 4.9 MultiMode™ SPM system hardware (Digital Instruments).

MultiMode™ SPM system consists of seven major components: SPM, controller, computer, keyboard, mouse, display monitor and control monitor. The heart of the system is the SPM itself, shown in Fig. 4.10

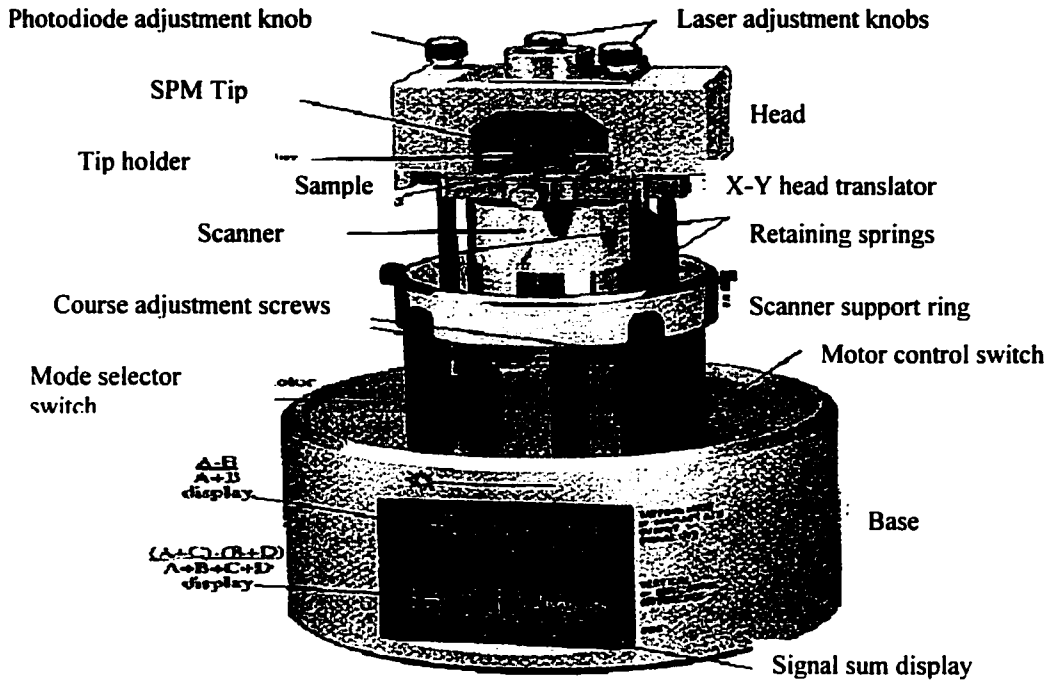

Figure 4.10 MultiMode SPM (Digital Instruments).

Most SPM work is done using cantilevered probes. These consist of a flexible cantilever extending from a rigid substrate, to which a tip has been attached (See Fig. 4.11). Most contact AFM is conducted with "silicon nitride" tips. On the other hand, in tapping mode, a crystal silicon probe is oscillated up and down at its resonant frequency while its amplitude and phase are monitored.

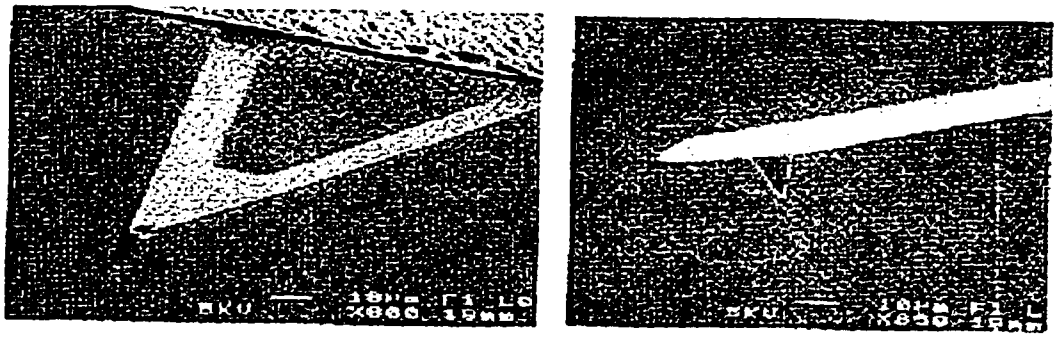

Figure 4.11 Two types of cantilevered probes: Silicon nitride (left), and crystal silicon (right) (Digital Instrument).

4.2.2.2 Sample Preparation

Each hollow fiber was cut in a small piece of 1 cm length, which was fixed to a round 1.5-cm metal disk ("puck") by a double side tape. Then, the hollow fiber was cut at an inclined angle as shown in Fig. 4.12.

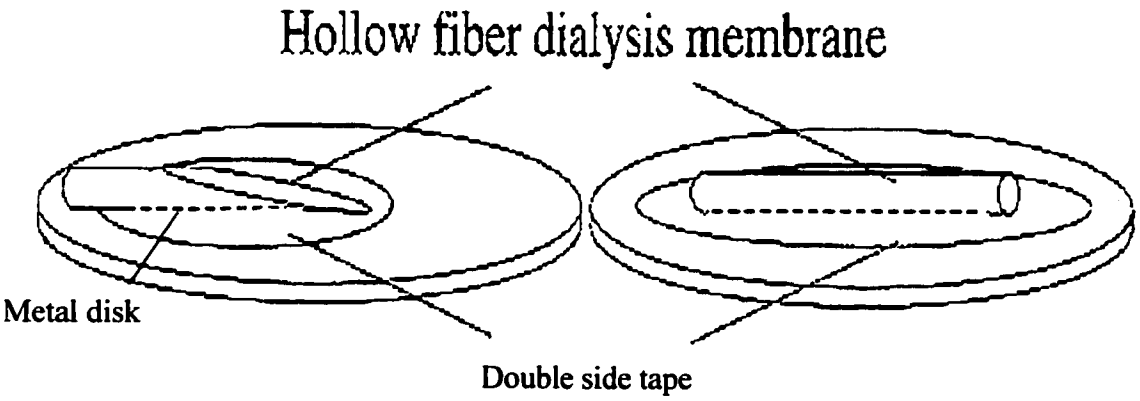

Figure 4.12 Cutting technique used for AFM and SEM studies of the internal surface of dialysis hollow fiber membranes.

By using this cutting technique, it became possible to have an access to the internal surface of dialysis hollow fiber membranes. The cut section of the hollow fiber was also inspected by a microscope to ensure that the membrane surface was not damaged.

4.2.2.3 Analysis Technique

After the sample was prepared, it was magnetically attached to the top of the scanner tube. As the scanner moves back and forth, the sample moves with it, allowing the probe to extract information from the sample surface much like a photograph needle plays a vinyl record. Images produced from scans were analyzed and/or modified using the microscope's functions.

During this study, roughness parameters were determined by the AFM software, while pore size and nodule size were determined by visual inspection of the line profile of different pores and nodules from various AFM images. Membrane surface morphology was also expressed in terms of mean surface roughness (R_a), mean surface nodule size (μ_n) and mean surface pore size (μ_n). The mean roughness is the mean value of the surface relative to the center plane, the plane for which the volume enclosed by the image above and below this plane are equal, and is calculated as

$$R_a = \frac{1}{L_x L_y} \int_0^{L_y} \int_0^{L_x} |f(x,y)| \, dx dy \qquad (4.1)$$

Where f (x, y) is the surface relative to the center plane and L_x and L_y are the dimensions of the surface (Singh et al., 1998).

Figure 4.13 represents the cross-sectional view of nodules and pores and the measurement of these parameters from AFM.

Figure 4.13 Cross-sectional view of nodules and pores and the measurement of these parameters from AFM.

Measurements of nodules and pores were taken from cross-sectional views of the data along the reference line. For a pair of cursors, the horizontal distance represents the diameter of a nodule or a pore. The mean diameter of pores or nodules is based on at least 50 measurements. The scan sizes of samples were in the range of 2-4 μm^2. Also, the same scan size was used for better analysis and comparison between different samples.

4.2.3 Scanning Electron Microscopy (SEM) Studies

Micrographs of the cross section, internal and external surfaces of dialysis MCA and PS hollow fibers were obtained using a scanning electron microscope (JEOL JSM 6400) at Carlton University. The scanning electron microscope was composed of X-Ray analyzer (Link eXL LZ4), Cryo-stage system (Oxford CT 1500), two backscatter detectors (Robinson & JEOL), and Tungsten and LaB6 filaments.

The same cutting technique used for AFM samples was used for SEM imaging to have an access to the internal surface of hollow fibers. Also, some preparative methods were required for SEM observations. For this purpose, a continuous conducting surface was necessary in SEM specimens in order to prevent charge build-up. As hollow fibers were not naturally conducting, a conductive surface was provided by attaching small swatches of hollow fibers to a sample stub by carbon tape and vacuum-coating them with up to 500 A° of gold-palladium alloy. Then, each sample was placed in a chamber equipped with a stage motorized in the X, Y and Z axes, which can be controlled manually using a joystick, or externally by a software. The sample was bombarded with an electron beam generated by a standard tungsten hairpin filament. SEM images were formed by collecting secondary electrons emitted from the bombarded specimen. SEM photographs were also taken at X-300, X-2000, X-5000, X-10000, X-15000, X-20000 magnifications. Figure 4.14 represents an SEM image obtained from the internal surface of a modified cellulose acetate (MCA) dialysis hollow fiber.

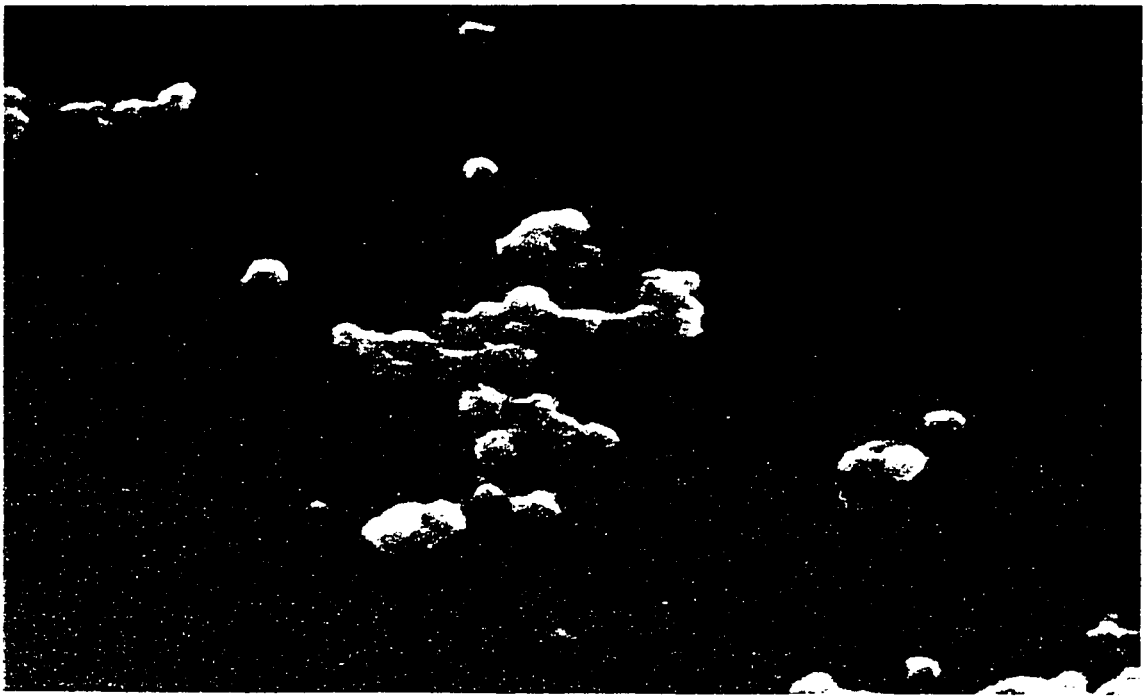

Figure 4.14 SEM image of the internal surface of a modified cellulose acetate (MCA) dialysis hollow fiber membrane.

Chapter 5

RESULTS AND DISCUSSION

This chapter is composed of six main sections. In the first four sections, the internal and external surfaces of dialysis hollow fiber membranes are characterized by AFM and CAM. The first and second sections represent the effect of hollow fibers drying time and PEG (polyethylene glycol) blending on surface properties of these membranes. In section three, the aim is to identify the effect of various parameters, i.e. material, surface morphology, and hollow fiber diameter, on surface energetic of the membranes. Section four deals with the morphology comparison between similar hollow fiber membranes made by various manufacturers. In the fifth section, two different techniques are used to measure the contact angle on flat sheet membranes. The goal is to compare the contact angle measured for flat sheet to those for hollow fiber membranes obtained by various techniques. In all cases, contact angle data was reported in terms of equilibrium contact angle (θ_e) unless otherwise specified. Finally, in the last section, scanning electron microscopy (SEM) is used to study the microstructure of hollow fiber membranes.

5.1 Effect of drying time on surface properties of dialysis hollow fiber membranes.

The internal and external surfaces of polysulfone hollow fibers blended with PEG- 1000 were studied by AFM and CAM. Figures 5.1 and 5.2 represent the AFM images obtained from the internal and external surfaces of PS hollow fibers. P-0 hollow fiber was dried for a short period of 5 minutes while P-1 and P-2 hollow fibers were dried for 1 and 2 hrs, respectively.

Membrane surface morphology has been expressed in terms of three parameters, mean roughness (R_a), mean nodule size (μ_n), and mean pore size (μ_p). Nodule sizes and pore sizes were measured at the inside and outside surface of hollow fibers by visual inspection of line profiles of different nodules and pores from various AFM images. The results were arranged in ascending order and assigned median ranks. To obtain a distribution function graph, these median ranks were plotted on the ordinate (Y axis) against nodule or pore sizes arranged in an increasing order on the abscissa (X axis)(Fig. 5.3 for nodule size). This plot yields a straight line on a log-normal probability paper if the nodule size or pore size measurements have a log-normal distribution. From this plot, values of mean nodule or pore sizes (μ_n or μ_p) and geometric standard deviations of nodule or pore sizes (σ_n or σ_p) can be calculated (Singh et al., 1998).

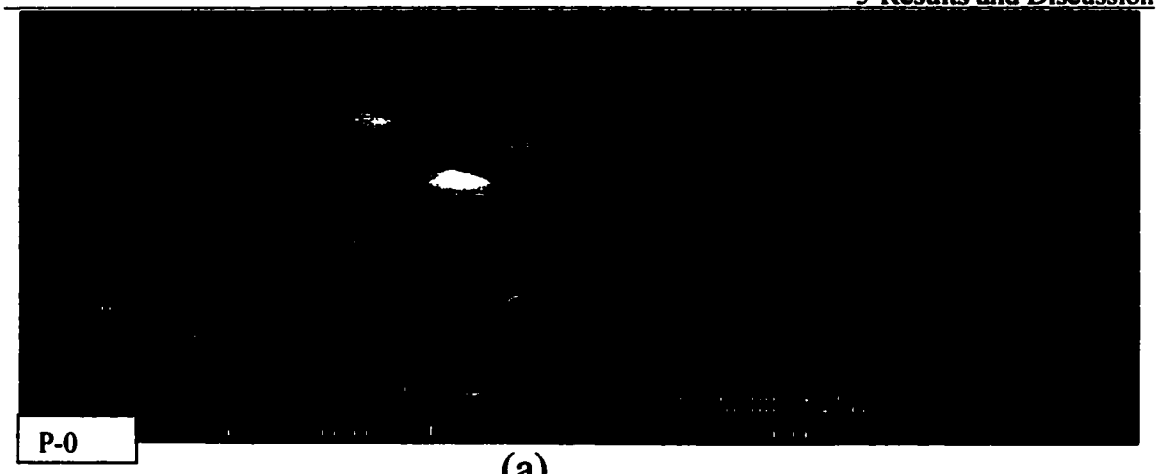

(a)

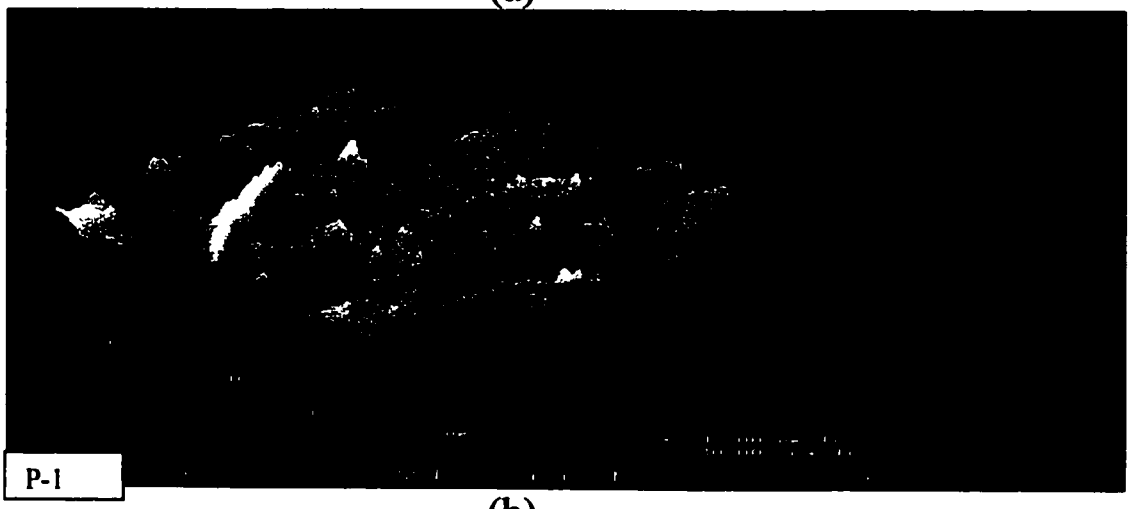

(b)

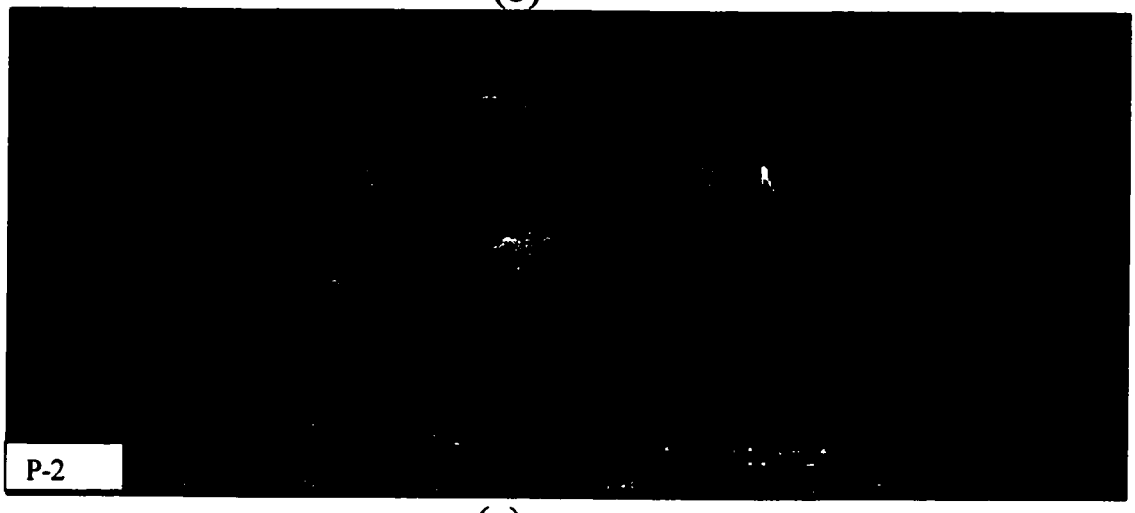

(c)

Figure 5.1 AFM images of the internal surfaces of (a) P-0 hollow fiber dried for 5 min, (b) P-1 hollow fiber dried for 1hr, and (c) P-2 hollow fiber dried for 2hrs.

(a)

(b)

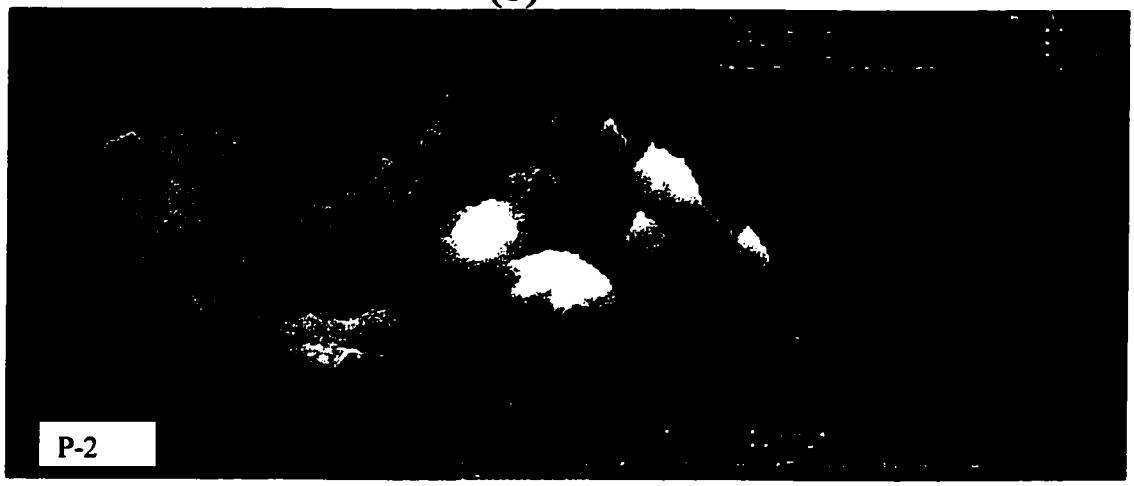

(c)

Figure 5.2 AFM images of the external surfaces of (a) P-0 hollow fiber dried for 5 min, (b) P-1 hollow fiber dried for 1hr, and (c) P-2 hollow fiber dried for 2hrs.

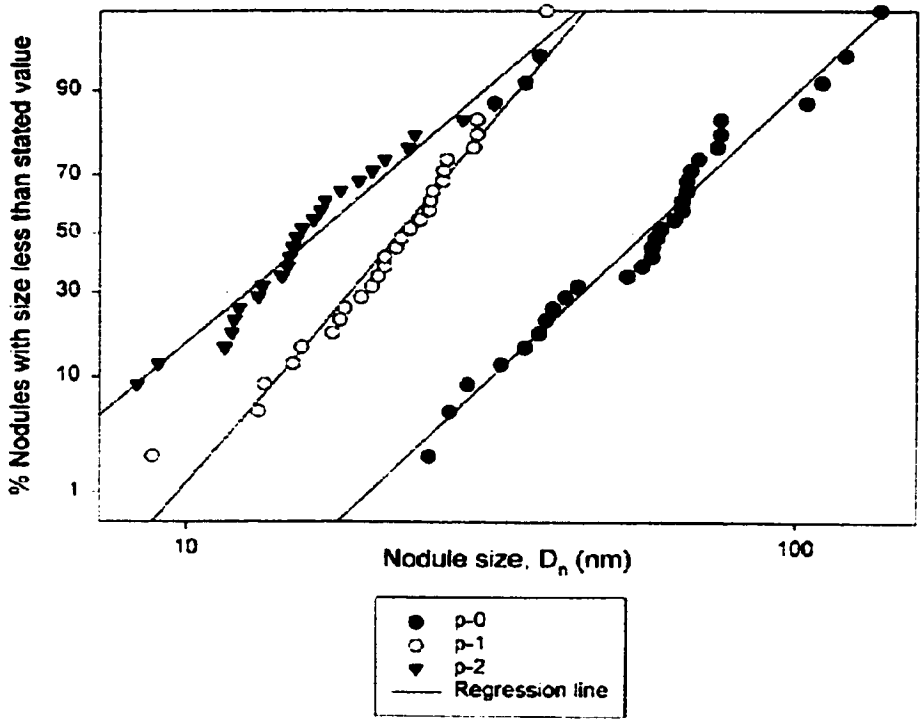

Figure 5.3 Log-normal nodule size distribution for the internal surfaces of P-0, P-1, and P-2 polysulfone hollow fibers subjected to drying for 5 mins, 1hr, and 2 hrs, respectively.

In addition to log-normal distribution chart, cumulative nodule size and pore size distribution (See Fig. 5.4) and probability density function curves (See Fig. 5.5) were generated based on the mean values and standard deviations for nodule sizes and pore sizes. According to Singh et al. (1998), pore sizes measured by AFM corresponded to the pore entrances which were of funnel shape and had maximum opening at the entrance while the pore sizes obtained from a solute separation corresponded to a minimal size of the pore constriction experienced by the solute while passing through the pore.

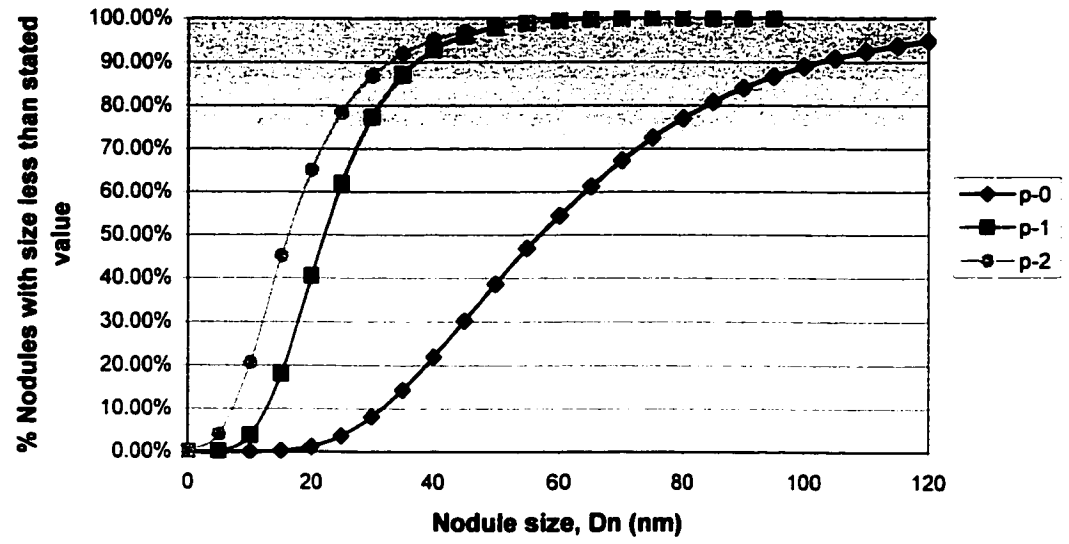

(a)

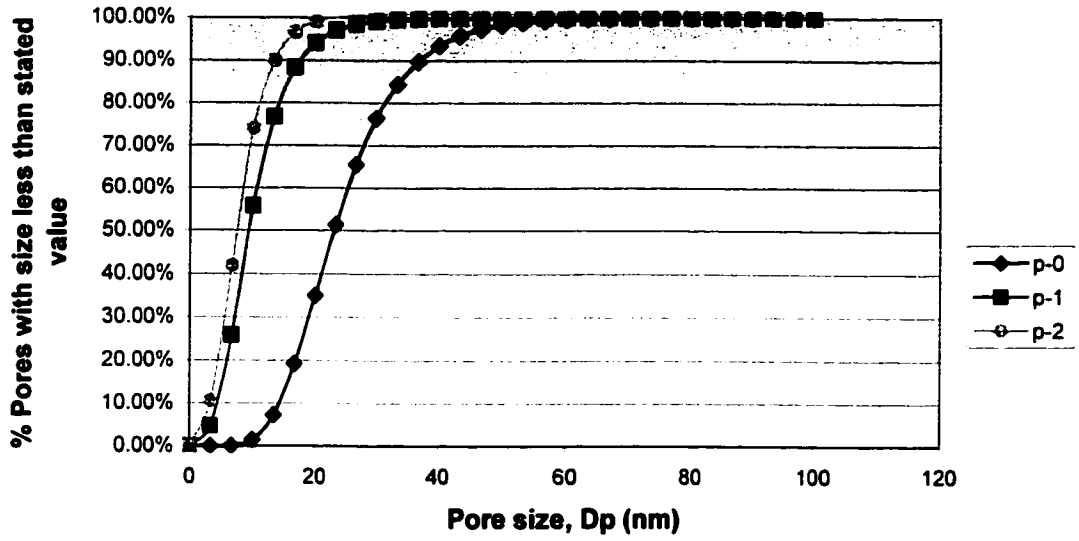

(b)

Figure 5.4 Cumulative size distributions of (a) the internal surface nodules and (b) the internal surface pores of P-0, P-1, and P-2 polysulfone hollow fiber membranes subjected to drying for 5 mins, 1hr, and 2hrs, respectively.

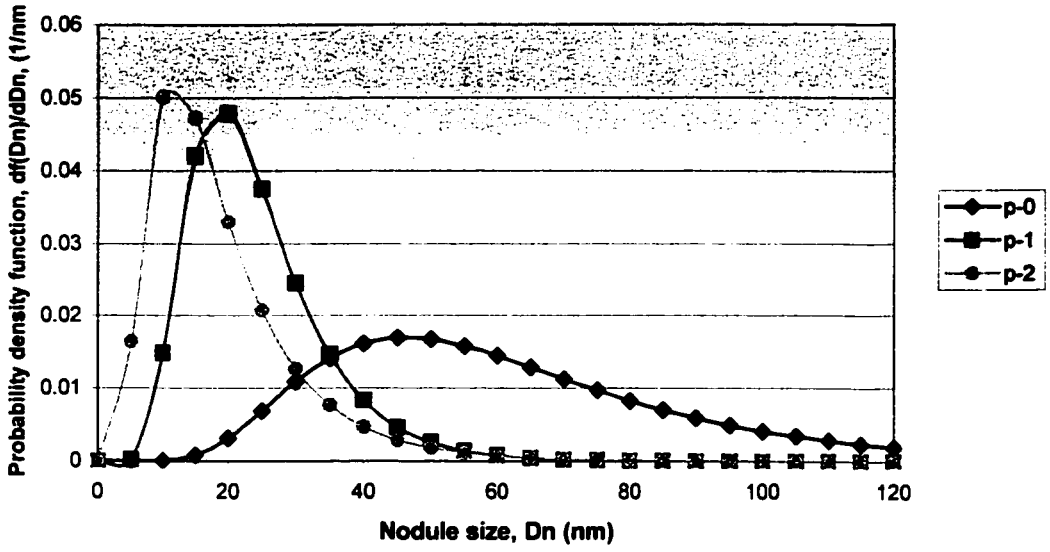

(a)

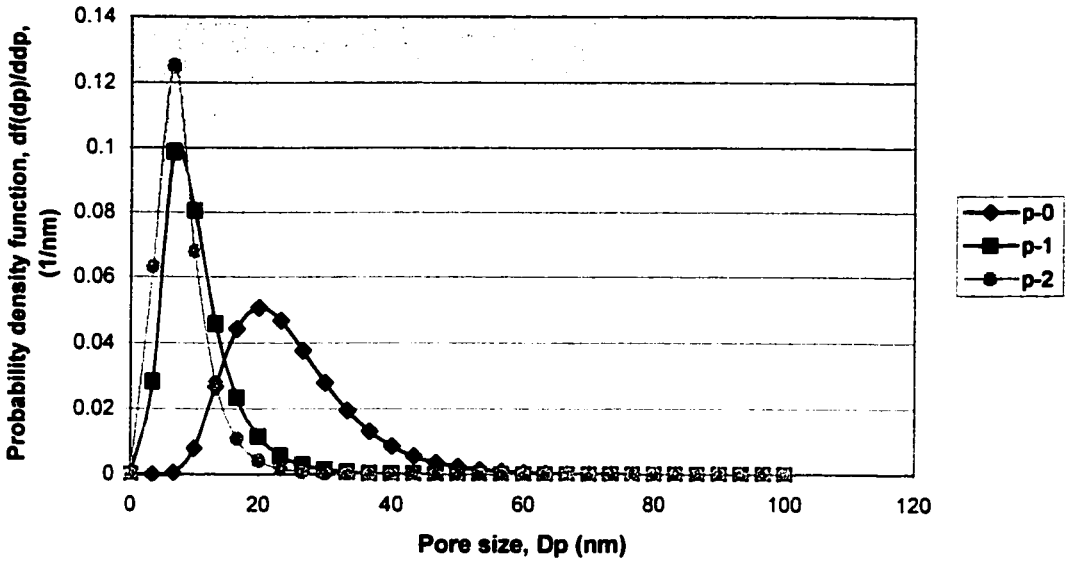

(b)

Figure 5.5 Probability density function curves generated for the internal (a) surface nodules and (b) surface pores of P-0, P-1, and P-2 polysulfone hollow fiber membranes subjected to drying for 5 mins, 1hr, and 2hrs, respectively.

Experimental results of the surface morphology and contact angle measurement have been summarized in Table 5.1 and Table 5.2 for the internal and external surfaces respectively.

Table 5.1 Experimental results of the surface morphology and contact angle measurement for the internal surfaces of P-0, P-1, and P-2 hollow fibers.

Hollow fiber name	Drying time (min)	R_a (nm)	μ_n (nm)	μ_p (nm)	θ_a (degree)	θ_e (degree)
P-0	5	4.1±0.2	57±1.6	23±1.4	79±0.5	-
P-1	60	7±0.5	22±1.5	9.2±1.6	83±0.6	81.1±0.3
P-2	120	7.9±0.6	16±1.75	7.3±1.6	83.1±0.5	81±0.4

*PEG in polymer solution, PEG-1000
*R_a values are based on the AFM scan size of 2000 nm.
*θ_a values are advancing contact angles obtained from meniscus technique.
*θ_e values are equilibrium contact angles obtained from meniscus technique.

Table 5.2 Experimental results of the surface morphology and contact angle measurement for the external surfaces of P-0, P-1, and P-2 hollow fibers.

Hollow fiber name	Drying time (min)	R_a (nm)	μ_n (nm)	μ_p (nm)	θ_a (degree)
P-0	5	5.6±0.3	70±1.6	39±1.6	71.8±1.5
P-1	60	-	25±1.5	6.7±1.5	80.4±2.7
P-2	120	7.8±0.5	17±1.75	6.2±1.7	79.0±3.2

*PEG in polymer solution, PEG-1000
*R_a values are based on the AFM scan size of 2000 nm.
*θ_a values are advancing contact angles obtained from meniscus technique.

Among the above "PS" hollow fibers, P-0 that was dried for shorter time had the largest mean nodule size (μ_n) and mean pore size (μ_p) while it had the lowest advancing contact angle. In general, it was found that contact angle and roughness increased while both nodule size and pore size decreased from P-0 to P-1 but they leveled off at P-1.

5.2 Effect of the molecular weight of PEG (polyethylene glycol) blended in the polymer solution on hollow fibers' surface properties.

The surface properties of PS hollow fibers manufactured from the polymer solutions blended with different molecular weights of PEGs were investigated by AFM and CAM. Some of the AFM and CAM experimental results are also summarized in Table 5.3.

The table shows that blending of higher molecular weight PEG decreases the advancing contact angle. Indeed, the decrease in advancing contact angle for PG-15 and PG-20 hollow fibers is due to the presence of higher molecular weight PEG chains at the membrane surface. It was also observed from AFM images that the surface nodules were larger and aligned along the spinning direction for PG-15 and PG-20 compared to P-0A.

Table 5.3 Experimental results of the surface morphology and contact angle measurement for the internal surfaces of P-0A, PG-15, and PG-20 polysulfone hollow fibers.

Hollow fiber name	PEG in the polymer solution	R_a (nm)	μ_n (nm)	μ_p (nm)	θ_a (degree)
P-0A	PEG-1000	3.8±0.1	48.1±1.36	9.2±1.35	81.3±0.7
PG-15	PEG-1500	5.8±0.3	61.4±1.33	15.4±1.24	76.3±0.4
PG-20	PEG-2000	5.5±0.3	78±1.37	17.9±1.28	77.7±0.57

*PEG-1000: Polyethylene glycol with a molecular weight of 1000 Dalton.
*PEG-1500: Polyethylene glycol with a molecular weight of 1500 Dalton.
*PEG-2000: Polyethylene glycol with a molecular weight of 2000 Dalton.
*θ_a values are advancing contact angles obtained from meniscus technique.

Figure 5.6 shows the AFM images obtained from the internal surfaces of these PS dialysis hollow fibers.

(a)

(b)

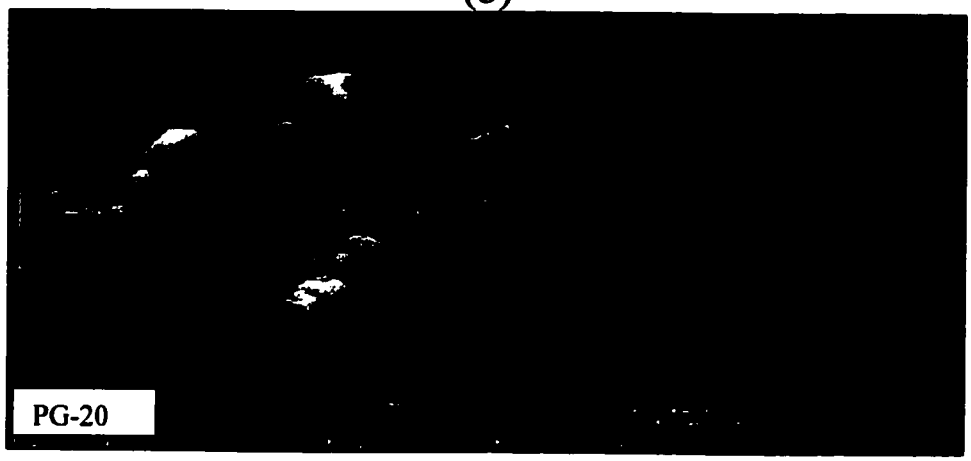

(c)

Figure 5.6 AFM images obtained from the internal surfaces of PS dialysis hollow fibers (a) P-0A, polymer solution blended with PEG-1000, (b) PG-15, polymer solution blended with PEG-1500 (c) PG-20, polymer solution blended with PEG-2000.

*P-0A is similar to P-0 hollow fiber but with a higher polymer concentration of 4 %.

5.3 Effect of various parameters on surface energetics of dialysis hollow fiber membranes.

5.3.1 Effect of Membrane Material on Contact Angle.

Figure 5.7 shows the advancing and receding contact angles as well as contact angle hysteresis of the internal surfaces of MCA, PG-20, and P-0A hollow fibers where MCA is modified cellulose acetate, PG-20 and P-0A are PS hollow fibers manufactured from the polymer solutions blended with PEG-2000 and PEG-1000, respectively. Figure 5.7 reveals that membrane surface hydrophilicity is affected by the membrane material and by the additives.

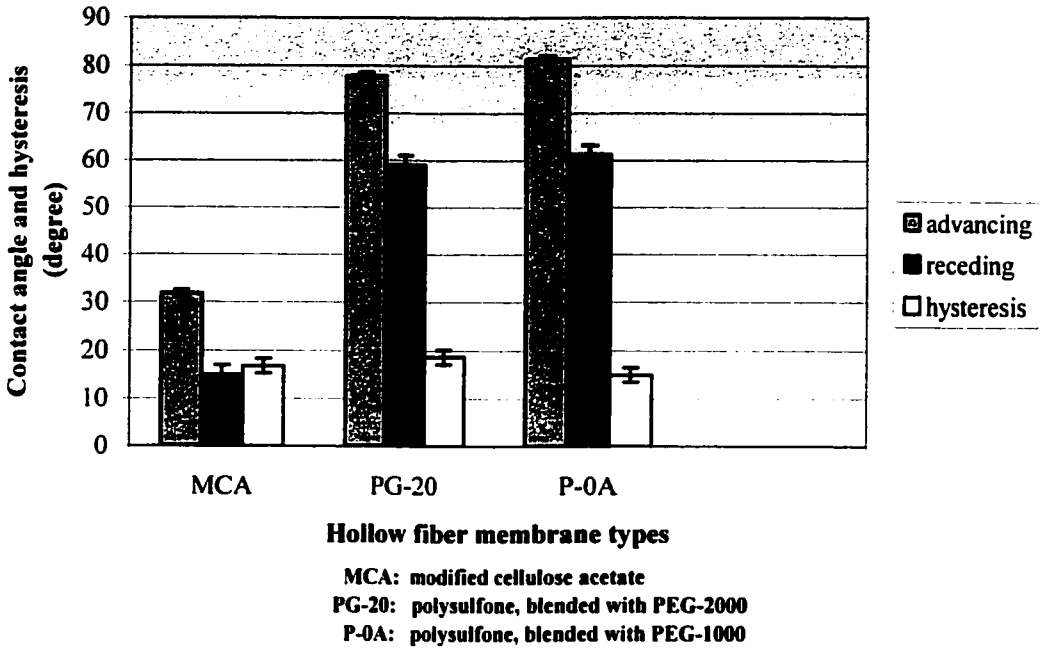

Figure.5.7 Effect of membrane material on advancing and receding contact angles and contact angle hysteresis of the internal surfaces of different dialysis hollow fiber membranes.

*contact angle data is obtained from meniscus technique.

5.3.2 Effect of Membrane Surface Morphology on Contact Angle

5.3.2.1 Direct Approach Based on Meniscus Technique.

Figure 5.8 shows the variation of advancing contact angle at the internal surface of five PS hollow fibers as a function of roughness and nodule size. Both roughness and nodule size have been shown in the form of a single value "k" that is the ratio of mean roughness to mean surface nodule size of the membranes.

According to the data in Tables 5.1 and 5.2, and the graph shown in Fig. 5.8, it was found that membranes with rougher surface and smaller nodules had a higher advancing contact angle compared to those with smoother surface and larger nodules.

This behavior was also observed for equilibrium contact angles as predicted in the theoretical section. Figure 5.9 presents the variation in equilibrium contact angle obtained from meniscus technique as well as those obtained from Eq. 3.12. To obtain the values of apparent contact angle from Eq. 3.12, parameters f_{SL} and f_{LV} were assumed to be equivalent to the numerical values of $\mu_n/(\mu_n+\mu_p)$ and $\mu_p/(\mu_n+\mu_p)$, respectively. The value of Υ_{SL} was also determined from Eq. 3.2 when $\theta_i = 68°$. This value of θ_i was obtained from capillary rise experiment.

As shown in Fig. 5.9, both sets of data obtained from experiments and those from Eq. 3.12 have the same trend when they are plotted against "k" values.

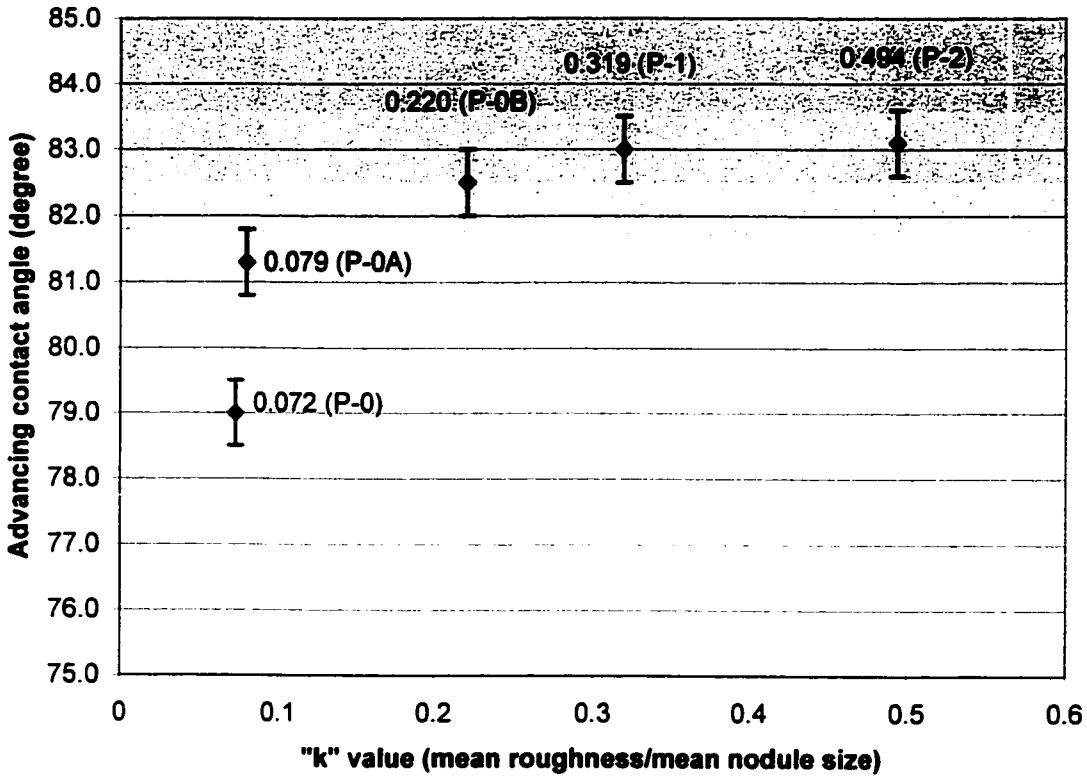

Figure 5.8 Advancing contact angle at the internal surface of P-0, P-0A, P-0B, P-1 , and P-2 hollow fibers vs. "k" value that is the ratio of mean roughness to mean surface nodule size.

*All of the hollow fibers in the above figure are polysulfone blended with PEG-1000.
*P-0, P-0A, and P-0B are PS hollow fibers dried for 5 min but manufactured under different spinning conditions, while P-1, and P-2 are the PS hollow fibers dried for one and two hrs, respectively.

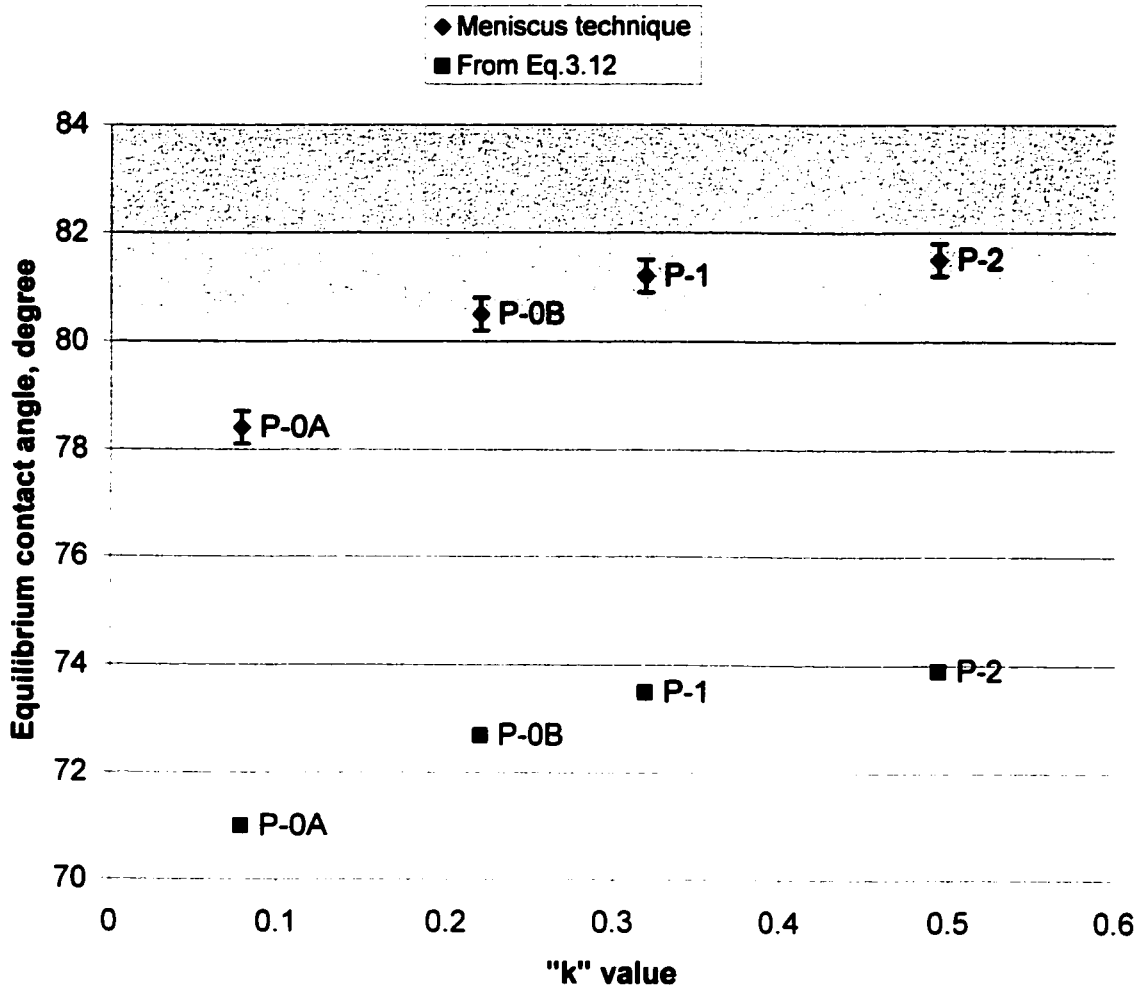

Figure 5.9 Experimental and theoretical equilibrium contact angles at the internal surfaces of P-0A, P-0B, P-1, and P-2 hollow fibers vs. "k" value.

5.3.2.2 Indirect Approach Based on Capillary Rise Technique.

Figure 5.10 shows the variation of contact angle at the internal surface of PS hollow fibers as a function of k values. Contact angles were obtained from meniscus technique, capillary rise experiment (Eq. 3.14) and the empirical Eq. 3.15. As shown in Fig. 5.10, the values obtained for θ_e from capillary rise experiments using Eq. 3.14 were in a narrow range of 67.5 to 68°, while the equilibrium values for contact angle (θ_{ap}) obtained from meniscus technique were in the range of 77 to 81°. It was also shown that θ_e values, obtained from Eq. 3.14, were independent from surface morphology (i.e. roughness and nodule size), while θ_{ap} values were affected by surface morphology. From these observations, it was hypothesized in theoretical section that θ_e values obtained from Eq. 3.14 were most likely intrinsic to the membrane surface material, while those obtained from meniscus technique were apparent contact angles.

The θ_e values obtained from Eq. 3.14 in conjunction with the membrane morphology data were used in Eq.3.15 to determine θ_{ap}. As shown in Fig.5.10, the θ_{ap} values initially obtained from Eq. 3.15 were not in good agreement with the experimental θ_{ap} values although they have shown an increasing trend when plotted against k values.

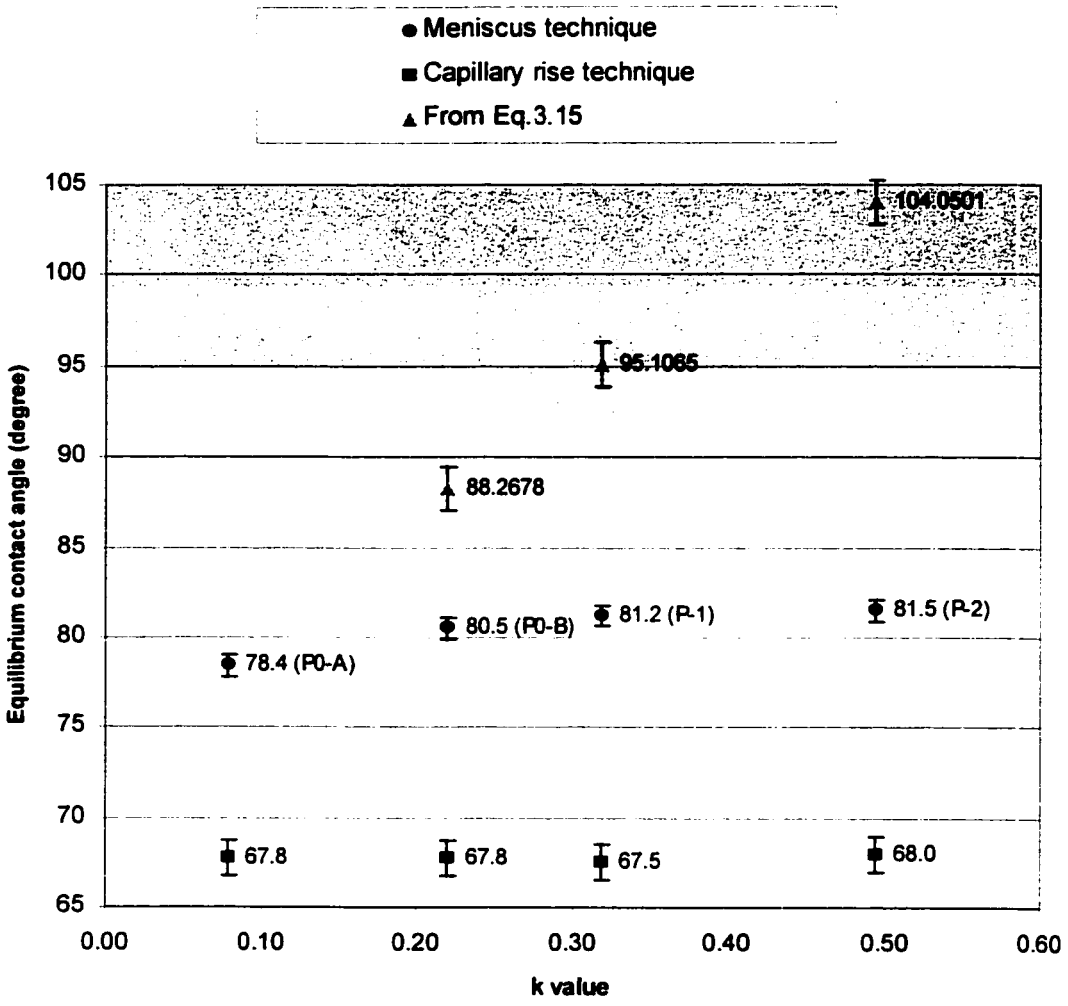

Figure 5.10 Contact angle data obtained from different techniques at the internal surfaces of P-0A, P-0B, P-1, and P-2 hollow fibers vs. "k" value.

It was known that the pores observed by AFM, which, most likely, correspond to the interstitial region surrounded by the nodules, were larger than the real pore sizes at the membrane surface. Therefore, an attempt was made to recalculate θ_{ap} from Eq. 3.15 when the pore sizes were reduced by almost 25 % of their observed values from AFM.

As shown in Fig. 5.11, the modified θ_{ap} values obtained from Eq.3.15 were almost in agreement with the experimental θ_{ap} values when the surface was microscopically rough (Ra>7 nm or k>0.2) and the contact angle was large (but less than 90°).

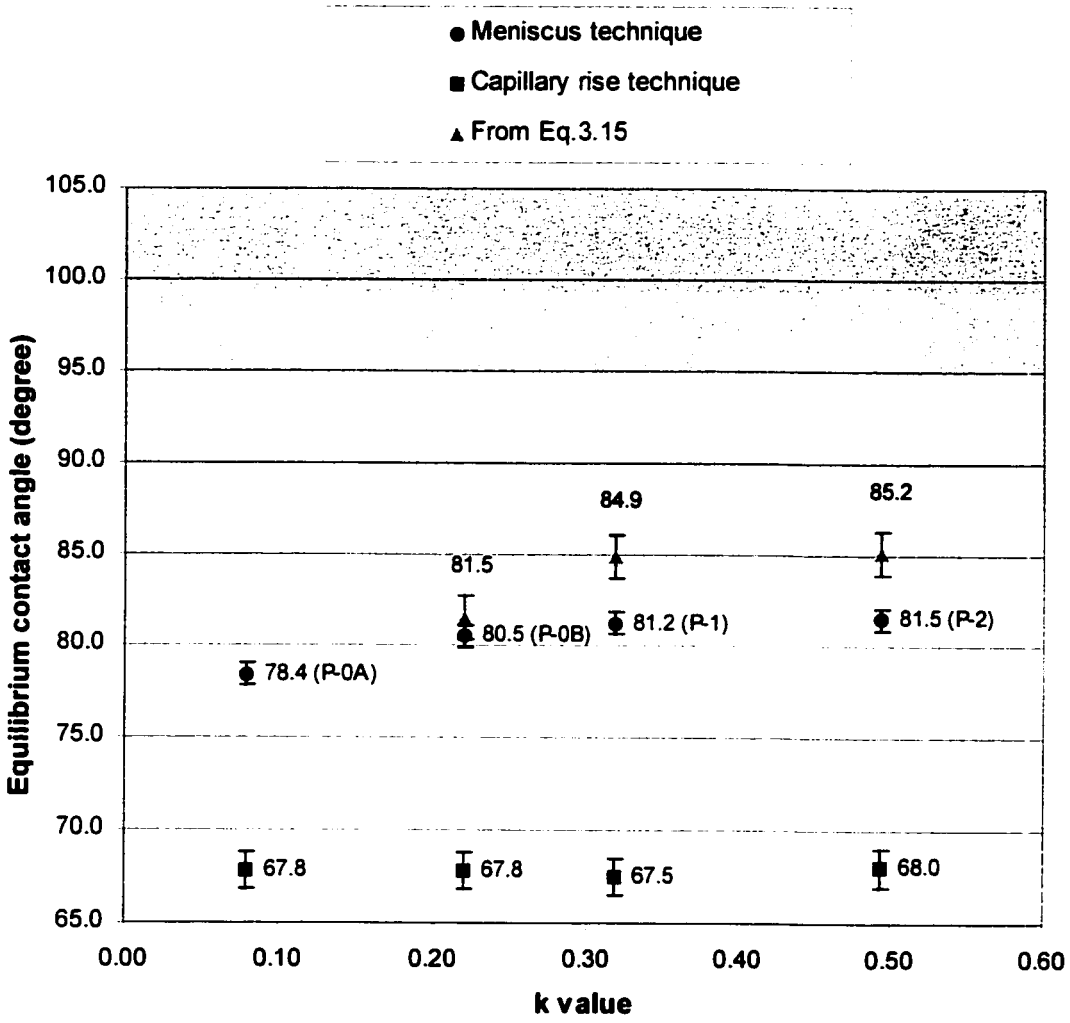

Figure 5.11 Contact angle obtained from different techniques at the internal surface of P-0A, P-0B, P-1, and P-2 hollow fibers vs. "k" value.

*Contact angle values obtained from Eq.3.15 are based on modified values for pore size (opening).

5.3.3 Effect of Surface Roughness on Contact Angle Hysteresis

Contact angle hysteresis, which is the numerical difference between advancing and receding angles, was determined for the internal surfaces of various polysulfone hollow fibers. As shown in Fig. 5.12, the rougher the surface, the higher was the contact angle hysteresis. This behavior was proposed to be the result of hindering of the test liquid front motion on the rough surfaces (Clark and Feast, 1978).

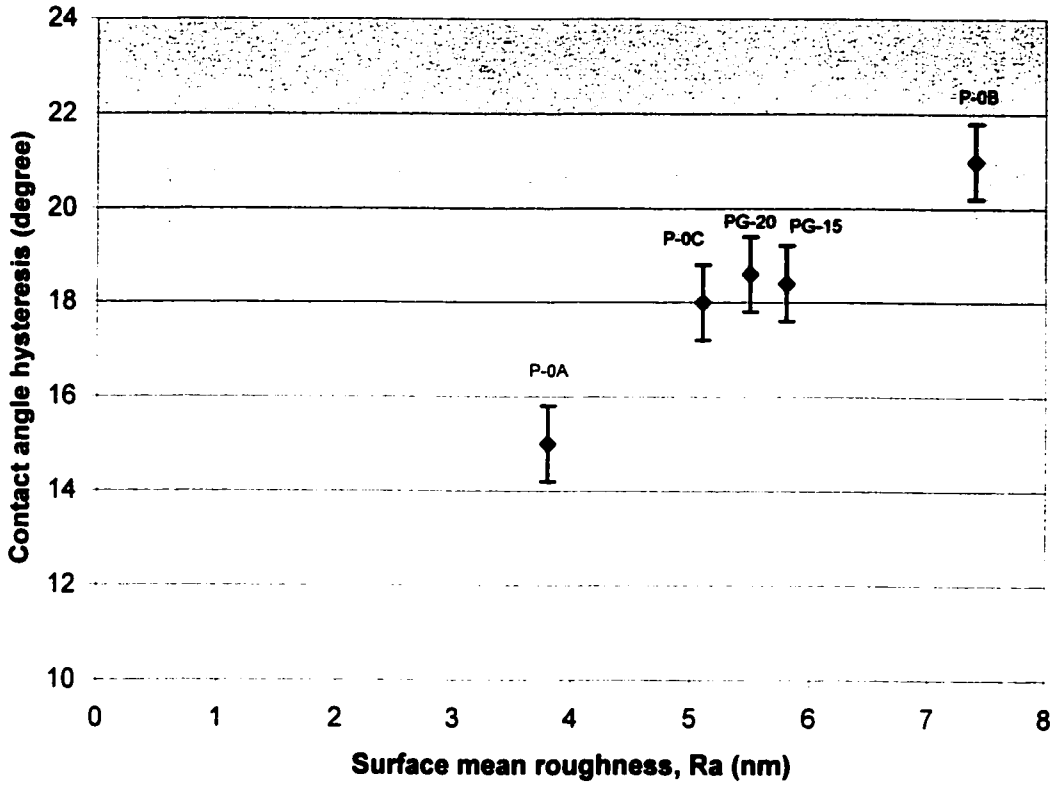

Figure 5.12 Effect of surface roughness on contact angle hysteresis at the internal surfaces of various polysulfone hollow fibers.

* P-0C is a PS hollow fiber dried for 5 min but manufactured under different spinning conditions compared to P-0A and P-0B.

5.3.4 Effect of Hollow Fibers' Dimension on Contact Angle

Figure 5.13 represents the effect of hollow fibers' outside diameter on advancing contact angle measured at the external surface of MCA and P-0A hollow fiber membranes. It was observed that contact angle at the external surface decreased when the outside diameter of hollow fibers increased. Based on the experimental results for the internal surface of hollow fibers, no correlation was observed between contact angle and inside diameter of hollow fibers.

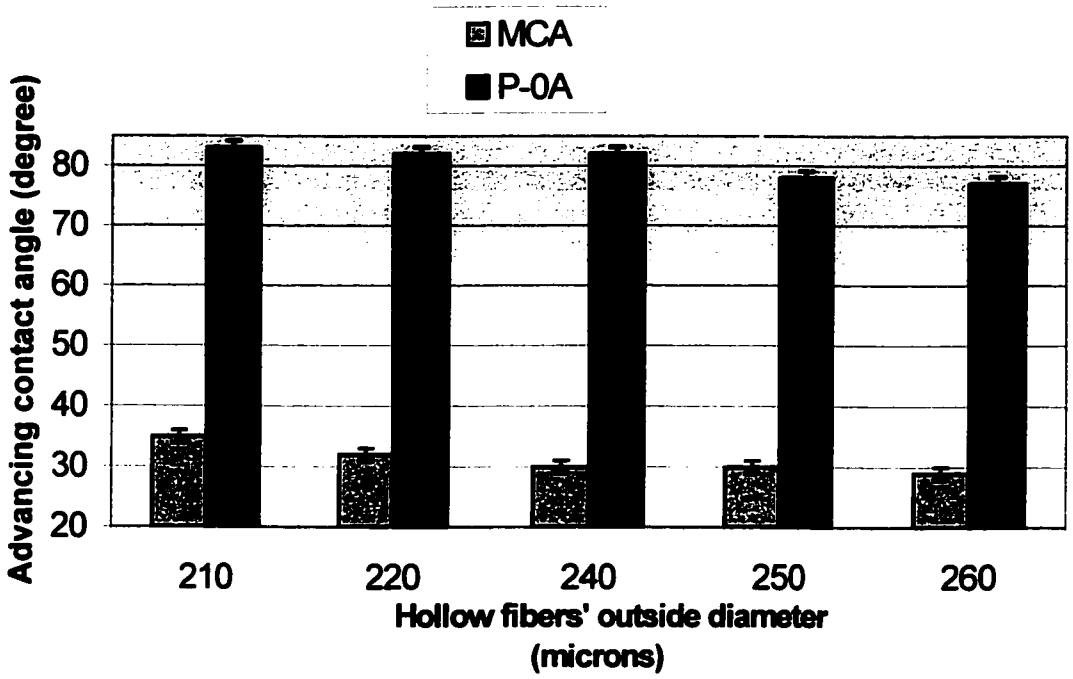

Figure 5.13 Effect of hollow fibers outside diameter on the advancing contact angle measured at the outer surface of MCA (modified cellulose acetate) and P-0A hollow fibers.

* The values for outside diameter of hollow fibers are the average of five measurements.

5.4 Surface morphology comparison between polysulfone dialysis hollow fiber membranes made by various manufacturers.

Differences in the structure of the inner and outer surfaces of hollow fibers were observed by AFM for dried samples of polysulfone membranes manufactured by three main manufacturers of dialysis hollow fiber membranes.

Surface mean roughness, and mean pore size data for the internal and external surfaces of the polysulfone hollow fibers manufactured by Baxter, Membrana, and Fresenius have been summarized in Table 5.4.

Table 5.4 Surface roughness and nodule size data for the external surfaces of three PS dialysis hollow fiber membranes manufactured by (a) Baxter, (b) Membrana, and (c) Fresenius.

Hollow fiber name	Manufacturer	Internal surface		External surface	
		R_a (nm)	μ_p (nm)	R_a (nm)	μ_p(nm)
PS-5	Baxter	2.5±0.5	7.5±1.6	10.4±2.5	8.2±1.6
DP-PS	Membrana	6.4±0.7	14±1.7	33.5±9.6	27.1±1.4
FS-PS	Fresenius	5.4±0.8	25±1.5	98.0±15.3	40.7±1.5

* R_a values for the internal surfaces are based on the scan size of 1000 nm.
* R_a values for the external surfaces are based on the scan size of 4000 nm.

It is well known that surface properties such as roughness play important roles in determining membrane biocompatibility. It is reported that smoother surfaces are more biocompatible (Tsunoda et al., 1999). Therefore, it can be expected that the PS hollow fibers manufactured by Baxter Inc. have a better biocompatibility compared to those manufactured by Fresenius, and Membrana. Figures 5.14 and 5.15 also show the AFM images of the internal and external surfaces of the above-mentioned polysulfone hollow fibers.

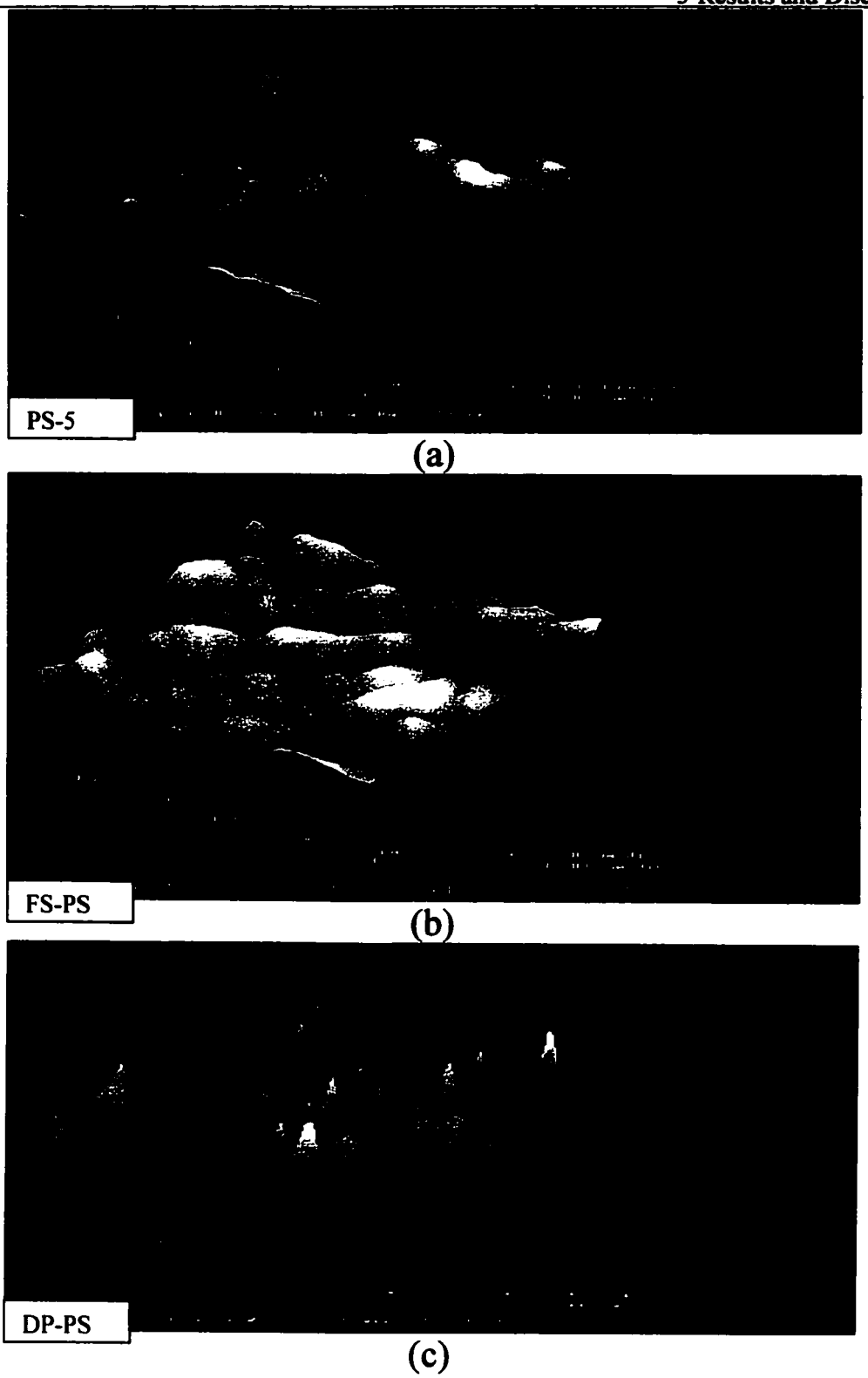

Figure 5.14 AFM images of the *internal* surfaces of typical PS hollow fibers manufactured by (a) Baxter, (b) Fresenius, and (c) Membrana.

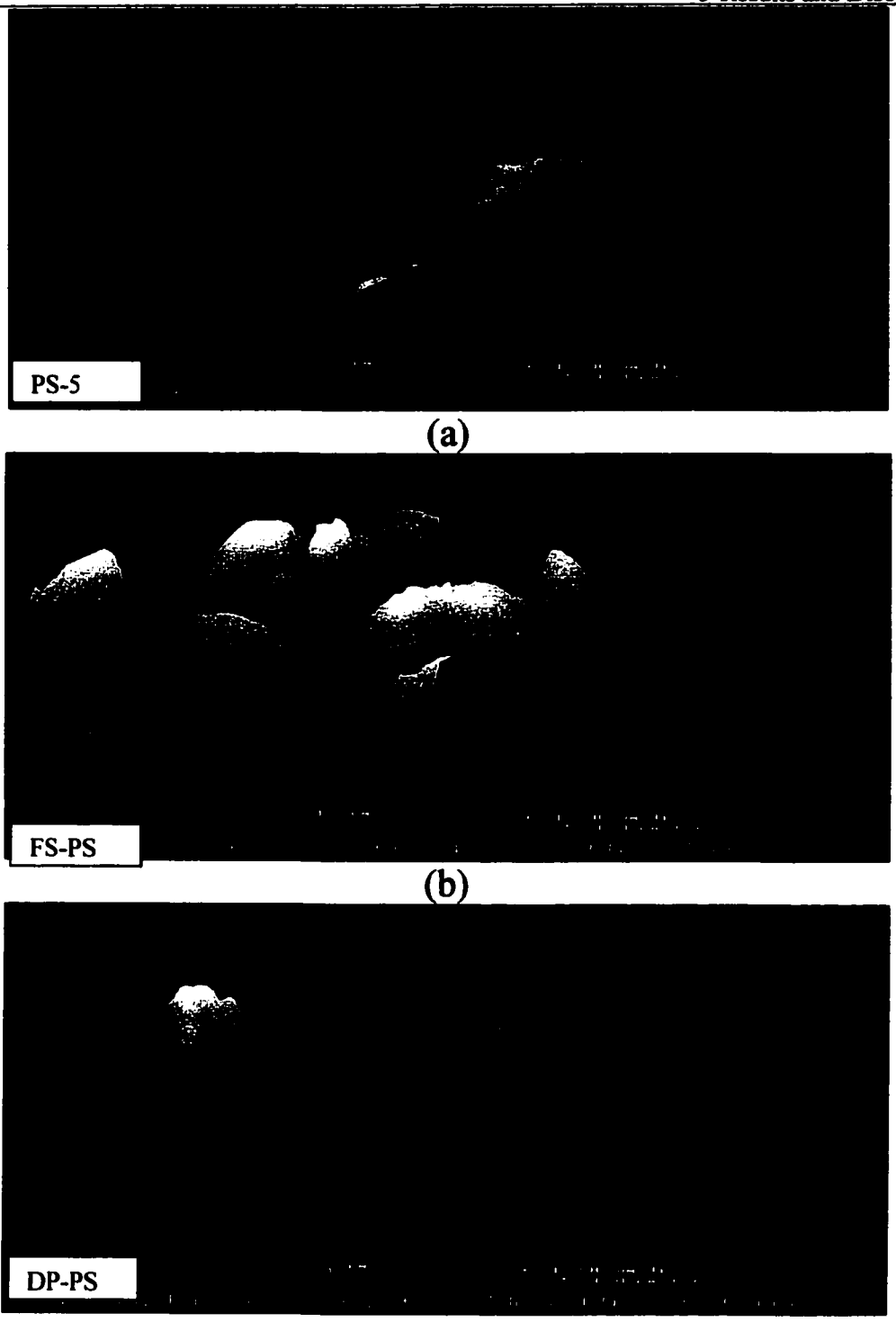

Figure 5.15 AFM images of the *external* surfaces of PS hollow fibers manufactured by (a) Baxter, (b) Fresenius, and (c) Membrana.

5.5 Contact Angle Measurement for Flat Sheet Membranes

In addition to contact angle measurement for hollow fiber membranes, contact angles of commercial flat sheet polysulfone and cellulose acetate membranes were also measured by two techniques, sessile drop and immersion techniques. Commercial membranes were obtained from OSMONICS, Inc., MN, USA.

5.5.1 Effect of the Measurement Technique on Contact Angle.

Table 5.5 summarizes contact angle results for polysulfone and cellulose acetate flat sheet membranes.

Table 5.5 Equilibrium contact angle data for PS and CA flat sheet membranes obtained from sessile drop and immersion techniques.

Membrane material	**θ_e (degree) (Sessile drop technique)**	**θ_e (degree) (Immersion technique)**
Polysulfone	**67.3±3**	**63±1.5**
Cellulose acetate	**36±3.5**	**31±2**

The data shown in Table 5.5 reveals that the contact angles measured from immersion technique are smaller and more reproducible compared to those from sessile drop technique.

5.5.2 Time dependency of the techniques used for contact angle measurement.

Effect of elapsed time after the equilibrium condition was reached was investigated for both sessile drop and immersion techniques. Figures 5.16 and 5.17 illustrate the contact angles for flat sheet polysulfone membranes obtained from sessile drop and immersion techniques, respectively.

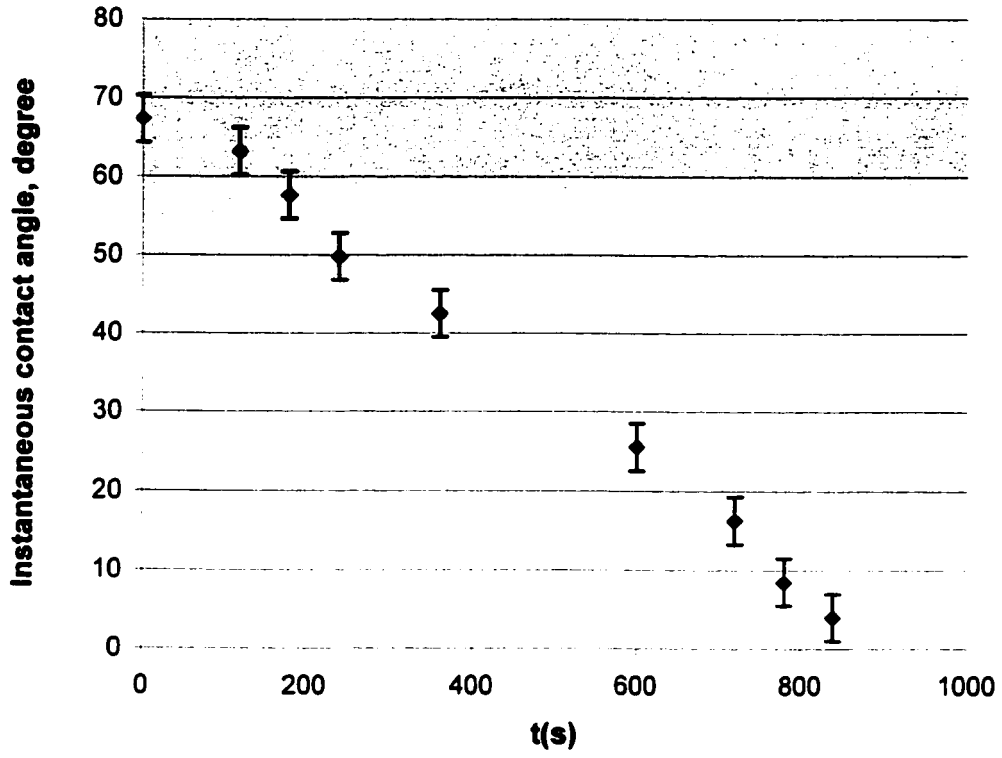

Figure 5.16 Contact angle data obtained from "sessile drop technique" vs. elapsed time for polysulfone flat sheet membrane.

* "t" is the elapsed time after the equilibrium condition was reached.
* The instantaneous contact angle at time equal to zero is equivalent to the equilibrium contact angle.
* Syringe tip was removed from the liquid drop at time zero.

Figure 5.16 shows that instantaneous contact angle decreases with elapsed time after removing the syringe tip from the test liquid drop. This was obviously due to the penetration of the test liquid into the pore structure of the membrane. Therefore, for relatively hydrophilic membranes, the measurement must be conducted as soon as the equilibrium was reached and before removing the syringe tip from the drop. Although sessile drop technique is a technique used most frequently in contact angle measurement, it is not very effective and precise as shown by Fig. 5.16. So, another alternative is necessary for contact angle measurement at the hydrophilic membrane surfaces.

Figure 5.17 shows that contact angles obtained from immersion technique for the same polysulfone membrane used in sessile drop technique. The measured values for contact angle were not changing with the elapsed time after the equilibrium condition was reached. Also, the reproducibility of this technique was found to be higher than sessile drop technique. Therefore, it seems that this technique is a more effective technique for contact angle measurement of relatively hydrophilic membranes. One of the reasons for stability of contact angle data obtained from immersion technique is that the gravity effect is minimized due to the different directions of gravity and liquid penetration through the membrane.

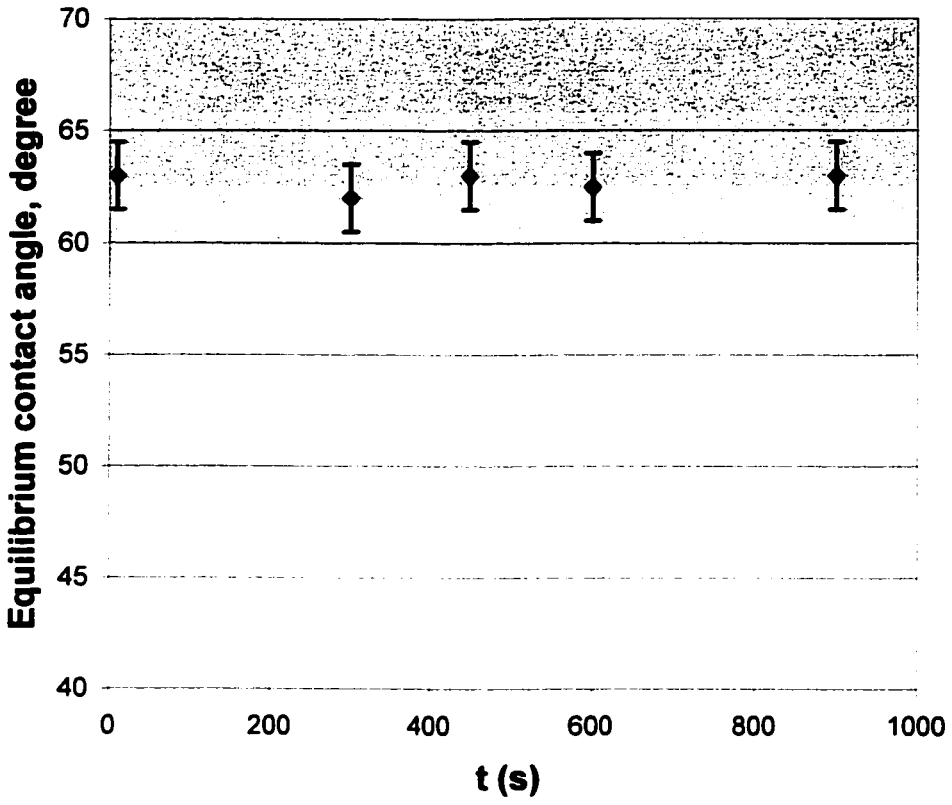

Figure 5.17 Equilibrium contact angle obtained from "immersion technique" vs. elapsed time for polysulfone flat sheet membrane.
* "t" is the elapsed time after the equilibrium condition was reached.

5.6 Microstructure study of the PS dialysis hollow fibers by scanning electron microscopy (SEM).

The microstructure of the PS hollow fibers was investigated by SEM. It was observed that there was an ultra thin skin on both inner and outer surfaces. While the ultra thin inner surface offers good possibilities for solutes to permeate through the membrane due to the low resistance the outer thin layer serves as an excellent barrier to endoxins (Nguyen and Ericsson, 1999). Figure 5.18 illustrates the skin layers both at the internal and external surfaces of a typical polysulfone hollow fiber manufactured by Baxter Healthcare Inc..

The effect of drying time on the surface of the membranes was also studied by SEM. The SEM images obtained from the external surface of the hollow fibers showed that membrane surfaces were different for various drying times. Figure 5.19 presents the external surfaces of P-0 and P-1 hollow fibers dried for 5 min and one hour, respectively. It was observed that some fissures and cleavages within the size range of 1-3 μm were produced as the effect of longer drying period.

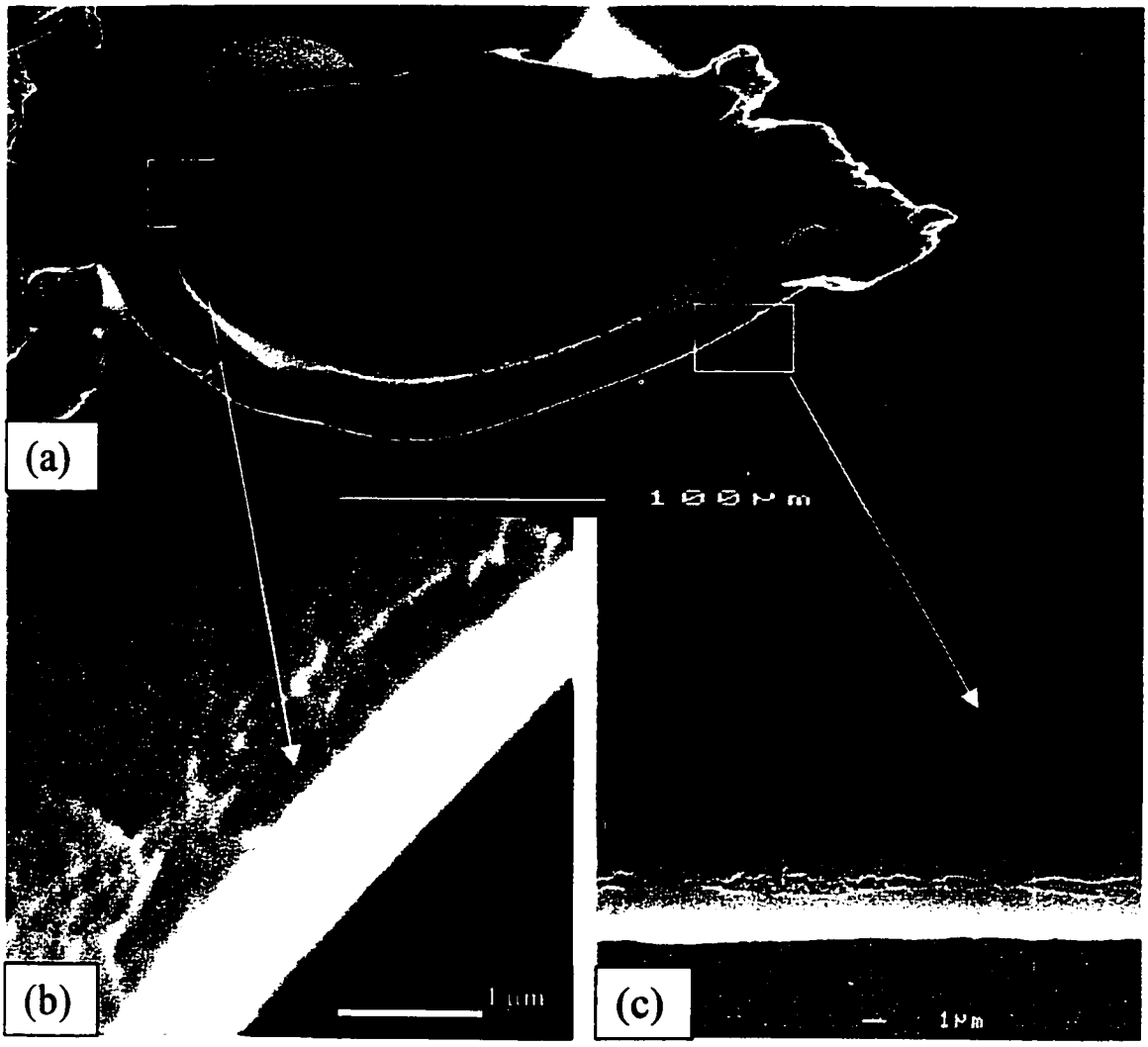

Figure 5.18 SEM images of (a) cross section (b) internal skin layer, and (c) external skin layer of a typical polysulfone dialysis hollow fiber.

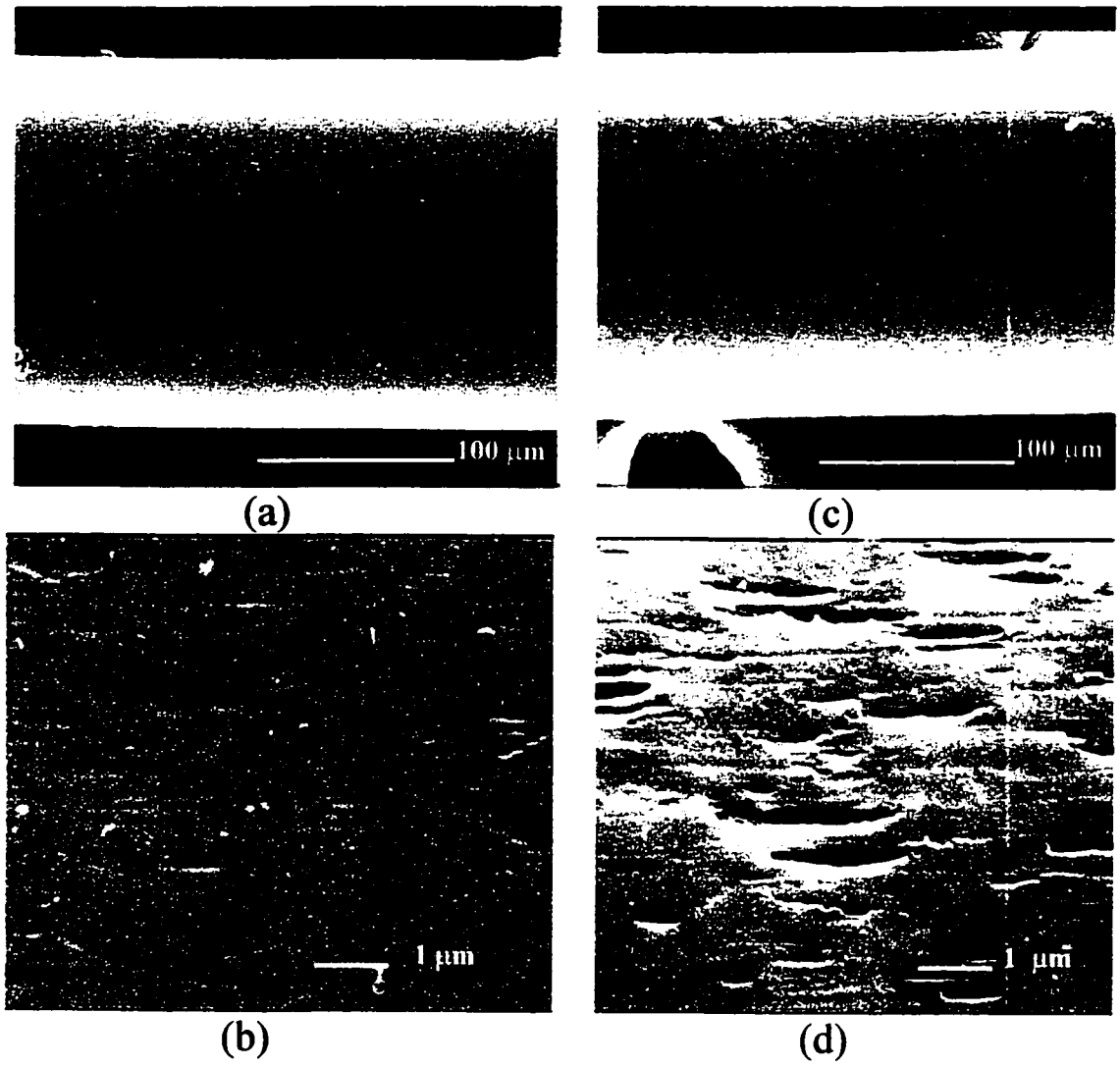

Figure 5.19 SEM images of the external surfaces of PS dialysis hollow fibers (a) and (b) dried for 5 minutes and, (c) and (d) dried for 1 hr.

Chapter 6

CONCLUSIONS

The following conclusions can be drawn from this work.

1- Contact angle measurement (CAM) is successfully applied to the internal and external surfaces of dialysis hollow fiber membranes by developing a novel technique for which a contact angle goniometer is modified.

2- Surfaces of dialysis hollow fiber membranes are characterized by atomic force microscopy (AFM) by applying a cutting technique in which fibers are cut at an inclined angle to have an access to the internal surface of them.

3- Valuable surface information is obtained by correlating the results from contact angle measurement (CAM) to those from atomic force microscopy (AFM).

4- Drying the PS hollow fibers increases roughness parameter and contact angle while decreases nodule size and pore size.

5- Mean nodule size and nodule size distribution of the hollow fiber membranes are determined from AFM studies for the first time.

6- Blending of PEG in the spinning solution increases roughness parameter and nodule size but decreases contact angle aiming at the improvement of biocompatibility.

7- Contact angle increases as the ratio of roughness parameter to nodule size increases. This is probably due to the decrease in the area of contact between liquid and polymer as air is trapped in the troughs created between the nodules.

8- Two theoretical models capable of predicting the effect of surface morphology on contact angle are developed.

9- The theoretical prediction shows that the measured contact angle would be greater than the value intrinsic to the membrane material, and the prediction is also confirmed by experimental data. This behavior is found to be the consequence of non-ideal composite surfaces.

10- It is found that the hydrophilicity of hollow fiber membranes is not only affected by the membrane material but also by the additive materials blended with the polymer solution.

11- It is observed that when the membrane surface is rougher, contact angle hysteresis, is larger.

12- It is found that contact angle at the external surface of hollow fibers decreases when the outside diameter of hollow fibers increases while for the internal surface of hollow fibers, no clear correlation is observed between contact angle and inside diameter of hollow fibers.

13- Based on the AFM studies on various PS hollow fibers manufactured by different manufacturers, it is found that those fibers which were made by Baxter Inc. have smoother inner and outer surfaces.

14- In the case of relatively hydrophilic flat sheet membranes, it is found that the immersion technique for contact angle measurement is more precise and more practical compared to the conventional sessile drop technique. Contact angles from the former technique are more stable in comparison with those from the latter one.

15- Scanning electron microscopy (SEM) is not effective for the morphology study of dialysis hollow fibers when the membrane surface is relatively smooth and pores and nodules are in the size range of nanometers.

16- According to SEM microstructure studies, polysulfone dialysis hollow fibers which were manufactured by Baxter Inc. have dense skin layers on the bore side and the shell side of the surface. Furthermore, some fissures and cleavages are generated at the hollow fiber external surfaces when they are dried for one hour and longer.

Chapter 7

RECOMMENDATIONS

In summary, Contact angle measurement (CAM) and atomic force microscopy (AFM) are developed during the course of this research to characterize surfaces of dialysis hollow fibers. Furthermore, valuable information is gathered by combining the results obtained from these two techniques. However, more effort must be made to improve other characterization techniques applicable to dialysis hollow fibers. Moreover, many areas of this research have not been pursued because of some issues and time limitations. To address these issues, the following recommendations are suggested:

1- Due to difficulties introduced by the small size and radius of curvature of these hollow fibers, it is recommended to computerize the CAM technique in order to improve the meniscus imaging as well as minimizing the equipment and human errors.

2- It is recommended to develop other characterization techniques, i.e. XPS as complementary technique, to identify the surface chemistry of the membrane and correlate them with CAM and AFM.

3- Different modification techniques, i.e. addition of chemicals or natural materials to the polymer solution to increase surface hydrophilicity, must be examined. This is to improve the membrane hemocompatibility.

4- All the surface characterization data should be combined with the membrane performance data to ensure that the applied modification techniques do not have any negative effect on the membrane performance. It will also be possible to confirm the validity of some of the surface characterization data with performance data.

5- To develop a better theoretical model capable of quantitatively predicting the effect of surface morphology on membrane hydrophilicity for the entire range of surface roughness and nodule size.

REFERENCES

Adamson, A.W., "Physical Chemistry of Surfaces", John Wiley and Sons, New york, (1982), pp.338-363.

Andrade, J.D., " Surface and Interfacial Aspects of Biomedical Polymers", Plenum Press, New York, (1985).

Andrade, J.D., "Hydrogels for Medical and Related Applications", American Chemical Soc. Symp., Ser.31, (1976).

Attard, G., C.Barnes, "Surfaces", Oxford, New York, (1998), pp. 57-61.

Boutin, B., Rame-hart contact angle goniometers, (1999), n. pag., On-line, Internet, 5 Sep. 2001, Available: www.ramehart.com/goniometers.

Chan, C.M., "Polymer Surface Modification and Characterization", Hanser, New York, (1994), pp. 1-76.

Clark, D.T, W.J. Feast, "Polymer Surfaces", Wiley, Chichester, New York, (1978), pp. 171-177.

Clark, W., D. Gao, "Research Advances in Membrane-based Artificial Kidney", in " Proc. 12th Annual Meeting of North American Membrane Soc.", D. Bhattachayya, D. A. Butterfield, L. Carlson, Eds., Lexington, Kentucky, USA, May 15-20, 2001, North American Membrane Soc., Lexington, Kentucky, (2001), pp. 137-138.

De Laplace, P.S. "Mechanique Celeste", supplement to book 10, J.B.M. Duprat, Paris, (1808).

Digital Instruments, Inc., "Nanoscope III MultiMode Scanning Probe Microscope", Instructional Manual, Santa Barbara, CA, (1993).

Elsen, R., L. K. Silva, " Advantages of Melt-spun Membrane Technology Compared to Solution Spinning", in " Evolution in Dialysis Adequacy", C. Nephrol et al., Eds., Besel, Karger, Switzerland, (1993), pp. 125-138.

Felder, R. M., R.W. Rousseau, "Elementary Principles of Chemical Processes", J. Wiley and Sons, New York, (2000).

Gibbs, W.D., " The Scientific Papers of J. Willard Gibbs", Dover, New York, (1961).

Good, R.J., "A Critical Review of Contact Angle", in "Contact Angle Wetting and Adhesion", K.L. Mittal, Ed., Utrecht, The Netherlands, (1993), pp.3-36.

Jasper, J.J., and E.V. Kring, J. Phys. Chem., Vol 59, (1955).

Kessler, S.B., E.Klein, "Dialysis process", in "Membrane Handbook", W.S. Winston and K. K. Sirkar, Eds., Van Nostrand Reinhold, New York, Ny, (1992), pp. 163-215.

Li, D., A.W. Neumann, " Thermodynamic Status of Contact Angle" in " Applied Surface Thermodynamic", A.W. Neumann and J.K. Splet, Eds., Marcel Dekker, Inc., New York, (1996), pp.109-168.

Lipps, B. J., R. D. Stewart, H.A. Perkins, G.W. Holmes, E.A. Mclain, M.R. Rolfs, and P.P. Oja., "The Hollow Fiber Artificial Kidney", Trans. Am. Soc. Artif. Intern. Organs, 13, 200-207 (1967).

Mcluch, T.B., C.Y. Chiang, H. Jaanine, T. Nguyen, J.M. Radovich, K. Ruzius, L.K. Silva, and G. Washington, "Melt-spun Polysulfone Membranes", US Patent 6,218,441, B1, (2001).

Miller, C.A., P. Neogi, "Interfacial Phenomena", M. Dekker, New York, (1985), pp. 338-437.

Miyata, T., Y. Nakanishi, T. Uragami, "Surface Modification of Poly (Dimethylsiloxane) Membranes by Polymer Additives", in "Membrane Formation and Modification", I. Pinnau and B. D. Freeman, Eds., American Chemical Society, Washington, DC, (1999), pp. 280-294.

Morra, M., E. Occhiello, F. Garbassi, Surface Interface Analysis, 16, 412 (1990).

Mulder, M., "Basic Principles of Membrane Technology", Kluwer, the Netherlands, (1995), pp. 260-267.

Neumann, A.W., D. Renzow, R. Reumuth, I.E. Richter, "Kolloide Polymers", Utrecht, the Netherlands, (1971), pp.49-55.

Nguyen, T., L. Ericsson, "Althane Polysulfone Membranes", Technical Information, Althin Medical, Miami Lakes, FL, (1999).

Odian, G., " Principle of Polymerization", John Wiley and Sons, Inc., New York, (1991), pp. 155-157.

Palacio, L., J.I. Calvo, P. Pradanos, A. Hernandez, P. Vaisanen, M. Nystrom, Contact Angles and External Protein Adsorption onto UF Membranes, J. Membrane Sci., 152, 189 (1999).

Singh, S., K.C. Khulbe, T. Matsuura, P. Ramamurthy, Membrane Characterization by Solute Transport and Atomic Force Microscopy, J. Membrane Sci., 142, 111-127 (1998).

Sourirajan, S., T. Matsuura, "Reverse Osmosis and Ultrafilteration Process Principles", National Research Council of Canada, Ottawa, (1985).

Spelt, J.K., E.I. Vargha-Butler, "Contact Angle and Liquid Surface Tension Measurements: General Procedures and Techniques", in "Applied Surface Thermodynamics", A.W Neumann and J.K. Spelt, Eds., Marcel Dekker, Inc., New York, (1996), pp.379-411.

Tan, J.M.A., "Effect of Non-solvent Additive on the Surface Morphology and the Gas Separation Performance of Poly(2,6-Dimethyl-1, 4-Phenylene) Oxide Membranes", PhD Thesis, University of Ottawa, (1999), pp. 44-45.

Tsai, M.Y., J.C. Lin, Surface Characterization and Platelet Adhesion Studies of Self-assembled Monolayer with Phosphonate Ester and Phosphonic Acid Functionalities, J. Biomed. Materials Res., 55, 554-565 (2001).

Tsunoda, N., K. Kokubo, K. Sakai, Surface Roughness of Cellulose Hollow Fiber Dialysis Membranes and Platelet Adhesion, ASAIO Journal, 418, 418-423 (1999).

Young, T., "An Essay on the Cohesion of Fluids", in "Micellaneous Works of the Late Thomas Young", J. Peacock, J. Murray, Eds., London, (1855), pp. 418-453.

APPENDICES

Appendix A

Details of the calculations of Υ_{SV} and Υ_{SL} for polysulfone in section 3.3.1

1. Calculation of Υ_{SV}

It is known that the solid-vapor surface tension can be calculated from the relationship,

$\Upsilon_{SV} \approx 75x10^{-9}\ e_{coh}^{2/3}$

in which $e_{coh} = \delta_{sp}^{2}$

and $\delta_{sp}=32.5x10^{3}\ J^{1/2}\ m^{-3/2}$ for polysulfone material.

Therefore:

$e_{coh} = \delta_{sp}^{2} = (32.5x10^{3})^{2}(J^{1/2}\ m^{-3/2})^{2} = 1055.9\ x10^{6}\ J/m^{3}$

and

$\Upsilon_{SV} \approx 75x10^{-9}\ e_{coh}^{2/3}$

where the unit of Υ_{SV} is "J/m^2" , the unit of "$75x10^{-9}$" is $J^{1/3}$ and the unit of e_{coh} is "J/m^3"

Therefore: $\Upsilon_{SV} \approx 75x10^{-9}\ (1055.9\ x10^{6})^{2/3} = 77.7x10^{-3}\ J/m^2$

2. Calculation of Υ_{SL}

γ_{SL} can be determined by substituting $\Upsilon_{SV}=77.7x10^{-3}\ J/m^2$

and the value of γ_{LV} ($72.8x10^{-3}\ J/m^2$) in equation 3.2 for different θ_i :

For $\theta_i = 60$: $\Upsilon_{SL} = \Upsilon_{SV} - \Upsilon_{LV} COS\ \theta_i = 77.7x10^{-3} - (72.8x10^{-3}\ x\ COS(60)) = 41.3x10^{-3}\ J/m^2$

For $\theta_i = 85$: $\Upsilon_{SL} = 77.7x10^{-3} - (72.8x10^{-3}\ x\ COS(85)) = 71.3\ x10^{-3}\ J/m^2$

Appendix B

Details of the parameters used in the calculation of apparent contact angle from the theoretical models proposed in section 3.3.

Table B.1 Some experimental and calculated data correspond to the graphs presented in Fig. 5.9 and Fig.5.10.

Hollow fiber	R_a	μ_n nm	μ_p nm	k	f_{sl}	f_{lv}	θ_{ap} (Meniscus.) deg.	θ_i (Capillary.) deg.	θ_{ap} (Eq.3.12.) deg.	θ_{ap} (Eq.3.15.) deg.
P-0A	3.8	48.1	9.2	0.0790	0.8394	0.1606	78.4	67.8	71.0	52.5
P-0B	7.4	33.6	11.5	0.2202	0.7450	0.2550	80.5	67.8	72.7	88.3
P-1	7.0	22.0	9.2	0.3191	0.7051	0.2949	81.2	67.5	73.5	95.1
P-2	7.9	16.0	7.3	0.4938	0.6867	0.3133	81.5	68.0	73.9	104.1

*All of the contact angle results are equilibrium contact angles.

*$\theta_{ap\ (Meniscus.)}$: apparent contact angle obtained from experimental "meniscus technique".

*$\theta_{i\ (Capillary.)}$: intrinsic contact angle obtained from Eq. 3.14.

*$\theta_{ap\ (Eq.3.12)}$: apparent contact angle obtained from Eq. 3.12.

*$\theta_{ap\ (Eq.3.15)}$: apparent contact angle obtained from empirical Eq. 3.15.

Table B.2 Some experimental and calculated data correspond to the graphs presented in Fig. 5.11

Hollow fiber	R_a	μ_n nm	$*\mu_p$ nm	k	f_{sl}	f_{lv}	θ_{ap} (Meniscus.) deg.	θ_i (Capillary.) deg.	θ_{ap} (Eq.3.12.) deg.	θ_{ap} (Eq.3.15.) deg.
P-0A	3.8	48.1	7.3	0.0790	0.8682	0.1318	78.4	67.8	70.5	47.3
P-0B	7.4	33.6	9.5	0.2202	0.7796	0.2204	80.5	67.8	72.1	81.0
P-1	7.0	22.0	7.0	0.3191	0.7586	0.2414	81.2	67.5	72.6	84.9
P-2	7.9	16.0	4.8	0.4938	0.7435	0.2565	81.5	68.0	72.8	85.2

*μ_p values in this table are modified by a decrease of almost 25 % compared to those in Table B.1.

*All of the contact angle results are equilibrium contact angles.

*$\theta_{ap\,(Meniscus.)}$: apparent contact angle obtained from experimental Meniscus technique.

*$\theta_{i\,(Capillary.)}$: intrinsic contact angle obtained from Eq. 3.14.

*$\theta_{ap\,(Eq.3.12)}$: apparent contact angle obtained from empirical Eq. 3.12.

*$\theta_{ap\,(Eq.3.15)}$: apparent contact angle obtained from empirical Eq. 3.15.

Appendix C

Time dependency of "sessile drop" and "immersion" techniques used for contact angle measurement of cellulose acetate flat sheet membrane.

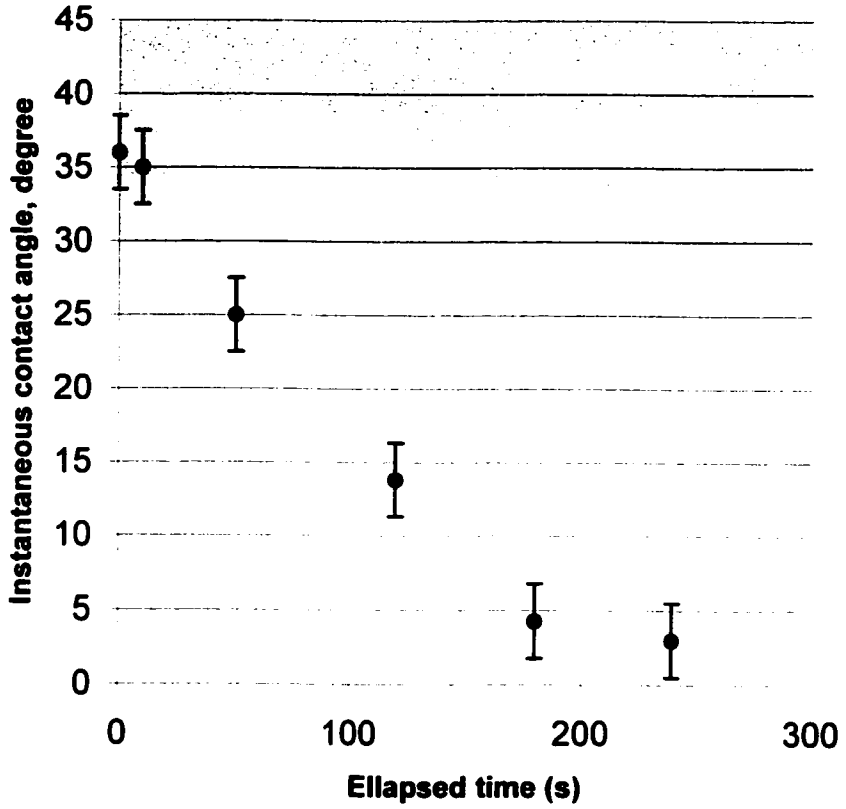

Figure C.1 Equilibrium contact angle obtained from "sessile drop technique" vs. elapsed measurement time for cellulose acetate flat sheet membrane.

* The instantaneous contact angle at time equal to zero is equivalent to the equilibrium contact angle.
* Syringe tip was removed from the liquid drop at time zero.

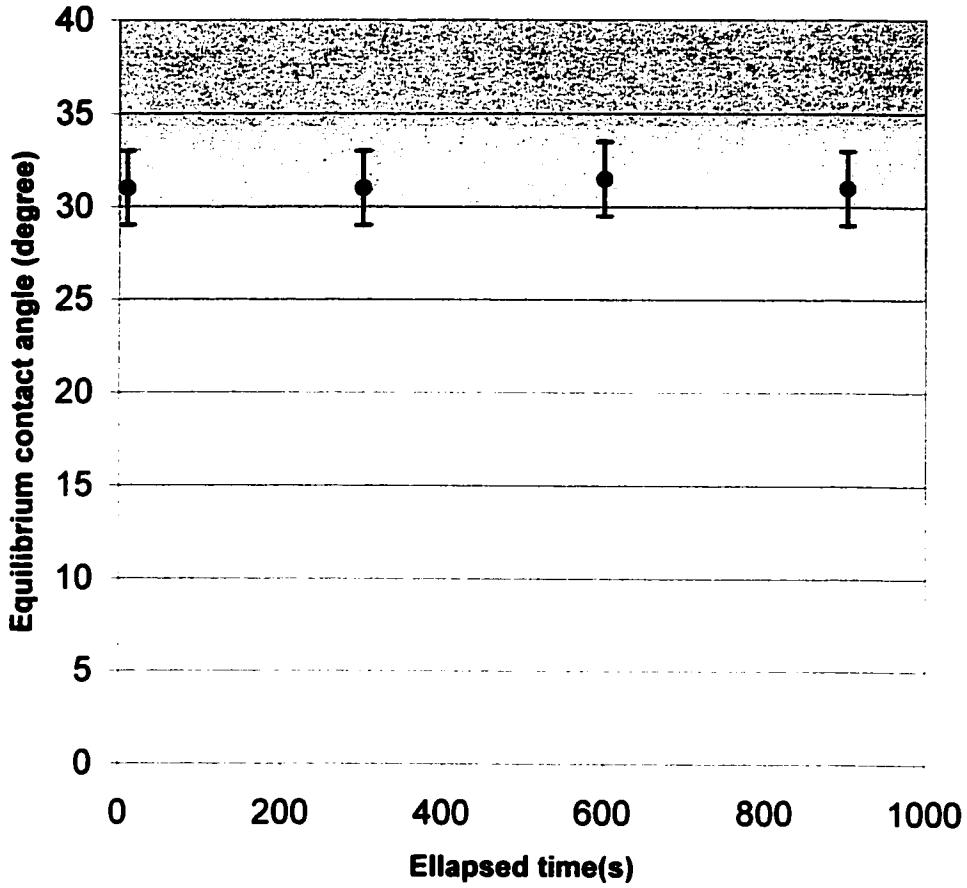

Figure C.2 Equilibrium contact angle obtained from "immersion technique"vs. elapsed time for cellulose acetate flat sheet membrane.

Appendix D

Some graphs similar to those presented in the main body of the manuscript.

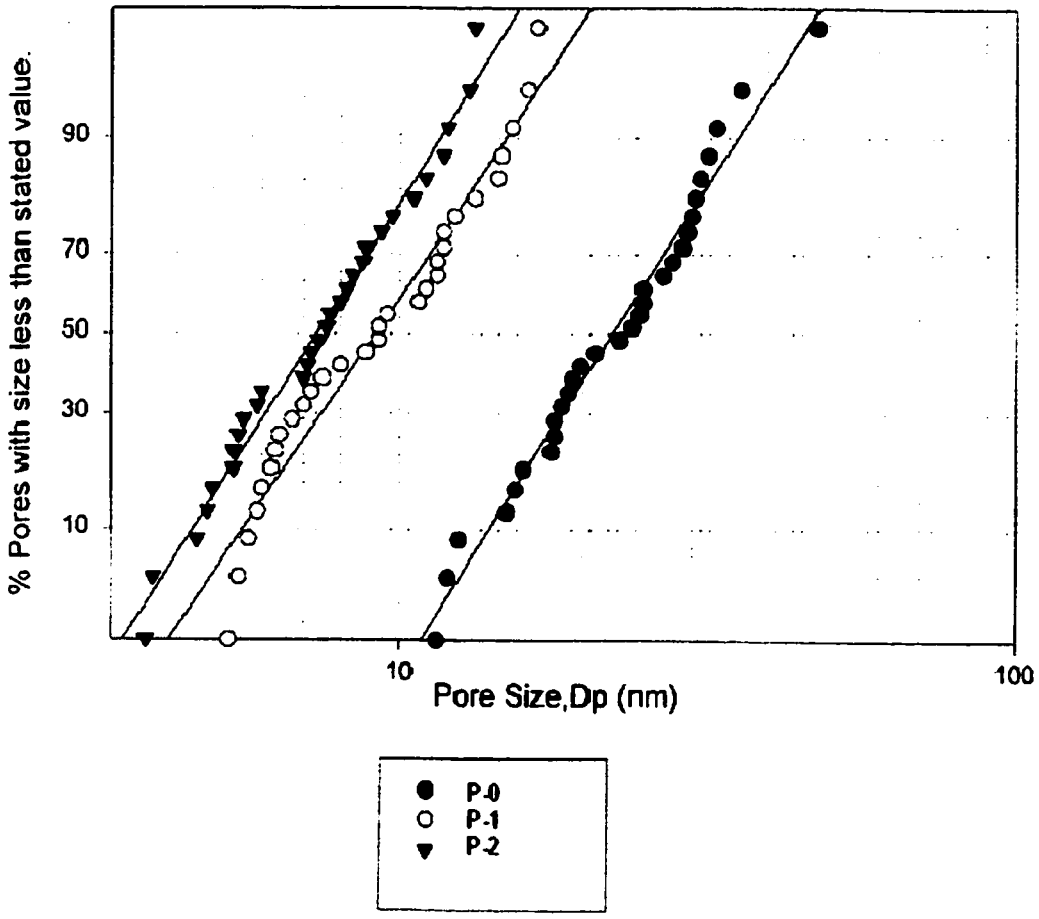

Figure D.1 Log-normal pore size distribution for the internal surfaces of P-0, P-1, and P-2 polysulfone hollow fibers subjected to drying for 5 mins, 1hr, and 2 hrs, respectively.

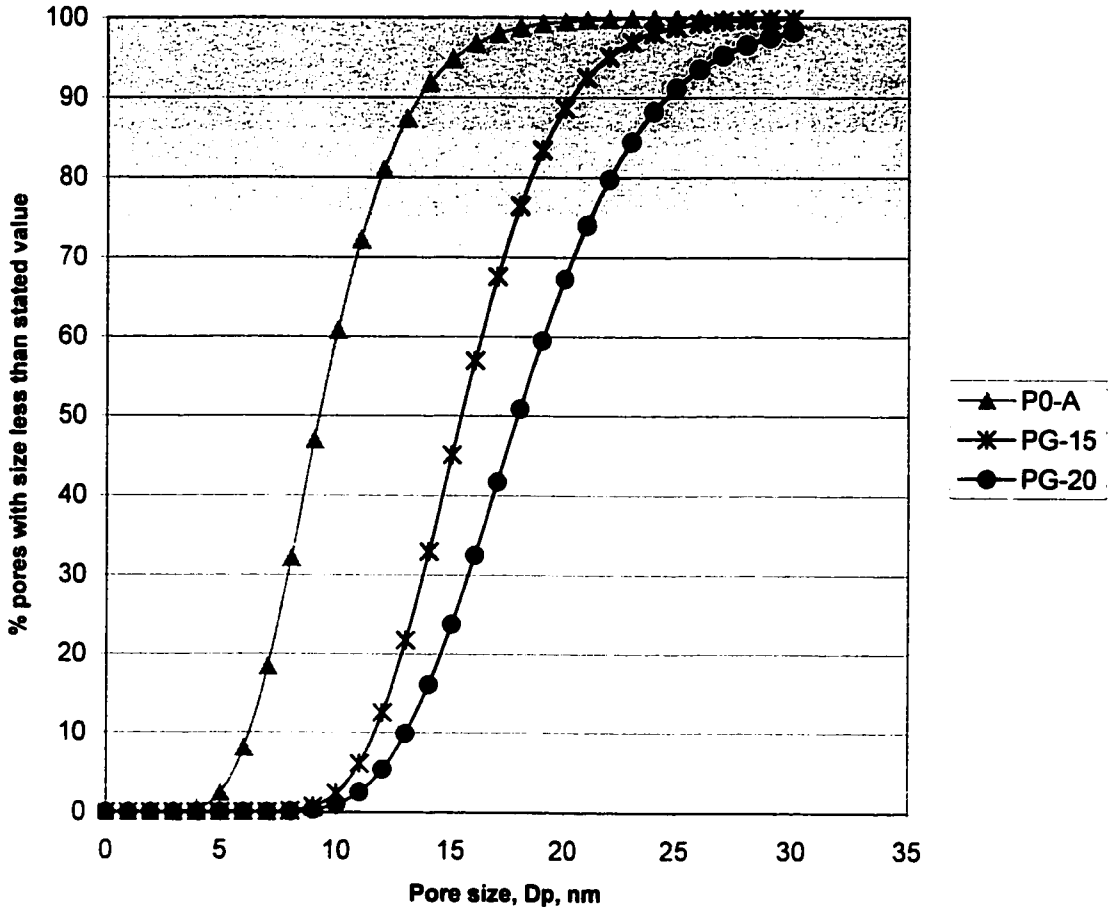

Figure D.2 Cumulative pore size distributions of the internal surfaces of P0-A, PG-15, and PG-20 polysulfone hollow fiber membranes.

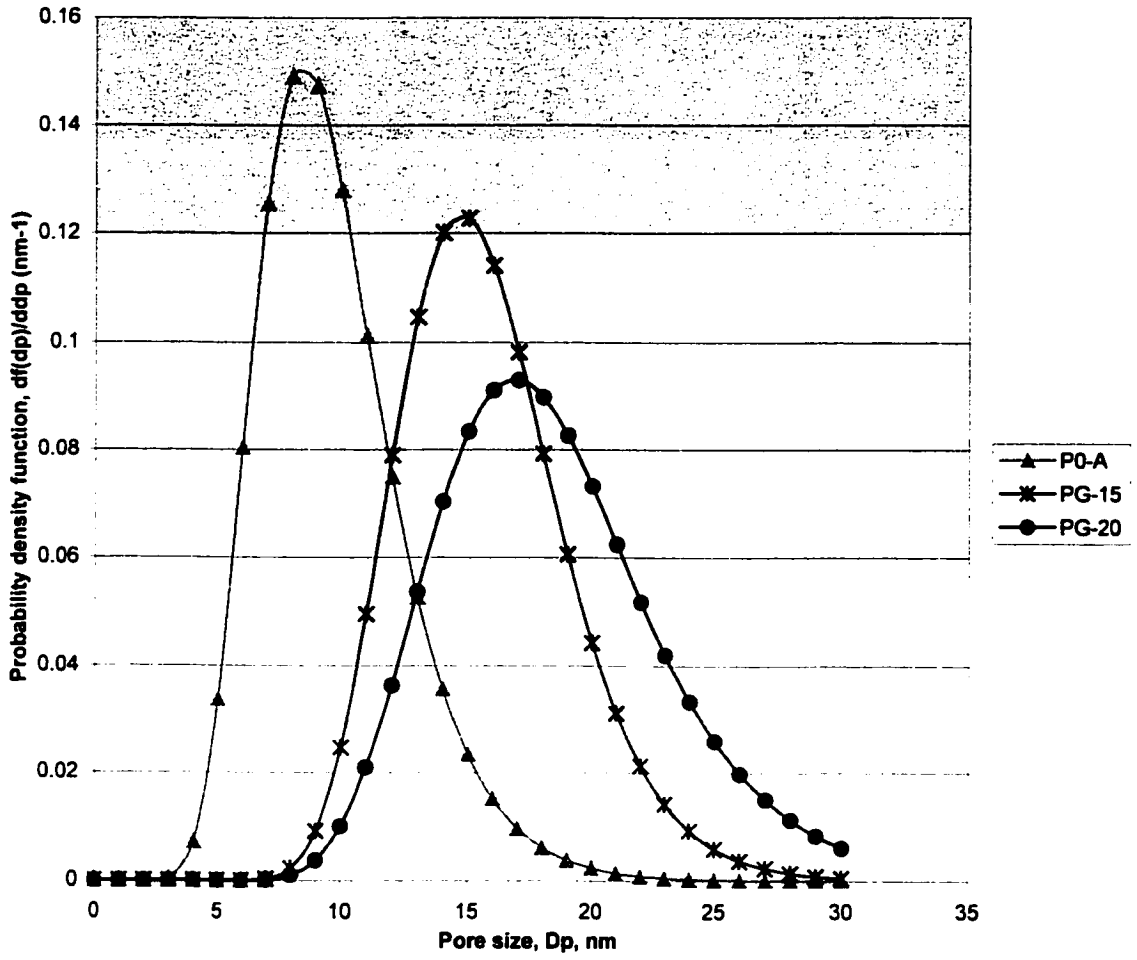

Figure D.3 Probability density function curves generated for the internal surface pores of P0A, PG-15, and PG-20 polysulfone hollow fiber membranes.